

Department of Physics  
Astronomia & Astrofisica FIS/05

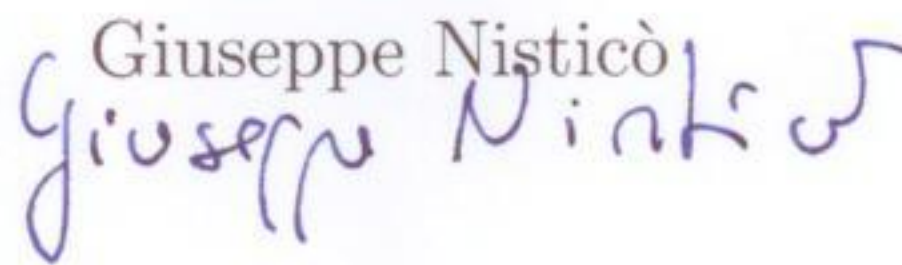
“Bernardino Telesio”  
“Doctorate School of Science and Technique”

curriculum in “*Physics of Complex Systems*”


Cycle XXIV

**Dynamics and evolution of solar corona: STEREO  
observations of jets, CMEs and numerical  
modeling**

PhD Candidate


Giuseppe Nisticò  


Supervisor  
Prof. Gaetano Zimbardo



School Director  
Prof. Roberto Bartolino

  
Curriculum Coordinator  
Prof. Vincenzo Carbone



Department of Physics  
Astronomia & Astrofisica FIS/05

“Bernardino Telesio”  
“Doctorate School of Science and Technique”

curriculum in “*Physics of Complex Systems*”

Cycle XXIV

**Dynamics and evolution of solar corona: STEREO  
observations of jets, CMEs and numerical  
modeling**

PhD Candidate  
Giuseppe Nisticò

Supervisor  
Prof. Gaetano Zimbardo

School Director  
Prof. Roberto Bartolino

Curriculum Coordinator  
Prof. Vincenzo Carbone



*“Mi piace scrivere  
e ancor più scrivere bene;  
soprattutto mi piace pensare  
e ancor più vivere quello che penso.”*

*“I like to write  
and even more write well;  
above all I like to think  
and live what I think even more.”*

Mario Borzaga OMI



# Contents

<b>1</b>	<b>The Sun: an introduction</b>	<b>1</b>
1.1	From the Sun to the boundary of the solar system . . . . .	1
1.2	The solar structure . . . . .	3
1.3	The solar corona: a deeper view . . . . .	4
1.4	The STEREO mission . . . . .	6
1.5	Aim and plan of this thesis . . . . .	8
<b>2</b>	<b>Coronal hole jets</b>	<b>13</b>
2.1	Introduction . . . . .	13
2.2	Selection criteria and statistics of the polar jet catalogue . . .	14
2.3	Typical morphology of coronal jets . . . . .	18
2.4	Coronal jet lifetimes . . . . .	24
2.5	Analysis of jet speeds . . . . .	26
2.6	3D reconstruction . . . . .	29
2.7	Summary . . . . .	31
<b>3</b>	<b>The maps of temperature of jets</b>	<b>33</b>
3.1	Temperature measurements in the solar corona . . . . .	33
3.2	Temperature from EUV filters . . . . .	34
3.2.1	Isothermal plasma approximation: filter ratio technique	35
3.2.2	Multithermal plasma approximation: DEM modeling .	38
3.3	Temperature analysis for coronal jets: motivations . . . . .	38
3.4	Temperature analysis . . . . .	39
3.4.1	Data processing . . . . .	39
3.4.2	The filter-ratio method . . . . .	39
3.4.3	The background subtraction . . . . .	41
3.5	Temperature determination results . . . . .	43
3.6	Summary . . . . .	45
<b>4</b>	<b>North-South asymmetry in the magnetic deflection of polar coronal hole jets</b>	<b>47</b>
4.1	The magnetic field structure in the solar corona . . . . .	48

4.2	Polar jet deflection measurements . . . . .	49
4.3	North-South asymmetry . . . . .	52
4.4	A model for the coronal magnetic field . . . . .	54
4.5	Calculation of the magnetic moments . . . . .	58
4.6	Comparison model vs observations: results and discussion . .	59
4.7	Summary . . . . .	62
<b>5</b>	<b>Three dimensional structure of CMEs: observations and modeling comparison</b>	<b>63</b>
5.1	Coronal Mass Ejections: a brief introduction . . . . .	63
5.2	2D or 3D shape? . . . . .	64
5.3	Forward Modeling technique of flux rope CMEs . . . . .	65
5.4	Source Region Identification . . . . .	67
5.5	Observations vs modeling: some results . . . . .	68
5.6	Summary . . . . .	73
<b>6</b>	<b>Heating heavy ions in the polar corona by collisionless shocks: a one-dimensional simulation</b>	<b>75</b>
6.1	Introduction to the coronal heating problem . . . . .	76
6.2	The numerical model . . . . .	78
6.3	The integration scheme . . . . .	82
6.4	Numerical results . . . . .	84
6.5	Summary . . . . .	89
	<b>Conclusions</b>	<b>91</b>
	<b>A Catalogue of polar coronal hole jets</b>	<b>95</b>
	<b>B Catalogue of equatorial coronal hole jets</b>	<b>101</b>
	<b>Bibliography</b>	<b>103</b>
	<b>Acknowledgements</b>	<b>113</b>

# List of Figures

1.1	Total solar eclipse . . . . .	4
1.2	Temperature and density of the corona . . . . .	5
2.1	Polar jet in the COR1 FOV . . . . .	15
2.2	Equatorial coronal hole jet . . . . .	17
2.3	Eiffel Tower Jet . . . . .	19
2.4	$\lambda$ jet . . . . .	20
2.5	$\lambda$ jet at 195 Å . . . . .	21
2.6	Helical jet . . . . .	22
2.7	Micro CME . . . . .	23
2.8	Twisted mini-prominence . . . . .	24
2.9	Lifetime distribution coronal jets . . . . .	25
2.10	Leading edge position in time for the micro-CME . . . . .	27
2.11	Leading edge position in time for the equatorial jet . . . . .	28
2.12	Speed jet profile for the jet n° 17 of <a href="#">A.1</a> . . . . .	29
2.13	Speed jet profile for the jet n° 71 of <a href="#">A.1</a> . . . . .	29
2.14	3D jet reconstruction . . . . .	30
3.1	STEREO/EUVI response functions . . . . .	35
3.2	STEREO/EUVI response functions ratio . . . . .	36
3.3	STEREO/EUVI color-color diagram . . . . .	37
3.4	Response functions STEREO A & B . . . . .	40
3.5	Background subtraction . . . . .	42
3.6	Temperature maps event n° 10 of <a href="#">A.1</a> . . . . .	43
3.7	Temperature maps event n°79 of <a href="#">A.1</a> . . . . .	44
3.8	Temperature distribution: simulation vs measurements . . . . .	46
4.1	PA measurements . . . . .	49
4.2	EUV PA vs COR1 PA . . . . .	50
4.3	N-S jet deflection asymmetry . . . . .	51
4.4	Dipole and Quadrupole field . . . . .	53
4.5	Solar magnetic structure . . . . .	57
4.6	Time evolution harmonic coefficient from WSO . . . . .	59
4.7	Classical and Radial model $\sigma$ maps . . . . .	60



4.8	Magnetic field structure . . . . .	61
5.1	CME structure . . . . .	65
5.2	CME morphologies . . . . .	66
5.3	CGS model . . . . .	67
5.4	MDI synoptic charts & Source Regions . . . . .	69
5.5	COR1, EUVI 195 and 304 CME event. . . . .	71
5.6	CME and EUV wave . . . . .	72
5.7	Carrington longitudinal and latitudinal distributions . . . . .	73
6.1	Electric and magnetic field profile . . . . .	80
6.2	O <sup>5+</sup> and H <sup>+</sup> trajectories . . . . .	85
6.3	O <sup>5+</sup> and H <sup>+</sup> velocity distributions . . . . .	87
6.4	O <sup>5+</sup> and H <sup>+</sup> energy distributions . . . . .	88

# List of Tables

1.1	Sun parameters . . . . .	3
1.2	Main characteristics of the STEREO spacecraft. . . . .	7
1.3	List of the STEREO packages . . . . .	8
2.1	Statistics of polar jet morphology . . . . .	16
3.1	EUUV wavelengths . . . . .	34
4.1	North and South fit parameters . . . . .	51
4.2	Ulysses magnetic fields. . . . .	52
6.1	H <sup>+</sup> and O <sup>5+</sup> per cent reflection rates . . . . .	86



# Chapter 1

## The Sun: an introduction

### 1.1 From the Sun to the boundary of the solar system

There are several ways for defining the Sun, some of which may be similar. We can say for example that the Sun is a giant sphere of hot gas that releases light and heat, or that it is the nearest star to us among the billions and billions of stars that populate the Universe. We can refer to its position and say that the Sun is a star located in the Orion arm of the Milky Way, and it is at the centre of the solar systems with Earth and the various planets orbiting around it. Another way, arguably more scientific, is to define the Sun as a yellow dwarf star of spectral class G2V. By this definition we are able to identify it and quantify its typical size and its mean temperature at the photosphere: indeed, “G2” means that the Sun has a typical surface temperature of about 6,000 K degrees and the suffix “V” indicates that the Sun belongs to the main sequence of the Hertzsprung-Russel diagram.

Despite these definitions, to give a complete description of the Sun in a few pages is practically impossible, considering the many phenomena and features that can be observed. The Sun shows a complex and a very dynamical structure that cannot be described with simple and few physical parameters, but we need to consider several fields of research for giving a full picture of our star. For example, nuclear physics is invoked for describing nuclear fusion reactions occurring at the centre of the Sun, which produce the energy that sustain the Sun structure; physics of matter is required for understanding how energy, under the form of radiation, propagates and interacts with matter; spectroscopy for identifying and quantifying chemical elements which compose the Sun; more in general plasma physics and magnetohydrodynamics for giving explanations of phenomena occurring in the solar atmosphere, in the solar wind and in the interplanetary medium. Then, there is also a significant contribution from optical physics, engineering and informatics for instruments and satellite design. In this sense, there is not

better way to define the Sun than to say that it represents a full laboratory of physics!

Seen by eye from the Earth, with the necessary precautions, the Sun obviously appears as a homogeneous sphere, able to light up and warm us, but, if we look more carefully and with suitable instruments, we will find a myriad of features which take place on its surface and which are also seen in the outer layers of its atmosphere. Moreover, what happens on the solar surface can have consequences on all of the solar system, and certainly an influence on the global Earth climate: it warms the Earth atmosphere, gives the necessary energy for moving the air masses and also for forming hurricanes. The signature of solar cycle is clearly found in paleontological and dendritometric studies. It is well known that the energy produced by the Sun is necessary for sustaining life on the Earth, and more in general the elements that are at the basis of the origin of life (carbon, oxygen, ...) are synthesized by nuclear reactions in the core of stars. We can say that we are made of stellar dust!

During the history of mankind, the Sun was at the centre of religious rituals, and phenomena related to it, as solar eclipses, have surprised human mind and caused fear too. It is only in the XVII century that the Italian physicist and astronomer Galileo Galilei observed for the first time the Sun by a telescope built by himself, discovering sunspots on the solar surface. Galilei was able to show that the Sun is not an immaculate body, in compliance with the Aristotelian thinking, and that it rotates by using the sunspots as tracers. After Galilei, other astronomers continued to study it with telescopes always more and more improved and powerful. The XIX century marks the main discoveries about the Sun: *e.g.*, observation of granulation on the photosphere by W. Herschel in 1801; identification of dark lines in the solar spectrum by J. Fraunhofer in 1817; determination of the cycle of the solar activity of 11 years from sunspot data by H. Schwabe in 1830; discovery of the differential rotation by R. C. Carrington in 1850; evidence of magnetic fields on the Sun by G. H. Hale in 1908.

Nowadays, we can observe in a very great detail the layers above the Sun surface and study the physical processes occurring on it thanks to modern instruments aboard spacecraft. In this context, space missions as Yohkoh, SoHO (Solar and Heliospheric Observatory), TRACE (Transition Region And Coronal Explorer), Hinode, STEREO (Solar TERrestrial RELations Observatory) and more recently SDO (Solar Dynamics Observatory) represented and represent a rich source of useful data for understanding and solving many of the open problems of Solar physics. These include, to cite just a few, the physical processes at the basis of the origin of outburst events like flares, Coronal Mass Ejections (CMEs), the acceleration mechanisms of Solar Energetic Particles (SEP events), the coupling between plasma and magnetic field in the solar corona, the paradox of the coronal heating, and the formation and propagation of the solar wind. These are only some of the

main problems inherent to the study of the Sun and that actually constitutes some of the most important field of research in solar physics.

## 1.2 The solar structure

The present knowledge of the Sun comes from the direct observations of its outer layers like the photosphere, the chromosphere and the corona, or from the measurements either in the space or at Earth of some particular physical quantities (*e.g.*, solar wind speed, density, and temperature, neutrino fluxes, geomagnetic indices, ...). Some typical parameters that describe the Sun are listed in the Table 1.1.

Parameter	Symbol	Value	Units
Age	$t_{\odot}$	$4.5 \times 10^9$	yr
Total mass	$M_{\odot}$	$1.99 \times 10^{33}$	g
Radius	$R_{\odot}$	$6.96 \times 10^8$	cm
Mean density	$\rho_{\odot}$	1.4	$\text{g}_{\odot}\text{cm}^{-3}$
Surface gravity	$g_{\odot}$	$2.74 \times 10^4$	$\text{cm s}^{-2}$
Escape Speed	$v_{\infty}$	$6.18 \times 10^7$	$\text{cm s}^{-1}$
Equatorial rotation period	$\tau_{equ\odot}$	26	days
Sunspot magnetic field strength	$B_{max}$	2500-3500	G
Photospheric temperature	$T_{phot}$	5762	K
Radiant power	$\mathcal{L}_{\odot}$	$3.90 \times 10^{33}$	$\text{erg s}^{-1}$
Radiant flux density (at 1 $R_{\odot}$ )	$\mathcal{F}$	$6.41 \times 10^{10}$	$\text{erg cm}^{-2}\text{s}^{-1}$
Astronomical unit	AU	$1.50 \times 10^{13}$	cm
Solar constant (at 1 AU)	$f$	$1.39 \times 10^6$	$\text{erg cm}^{-2}\text{s}^{-1}$

Table 1.1: Main parameters of the Sun

The interior of the Sun cannot be directly observed but its structure and physical properties are derived theoretically, based on the laws of classical physics and specific results of quantum-mechanics physics, above all atomic and nuclear physics. Informations on the internal structure are also obtained by the study of helioseismology. The Sun, and generally every star of the main sequence, is described by the equations of the ‘‘Solar Standard Model’’ (SSM), which describes it as a sphere of gas that produces a gravitational field acting on the same gas (autogravitant sphere), causing the fall down toward the center of the sphere which is in hydrostatic equilibrium by the force due to pressure. Coming from the centre, we have the core with a radius of one quarter of the solar radius, where energy is produced thank to nuclear fusion process between two hydrogen nuclei. Energy is released under the form of light and heat. The energy produced in the core, travels through out the radiative zone and then the convective zone. The photosphere is the

visible layer of the solar atmosphere. Then we have the chromosphere and the corona, visible only during the solar eclipses.

### 1.3 The solar corona: a deeper view

The outer layer of the solar atmosphere is the solar corona. It is such a tenuous layer of plasma that it is transparent to photospheric light, and becomes visible only during total solar eclipses, when the Moon obscures the solar disk. Indeed, the name “*corona*”, comes from the Latin word for crown, for indicating the halo visible during total solar eclipses (see Fig. 1.1). Since it appears only during total solar eclipses, daily observations

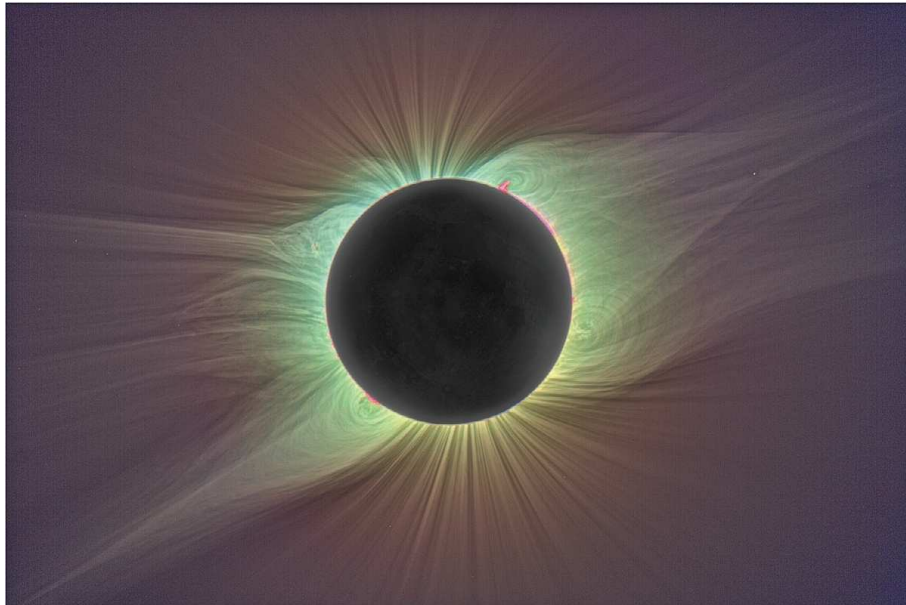


Figure 1.1: Color-enhanced image of the solar eclipse on 1st August, 2008, in Mongolia. White light coronal structure as helmet streamers at middle latitudes and ray like features at polar latitudes are well seen. Adapted from Pasachoff *et al.* (2009).

can be performed only by a special telescope, able to mask sunlight, called “*coronagraph*”. It was developed by Bernard Lyot in Paris in 1938. The corona is a very inhomogeneous medium where many spectacular as well as energetic phenomena take place. The dynamics depends on the magnetic field: a change in the magnetic field line configuration (that is the process of magnetic reconnection) determines a restructuring of the coronal structure and a releasing of energy under the form of accelerated flow, energetic particles and X-ray emission.

### 1.3 The solar corona: a deeper view

From X-ray and Extreme Ultra-Violet (EUV) images of the solar corona, we can distinguish two kinds of region, according the configuration of the magnetic field (closed or open). We have *Active Regions* (ARs) characterized by an intense X-ray or EUV emission formed by large bright loops filled with hot plasma, which trace the presence of closed magnetic field lines. They are associated in the photosphere with sunspots and represent very dynamic regions, site of very spectacular explosions. Then we have darker regions, called *Coronal Holes* (CHs) characterized by a lower emission in the X-rays or EUV. The magnetic field lines are open and the particle transport is more efficient: particles (electrons and ions) can escape in the interplanetary space, leading to the formation of the solar wind.

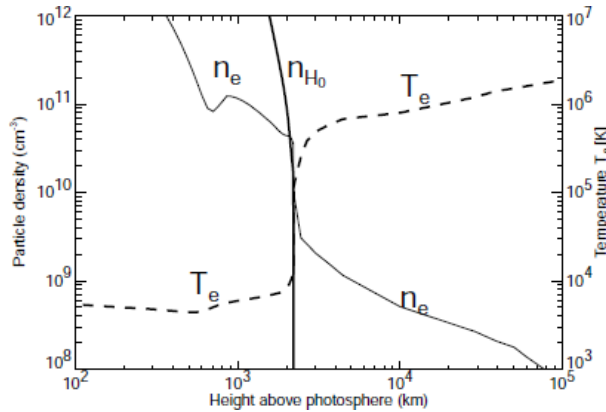


Figure 1.2: Temperature and density trend from the photosphere to the corona. Adopted from [Aschwanden \(2006\)](#).

From coronagraph or eclipse images, the corona shows the presence of helmet streamers, associated with ARs and closed magnetic field lines. Its shape varies during the solar cycle: at solar minimum it is almost symmetric, showing a reduced extension and “streamer” at low latitudes and large empty region in correspondence of poles (*polar coronal holes*) (Fig. 1.1); at solar maximum the corona is more “active” with an irregular shape, small extension of coronal holes and the presence of streamers at all latitudes. The density, that can be measured by white-light images since the emission is due to the photospheric light scattered by free electrons of coronal plasma (Thompson scattering), is typically of  $10^{15} \text{ m}^{-3}$  at  $1 R_{\odot}$ . From coronagraph observations, the coronal emission can be distinguished into three types:

- *K-corona* (*K* from German “kontinuierlich”) extending for a short distance from solar limb is due to photospheric radiation diffused for Thompson scattering by free electrons; the spectrum does not show Fraunhofer absorption lines. The intensity of the K-corona is proportional to the electron density, summed up along the line of sight;



- *F-corona* (F from Fraunhofer) extending between 2–3  $R_{\odot}$ , concentrated at the ecliptic plane characterized by a spectrum with Fraunhofer lines; this emission is due to white-light photospheric radiation scattered by dust particles (Rayleigh-scattering);
- *E-corona* (emission corona) due to a particular number of emission lines of ions.

Unexpectedly, the temperature increases from the photosphere, where  $T \sim 6,000$  K, to the corona up to the order of  $\sim 10^6$  K and coronal plasma emits very energetic radiation at X-rays (Fig. 1.2). This property was discovered in 1940s by Bengt Edlén, by spectroscopic analysis of coronal emission lines, which show a high degree of ionizations. Thereafter, Joseph L. Pawsey and David F. Martyn confirmed the high temperature of corona with measurements of intensity of radio emission. A fuller account of the story of coronal physics can be found in the books by Lang (2006); Aschwanden (2006).

## 1.4 The STEREO mission

The necessity to investigate and understand the real morphology of Coronal Mass Ejections (CMEs), and more in general, the three dimensional structure of Sun, has led to the development of the “*Solar TERrestrial RELations Observatory*” (STEREO) NASA mission. It consists of two almost identical spacecraft that have on board instruments for the remote observations and in-situ measurements. The two spacecraft are labeled respectively as STEREO-A (A from Ahead) and STEREO-B (B from Behind) since they orbit around the Sun at almost 1 AU (Astronomical Unit) respectively preceding (STEREO-A) and trailing (STEREO-B) the Earth. Their angular separation increase in time of about  $44^{\circ}$  per year. The mission started with its launch, on 26 October, 2006 from Cape Canaveral with a Delta III rocket. After the successful launch, the spacecraft were positioned in their orbit using the Moon fly-by. Only on February 2007, the first image of Sun was taken. Instruments are organized in packages and they are finalized for remote direct observations of the Sun (*e.g.*, coronal observations) or for in-situ measurements of the interplanetary conditions (*e.g.*, magnetic field, solar wind speed, particle densities). Here, we give a brief overview of the packages and their related instruments (for fuller description see Kaiser *et al.*, 2008).

- **SECCHI** (*Sun-Earth Connection Coronal and Heliospheric Investigation*) is a suite of remote sensing instruments (Howard *et al.*, 2008). It includes the Extreme Ultra-Violet Imager (EUVI) telescope, two white-light coronagraphs, named COR 1 and COR 2 which differ for the Field of View (FOV), and two white-light heliospheric imagers.

<b>STEREO Spacecraft characteristics</b>	
Mass	620 kg
Dimension	1.14 m 1.22 m wide (launch configuration) 6.47 m wide (solar arrays deployed) 2.03 m deep
Power consumption	475 watts
Data down-link	720 kbits per seconds
Memory	1 GB
Attitude	control - within 7 arcseconds (0.0019 degrees) knowledge - within 0.1 arcseconds (0.000028 degrees)

Table 1.2: Main characteristics of the STEREO spacecraft.

They are designed to study the three-dimensional evolution of CMEs from the Sun's surface through the corona and interplanetary medium to their eventual impact at Earth. The Naval Research Laboratory of Washington is the institution responsible for this package.

- **IMPACT** (*In situ Measurements of Particles and CME Transient*) was designed, build and tested by an international team of European and American research institutes. It measures the interplanetary magnetic field, thermal and suprathermal solar wind electrons and ions. It is formed by seven instruments, three of which - **SWEA** (Solar Wind Electron Analyzer), **SET** (SupraThermal Electron instrument), **MAG** (MAGnetic field experiment) - are located on a six-meter deployable boom extending antisunward. The remaining instruments - **LET** (Low-Energy Telescope), **HET** (High-Energy Telescope), **SIT** (Suprathermal Ion Telescope) and **SEPT** (Solar Electron and Proton Telescope) - are allocated on the main body of the spacecraft and are dedicated to measuring solar energetic particles (SEPs).
- **PLASTIC** (*PLAsma an Suprathermal Ion Composition*), built by an international consortium, provides in situ plasma characteristics of protons, alpha particles and heavy ions and characterizes the CME plasma from ambient coronal plasma. The institutions involved in this package are: the University of New Hampshire, the University of Bern, the Max Planck Institute for extraterrestrial Physics, the University of Kiel, and the NASA Goddard Space Flight Center.
- **S/WAVES** (*STEREO/WAVES*) was built by a team composed of the Observatoire de Paris, the University of Minnesota, and the University

of California, Berkeley. It is an interplanetary radio burst tracker that observes the generation and evolution of travelling radio disturbances from the Sun to the orbit of Earth. At its primary sensors, S/WAVES uses three mutually orthogonal monopole antenna elements, each six meters in length. The three monopoles were deployed antisunward so that they remain out of the fields of views of Sun-facing instruments.

<b>Instruments</b>	<b>Acronym</b>	<b>Purpose</b>
SECCHI	COR1	Coronagraph 1.4-4.0 solar radii
	COR2	Coronagraph 2-15 solar radii
	EUVI	Extreme ultraviolet imager
	HI	Heliospheric imager 12-215 solar radii
IMPACT	SWEA	Solar wind electrons to 3 keV
	STE	Suprathermal electron 2-100 keV
	SEPT	Electrons 20-400 keV; protons 60-7,000 keV
	SIT	Composition He-Fe 300-2,000 keV/nucleon
	LET	Protons, He, heavy ions to 40 Mev/nucleon
	HET	Protons, He, to 100 MeV; electrons to 8 Mev
	MAT	Vector magnetic field to 65,536 nT
PLASTIC	SWS	Protons, alpha dist. functions to 100 keV Heavy ions to 100 keV
	WAP	Wide angle heavy ions to 100 keV
S/WAVES	HFR	Electric field 125 kHz-16MHz
	LFR	Electric field 2.5-160 kHz
	FFR	Fixed frequency 32 or 34 MHz
	TDS	Time domain to 250 k sample/sec

Table 1.3: List of the STEREO packages and related instruments. Adapted from [Kaiser \*et al.\* \(2008\)](#).

## 1.5 Aim and plan of this thesis

The thesis aims to exploit STEREO data in order to obtain physical information on the solar corona from the instruments EUVI and COR1 of the SECCHI package, and to understand the dynamics and energetics of coronal phenomena like coronal jets, CMEs, and shock waves. All of these phenomena can be observed both in visible light and in the EUV by the instrumentation aboard STEREO. Although many other phenomena contribute to the energy balance of the corona, like flares, dissipation of waves in the chromosphere, dissipation of turbulence in coronal loops, magnetic reconnection on different sites and scales, and probably wave particle interactions (see [Aschwanden, 2006](#), for an overview), jets, CMEs and, to a lesser

extent, shock waves can be clearly identified in the STEREO data, their time evolution can be followed and their three-dimensional extent can be determined. More importantly, these phenomena share a common physics: both jets and CMEs are initiated by a magnetic reconnection between magnetic fields of opposing polarities, although on different spatial scales. The similarity between jets and CMEs arrives to the point that one of the morphologies of jets has been termed micro-CME (Bothmer *et al.*, 2010). Therefore it is important to understand the contribution of jets and CME to the coronal energy balance and to the formation of the solar wind. In addition both jets and CMEs are related to the possible formation of shock waves; for jets, the shock formation can happen in the reconnection outflow region, as envisaged in the numerical simulation of Yokoyama & Shibata (1996). For CMEs, besides the shock is associated with magnetic reconnection, a large scale shock is caused by the fast CME emergence from the low corona to the higher corona. Such shocks are frequently observed (Mancuso *et al.*, 2002; Bemporad & Mancuso, 2010), so that it is reasonable to assume that shocks can also be associated with coronal jets, although on a smaller scale. Shock waves in the corona are known to be associated with type II radio bursts, but we think that their dynamics and energetics have not received enough attention. We consider that shock waves could give a non negligible contribution to coronal heating, and in particular that they can explain the SoHO observation of preferential heating of heavy ions. In order to show this, a numerical simulation of ion dynamics at perpendicular shocks is carried out in this thesis work, too. On the other hand, the main part of the thesis work is dedicated to STEREO data analysis, due to the novel conception of this mission and to the excellent quality of the data.

More precisely, we mostly developed our research about the phenomena of “*coronal jets*” . Coronal jets appear as narrow and collimated ejections of plasma, originating in the lower layers of the corona and propagating throughout it with speeds of several hundreds of km/s. They can be observed everywhere on the Sun (active regions, quiet regions, coronal holes), but we restricted our study on jets occurring into polar coronal holes, where they appear and are identified more clearly, since their EUV emission contrasts the dark ambient of the solar limb and is not obscured by brighter coronal structures.

An interesting aspect of this work is that the study of jets, carried out in the next chapter (Chapter 2), has allowed to identify a north-south asymmetry in the magnetic deflection of jets, that possibly can give information on the north-south asymmetry of the solar magnetic field, as studied in more detail in Chapter 4. Therefore this work shows that an accurate study of the coronal features can also give information on the dynamo processes occurring in the interior of the Sun, giving a good example of cross-fertilization.

The thesis is organized in six chapters, besides the Introduction, in which we described the research work carried out during the three years of the

Ph.D. course.

The 2nd chapter is devoted to the presentation of coronal jets: we show observations of polar and equatorial coronal hole jets by EUVI-COR1/SECCHI instruments (Nisticò *et al.*, 2009, 2010). Observations of polar and equatorial jets are listed in two tables respectively in the Appendix, which report the time of observations for each instrument, the position on the solar disk and the morphology associated to the event. We discuss the possible mechanism for the origin and development of such events, in association with the morphologies that the events show. Morphologies like the Eiffel-tower jets, the  $\lambda$ -type jets, and helical structures are discussed. The statistics of the jet lifetimes in the different EUV wavelengths are obtained, and the jet velocities are discussed. We also present examples of 3D reconstruction of some jet exhibiting a helical structure.

The 3rd chapter concerns the determination of physical parameters from EUVI data; particularly, we determine the jet temperature using the filter ratio method between two filter in the EUV wavelengths (Nisticò *et al.*, 2011a). This work is motivated by the necessity to quantify some physical properties of jets, as temperature maps, in order to have a temperature estimate to make a reliable comparison with models and numerical simulations. In this chapter we explain the filter ratio technique, its advantages and limits, and give the results of temperature maps for some events, comparing then with past measurements obtained with other datasets and with numerical simulation modeling.

The 4th chapter deals with the North-South asymmetry of the solar magnetic field. Indeed, from the measurements of position angle (PA) for polar jets at 1 and 2  $R_{\odot}$ , we found a systematic asymmetry between the north and the south pole in the jet deflection, which is consistent with the asymmetry measured from other dataset (*e.g.*, magnetic field measurements from the Ulysses spacecraft, sunspot areas, Wilcox Solar Observatory (W.S.O.) multipole expansion, etc.). We made a multipole expansion of the solar magnetic field, obtaining the expression of the magnetic field as function of the dipole, quadrupole, and esapole coefficients. We integrate the magnetic field line with a Runge-Kutta scheme of the 4th order, while varying the coefficients of the multipole expansion, and compare the observed position angle of jets with that coming from the model. The comparison allows to quantify the asymmetry of the solar magnetic field.

The 5th chapter focuses on the Cylindrical Graduated Shell (CGS) model (also called “*croissant-model*”) for explaining the shape of flux-rope CMEs (Thernisien *et al.*, 2006), as observed by space coronagraphs as SoHO/LASCO or STEREO/SECCHI/COR1 and COR2. An analysis and modeling of almost one hundred CMEs, observed in COR2 data, was achieved by Eckhard Bosman, at the University of Göttingen, Germany (Bosman *et al.*, 2011). In collaboration with him, we made a comparison between modeling results and those ones coming from STEREO/SECCHI data, in order to val-

idate the goodness of the model. In more details, we compared the positions of the CME source regions obtained from the model and that one observed directly in the EUVI images. We show that a consistent number of the observed events are in good agreement with the modeling results, and that a typical latitudinal offset between the observed and modeled CME source regions is found, explained as a non radial propagation of CMEs, probably due to an influence of the global coronal magnetic field, in a similar way as discussed for jets in the 4th Chapter.

The 6th chapter is dedicated to the problem of shock wave contribution to coronal heating. Observations from the UltraViolet Coronagraph Spectrometer (UVCS) instrument aboard the SoHO spacecraft, have shown that heavy ions like  $O^{5+}$ ,  $Mg^{9+}$ , and  $Ca^{2+}$  have a strong temperature anisotropy ( $T_{\perp}/T_{\parallel} \sim 10 - 100$ ), that they are heated more than protons, and the energy is more than mass proportional (Kohl *et al.*, 1997). These results of preferential heating of heavy ions may be explained by a model (Zimbardo, 2009, 2011) in which the ion energization mechanism is the ion reflection off supercritical quasi-perpendicular collisionless shocks in the corona and the subsequent acceleration by the motional electric field  $\mathbf{E} = -\mathbf{V} \times \mathbf{B}/c$ . Such a model is supported by the observation of some small scale ejection as jets, spicules, that can create some shocks in the corona and sustain the heating, and CME driven shock waves. We performed numerical simulation by a one dimensional test particle code, studying the dynamics for protons and oxygen ions, and showing the different energization in the presence of shocks (Nisticò & Zimbardo, 2011b).

The thesis finishes giving the conclusions and the perspectives for the future, considering also the new planned space missions, like *Solar Probe* and *Solar Orbiter*, that will be launched within the end of the present decade, and that will reveal a totally new insights of solar physics.



## Chapter 2

# Coronal hole jets

In this chapter we introduce the study of coronal hole jets. They are collimated ejections of plasma that elongate from the solar surface to the outer corona. They are usually observed at Extreme Ultra-Violet (EUV) wavelengths or X-rays inside coronal hole, and in white-light by a coronagraph at height of more than  $1 R_{\odot}$ . We describe observations performed using data from STEREO spacecraft, more precisely we take advantage from image data by EUVI and COR1. Here we present the first catalogue of STEREO polar coronal jets, comprising 79 events, which were observed by both EUVI imagers in the ultraviolet, and contemporarily by the COR1 coronagraphs in white-light, during the period at solar minimum at the end of solar cycle 23 from March 2007 to April 2008. This time interval, during which the separation angle between the two spacecraft increased from 2 to 48 degrees with respect to the Sun, includes two time periods of high time cadence observations in May 2007 and January 2008. During the same period, we were able to identify a few events occurred inside coronal holes at middle latitudes, providing us another perspective on jets. Observations are organised in two catalogues listed in the Appendix, respectively for polar and equatorial jets, in which we specify time of observations at different wavelengths, duration and a basic morphology identified from EUV observations which we will discuss in a deeper view in the chapter.

### 2.1 Introduction

Among the many phenomena occurring on the Sun (*e.g.*, flares, coronal mass ejections, erupting and quiescent prominences, global waves, etc.), coronal jets are other typical outburst events, in which energy and plasma are ejected in the outer corona. They were seen everywhere, in active regions (sometimes in association with flares), in quiet and coronal hole regions. We restricted to the last type, since they are best observed inside polar coronal holes at EUV wavelengths when the plasma beams are seen in emission



against the dark background and are not obscured by bright ambient coronal structures.

First observations of coronal jets were provided by Skylab in the '70s, which was the first orbiting station around Earth and allowed to obtain first images of Sun at X-ray wavelengths. Later, more detailed observations were achieved using data from the Yohkoh satellite, which was launched on 20 August, 1991. The purpose of the mission was to study the soft and hard X-ray emission from solar flares and soft X-rays from non-flaring structures. The Soft X-ray telescope (SXT) revealed the dynamic nature of inner corona, including the appearance of collimated beams of plasma propagating from Sun to the outer corona (Shibata *et al.*, 1992; Shimojo *et al.*, 1996; Shimojo & Shibata, 2000). Polar coronal jets were studied by Wang *et al.* (1998), using images of the LASCO (Large Angle and Spectrometric COronagraph) and EIT (Extreme ultraviolet Imaging Telescope) instruments on board SoHO (Solar and Heliospheric Observatory). Further observations were reported by Alexander&Fletcher (1999) with the TRACE (Transition Region And Coronal Explorer) spacecraft. More recently, also Hinode, a Japanese mission, and STEREO have provided relevant data on polar jet parameters (Savcheva *et al.*, 2007; Kamio *et al.*, 2007; Moreno-Insertis *et al.*, 2008; Filippov *et al.*, 2009; Paraschiv *et al.*, 2010). X-ray jets have typical lengths of  $10^4$ – $4 \times 10^5$  km, widths of  $5 \times 10^3$ – $10^5$  km, and speeds ranging from 10 to 1000 km/s (Shimojo *et al.*, 1996). It is usually assumed that the jet is the result of magnetic reconnection phenomena happening in the solar corona (Shibata *et al.*, 1992; Yokoyama & Shibata, 1995, 1996; Moreno-Insertis *et al.*, 2008; Pariat *et al.*, 2009; Moore *et al.*, 2010). Coronal jets can be observed both in active regions, quiet sun and coronal holes (Shimojo *et al.*, 1996). A polar coronal jet has been studied for the first time stereoscopically with observations from the STEREO/SECCHI imagers by Patsourakos *et al.* (2008), suggesting the possible existence of helical magnetic field lines in this event.

The two points of view provided by the twin STEREO satellites are very helpful for the identification of coronal hole jets. Indeed, for the first time it is possible with STEREO/SECCHI data to assess what is the three dimensional (3D) structure of the jet, to understand what projection effects are present in single point observations, and to try to establish the true 3D velocity for the jet (Patsourakos *et al.*, 2008).

## 2.2 Selection criteria and statistics of the polar jet catalogue

SECCHI images are taken at four EUV wavelengths, precisely at 171 Å, 195 Å, 284 Å with a time cadence of 2.5, 10, 20 minutes, and at 304 Å with a time cadence of 10 minutes. During high time cadence observations on

## 2.2 Selection criteria and statistics of the polar jet catalogue

---

5th–19th May, 2007, and on 7th–20th January, 2008 the time cadences was respectively 37.5 s at 304 Å, and 75 s in the 171 channel. Because of the low time cadence of the 284 Å observations, in this jet study we concentrate on the 171, 195 and 304 Å wavelengths ranges. EUVI images were used For searching coronal jets, that are provided at the SECCHI website <http://secchi.nrl.navy.mil/>. SECCHI EUVI A and B daily movies are available at [http://cdaw.gsfc.nasa.gov/stereo/daily\\_movies/](http://cdaw.gsfc.nasa.gov/stereo/daily_movies/). The existence of subsequent jets in the COR1 A and B Field of Views (FOVs) were studied in the daily movies in intensity running difference available at <http://cor1.gsfc.nasa.gov/dailymov/MPEG/>. The running difference movies allow to identify faint transient coronal structures, *e.g.* those hidden by coronal streamers.

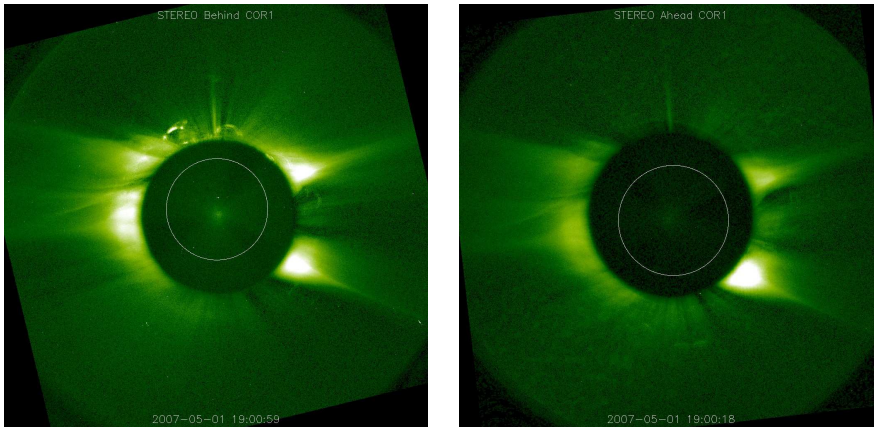


Figure 2.1: Coronal jet seen in the COR1 field of view for STEREO A and B on 1st May, 2007 near the Sun’s north pole (event n<sup>circ</sup> 10 of the catalogue in the Appendix A.1). Note the different offset of the STEREO A and B COR1 occulters with respect to the Sun’s center due to different pointing. Images courtesy SECCHI consortium.

In order to carry out a quantitative study of coronal jets, after identification of the events, SECCHI data have been analysed with the *SolarSoftWare* (SSW) package (<http://www.lmsal.com/solarsoft/>), which provides routines written in Interactive Data Language (IDL) for sophisticated SECCHI image processing. The data have been processed with the `secchi_prep` routine and specific commands such as (`plot_map`, `cursor`) have been used in order to obtain the values for the position angle of the events at the solar limb.

A selection criterion applied to the list of candidate jet events derived from the SECCHI images and COR difference movies, covering 256 events, was the unique visibility of the jets not just in the 171 Å or 195 Å observations of EUVI but also at least in either the COR1 A or COR1 B

observations. This criterion ensures that a jet is not confined to the low coronal FOV of EUVI, *i.e.*, to a height of  $1.7 R_{\odot}$ , and does not simply be a spicule or macrospicule event (Wang *et al.*, 1998; Yamauchi *et al.*, 2004). The visibility of the jet in the  $171 \text{ \AA}$  or the  $195 \text{ \AA}$  lines implies that the observed jet is comprising hot plasma at typical temperatures of  $\sim 10^6 \text{ K}$ . The condition that jets be detected by both STEREO A and STEREO B EUV imagers reduces the number of events to 79 polar jets. Fig. 2.1 shows

Classification	Number of events	Limb	Boundaries	Inside
Eiffel Tower	19/37	21	2	14
Lambda	4/12	4	5	3
Micro-CME	2/5	4	1	
Not classified	6/25	17	4	4
Helical structure	31			

Table 2.1: In the Table we supply the type-event, the number of helical events over the total number for the specific type, the locations in which polar coronal hole jets seem to occur. In the last row the total number of events that show helical feature.

an example of a typical coronal jet identified in the COR1 A and B fields of view.

In the catalogue in the Appendix A.1, we provide information on the date for all of the identified 79 polar jet events, the angular separation  $\Delta\phi_{AB}$  between STEREO A and STEREO B as seen from the Sun at the time of the events, the time of observation with EUVI at the different wavelengths and with COR1, the position angle  $\alpha$  and  $\beta$ , respectively in the EUVI and COR1 imagers at the solar limb, measured positive counter clockwise from solar North and, when possible, the result of the assessment of a jet’s morphology. The spatial distribution of jet positions corresponds to 45 events (57%) found in north polar coronal holes (NPCHs) and to 34 events (43%) in south polar coronal holes (SPCHs). The question whether the slight difference in the number of northern and southern events is related to a different areal size of the coronal holes in both solar hemispheres is beyond the scope of the present study.

A number of equatorial jets have also been found in the course of the search for coronal jet events, indicating that coronal jets are an overall coronal feature rather than limited to the polar regions, in agreement with the findings of (Moreno-Insertis *et al.*, 2008). Fig. 2.2 shows a sample event as a sequence of images from STEREO B at  $304 \text{ \AA}$ , in which the equatorial jet on 11th November, 2007, has been identified (event n<sup>o</sup> 10 of the catalogue in the Appendix B.1). The corresponding equatorial coronal hole can be seen as a darker cooler area. The jet was also visible in STEREO A, although it appeared behind the limb from this perspective (angular sep-

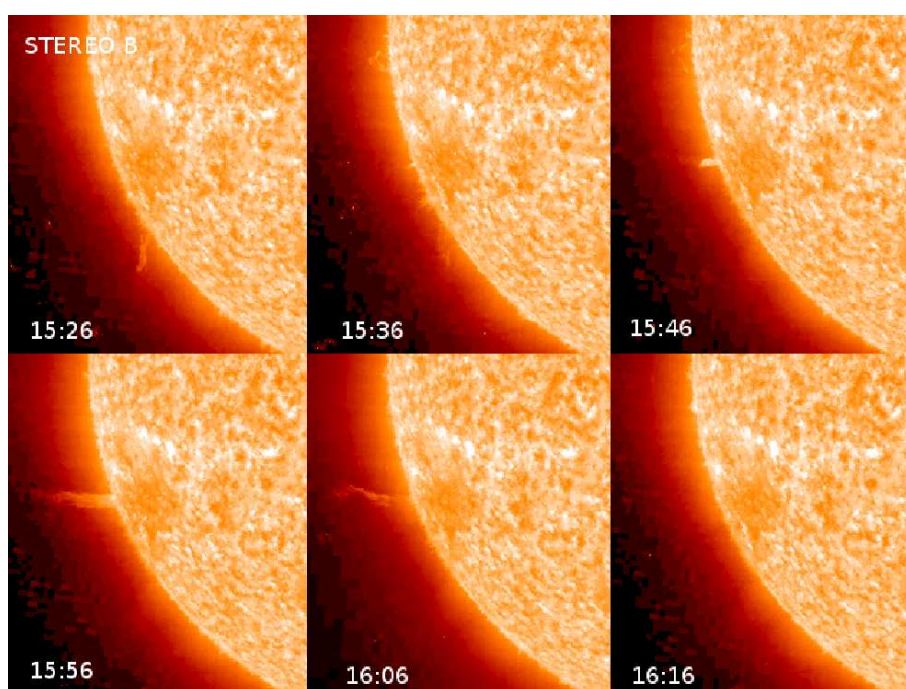


Figure 2.2: Sequence of images showing the evolution of an equatorial coronal jet on 11th November, 2007 (event n° 10 of the catalogue [B.1](#)).

aration  $\Delta\phi_{AB} \simeq 40^\circ$ ). The event was also visible in the 171 Å and 195 Å wavelengths.

However, because of the usual presence of large-scale equatorial coronal structures as is typical near solar minimum, *i.e.* in the presence of a streamer belt, only for very few equatorial jet events a clear subsequent signal could be identified in the COR1 data without improved image analysis. The equatorial jets identified so far from the SECCHI data are included in the equatorial jet catalogue presented in the Appendix B.1: we listed 15 events, specifying the date, the time of visibility for each EUVI wavelength, the time of appearance in the COR1 FOV, and the position angle in the EUVI and COR1 FOV.

### 2.3 Typical morphology of coronal jets

Based on previous results coronal jets can be basically classified into the following two categories (Table 2.1): i) *Eiffel Tower* (ET) jets which resemble a shape like small helmet streamers or an Y-inverted shape, and correspond to the magnetic topology of a small-scale photospheric bipole reconnecting with ambient open unipolar field lines of opposite polarity at its looptops (Shimojo *et al.*, 1996; Yamauchi *et al.*, 2004; Patsourakos *et al.*, 2008; Pariat *et al.*, 2009; Moore *et al.*, 2010); ii)  $\lambda$ -jets in which a small-scale photospheric magnetic bipole reconnects with ambient unipolar field lines near its footpoints (Shibata *et al.*, 1992; Yokoyama & Shibata, 1996). It should be noted that the EUVI observations only allow us to distinguish whether a jet occurred close to loop tops or the loop footpoints, *i.e.* we do not observe directly the magnetic field structure. An ideal case would thus be the phase of the STEREO mission when the viewing angle with respect to the Sun-Earth line had increased to about 90 degrees to correlate limb observations from STEREO with disk centered magnetograms from Hinode and SOHO. The morphology for each of the jet events listed in the Table of the Appendix A.1 was investigated for its morphological characteristics according to the above two categories. Fig. 2.3 and Fig. 2.4 show archetype “Eiffel tower” and “lambda” events observed by SECCHI EUVI A and B.

Fig. 2.3 shows a sequence of images of a north polar coronal jet taken at 171 Å, seen by both STEREO A and STEREO B on 1st May, 2007 (event n° 10 in the catalogue A.1). The fast ejection of hot material, as well as the bright loop at the bottom of the jet, are clearly seen by both spacecraft. The angular separation was  $\Delta\phi_{AB} \simeq 6.18^\circ$ , and the difference in the viewpoints is already becoming obvious and it is also possible to identify the helical structure of the magnetic field in the ejection.

Fig. 2.4 shows a sequence of images at 284 Å for a south polar jet taken on 17th November 2007, when both spacecraft were separated by  $\Delta\phi_{AB} \simeq 40.57^\circ$  (event n° 51). In STEREO EUVI A images, the jet is

### 2.3 Typical morphology of coronal jets

---

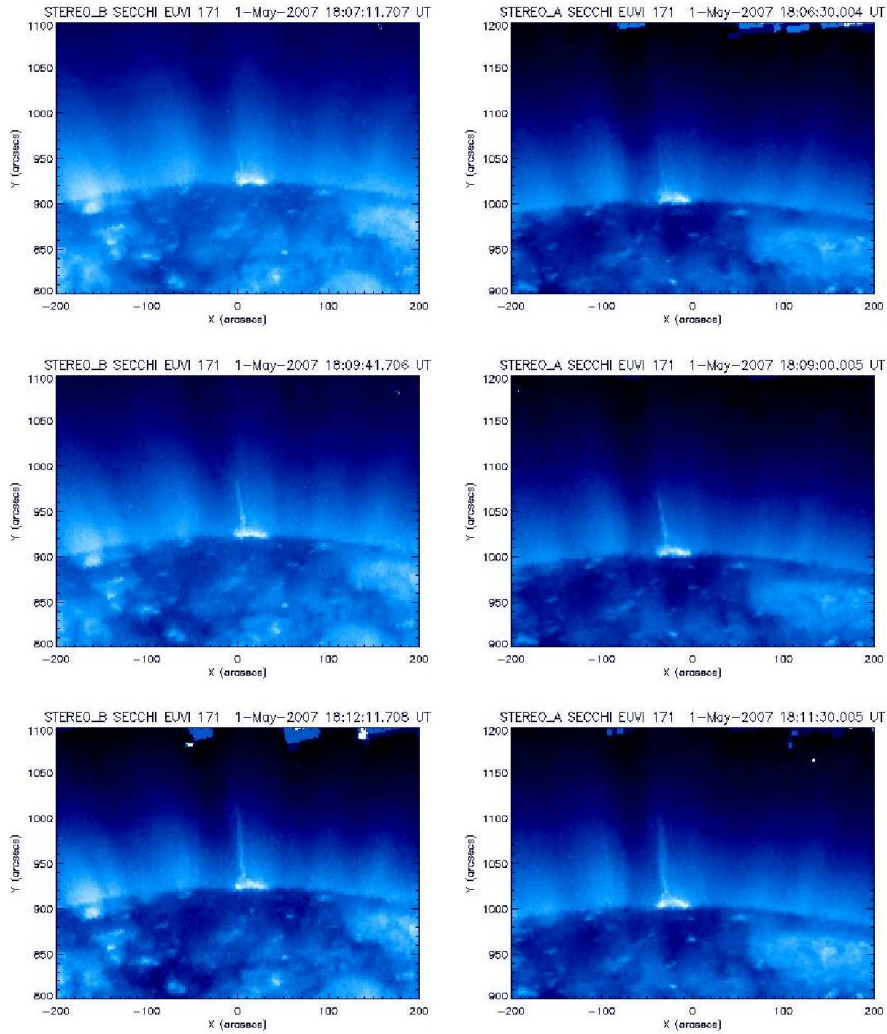


Figure 2.3: “*Eiffel Tower*” event in the north polar coronal hole on 1st May, 2007, imaged at 171 Å. Left: view from STEREO/SECCHI EUVI B. Right: view from STEREO/SECCHI EUVI A. Note that in this case the small loop below the jet is clearly resolved.

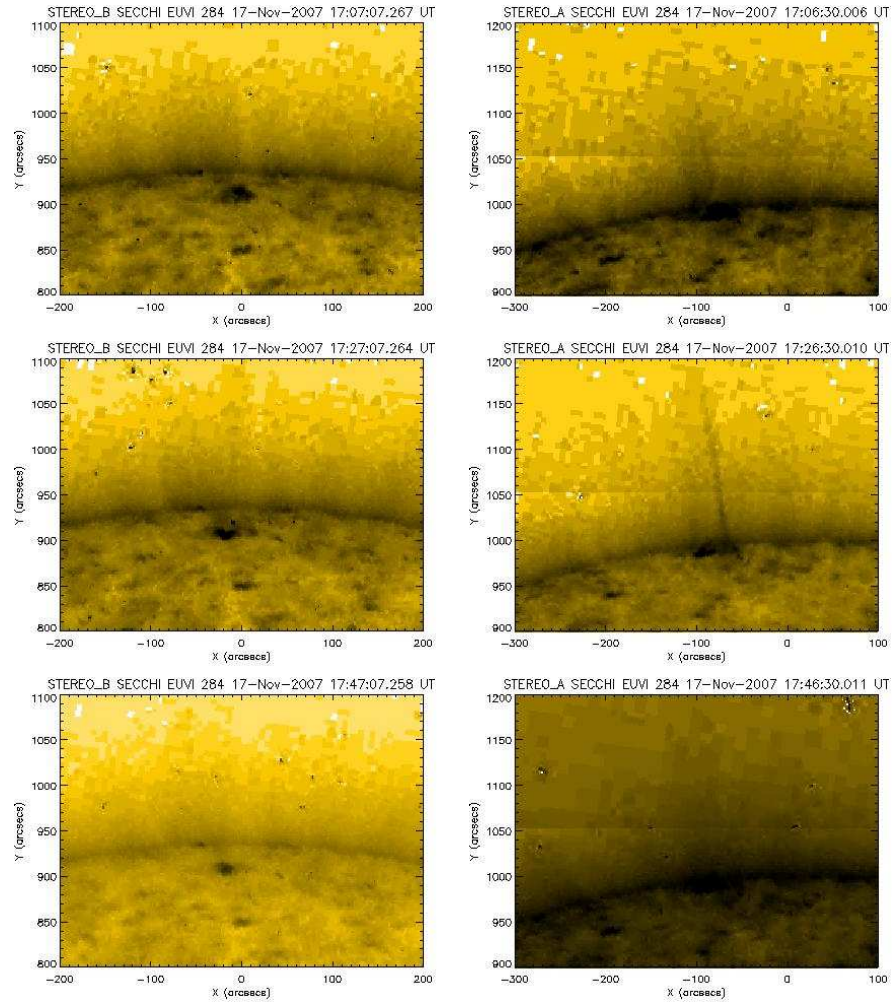


Figure 2.4: “ $\lambda$ ” event in the north polar coronal hole on 17th November, 2007, as observed by SECCHI EUVI A and B at 284 Å. Left: view from STEREO B. Right: view from STEREO A. Note that whereas in the STEREO A images the footpoint is characterized by a bright point and the ejection is shifted from it, B shows only the bright footpoint but no evidence of the ejections, maybe because it is very thin and it cannot be resolved.

## 2.3 Typical morphology of coronal jets

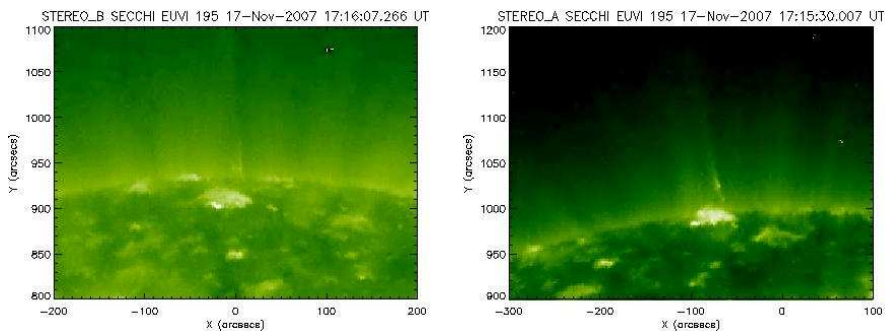


Figure 2.5: 195 Å “λ” type coronal jet seen by STEREO A and B on 17th November, 2007.

associated with the presence of a bright point at one leg of the loop and the ejection is developed at the opposite leg. In STEREO EUVI B only the presence of the bright point is visible. For this same event, images in 195 Å show ejection at the same heliographic position but the footpoint seems to be characterized by a small loop (Fig. 2.5). This event shows that the jet morphology, and even its very detection, can change with the point of view.

As can be seen from Fig. 2.3 and Fig. 2.4, the jet footpoints typically appear as chromospheric bright points or loops. These features sometimes seem to coexist whereas in other cases they appear from different perspectives as the same structure in the SECCHI A and B images. We interpret this finding as projection effects of small loops resembling coronal bright point at lower coronal altitudes viewed face on. These observations emphasize the importance of different perspectives.

Another important feature of the jet events, which we investigated, was whether a helical structure along the jet axis, as first reported by (Patsourakos *et al.*, 2008), could be identified. A sample event is presented in Fig. 2.6. This north polar jet exhibits a prominent helical structure but not seen to originate from an emerging closed loop system. It was observed at 304 Å on 2nd February, 2008 (event n° 74 of the catalogue in A.1), when the angular separation was  $\Delta\phi_{AB} = 45.45^\circ$ . It can be seen that the two helical arms appear well separated in STEREO B, while they partly overlap in STEREO A. This helical structure is also clearly seen at 171 Å and 195 Å, although the images are less bright. Out of the total number of 79 events, 31 events clearly revealed a helical structure as indicated in the Table of the jet events in the Appendix A.1. Since the presence of a helical structure is important to test the validity of different jet models (*e.g.*, Pariat *et al.*, 2009) these events are important cases for further modeling. The question why not all jets show helical structure cannot be uniquely answered. A possibility is that they were very narrow so that the twist could not be re-



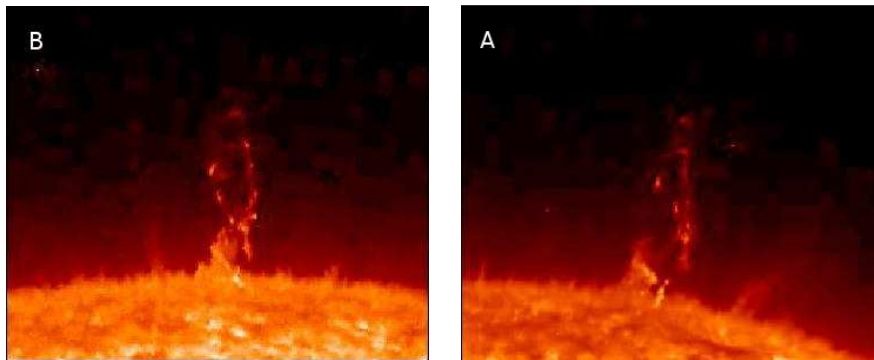


Figure 2.6: The helical jet event on 2nd February, 2008.

solved as supported by the cases when the jets widths was similar imaged from both perspectives (*e.g.* events n° 20–21–29–67–74 in the catalogue A.1). This is what one expects for jets that are to first order azimuthally-symmetric structures, *i.e.* invariant by rotation, so that they show the same width from different viewpoints. Contrary, a slab-like geometry would lead to significantly different widths for different perspectives. A detailed study of these characteristics would provide further insight into the validity of 3D models invoking magnetic twist as compared to models which are invariant by translation.

A surprise during the detailed study of the jet morphologies was to find events that revealed the same morphology as typically large-scale three part structured CMEs, consisting of a bright leading edge, a dark void and bright trailing edge (being the prominence material) but on much smaller scales. Fig. 2.7 shows a micro-CME at 304 Å occurred on 6th May, 2007: a bright small loop emerges from the solar limb and propagates through the low corona, keeping its loop shape, which mark the presence of the leading edge, followed by a region of dark void, in a similar way as found for large scale CMEs.

Another sample jet event (n° 41 of the catalogue in A.1) shows the appearance of a twisted small-scale prominence at 304 Å arising from inside the south coronal hole on 12th October, 2007 is presented in Fig. 2.8. Such twisted prominences are well observed features on much larger scale (<http://sohowww.nascom.nasa.gov/gallery/bestofsoho.html>). The spacecraft’s angular separation at that time was  $\Delta\phi_{AB} \simeq 35.84^\circ$ . The difference in the viewpoints is obvious and confirms that it is a real twisted 3D loop.

It seems likely that the overall magnetic topology depends on the source region characteristics of the underlying photospheric magnetic field as in the case of large-scale CMEs found to arise from bipolar magnetic field regions on

### 2.3 Typical morphology of coronal jets

---

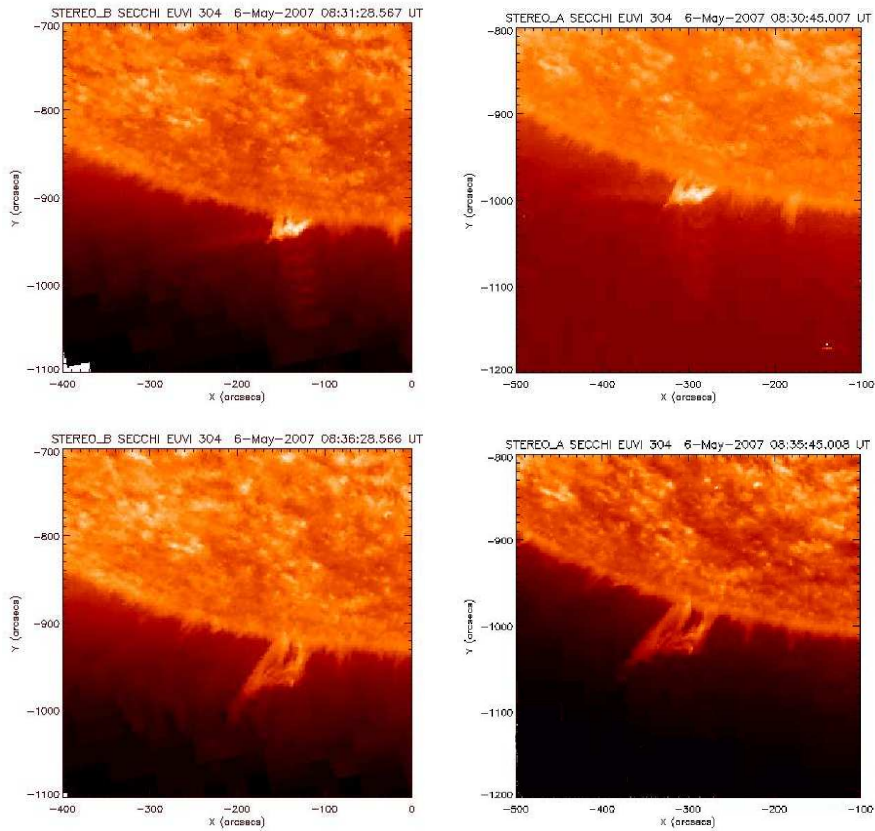


Figure 2.7: Micro-CME on 6th May, 2007 (event n<sup>o</sup> 15), at 304 Å seen by STEREO B (left) and A (right). The angular separation between the spacecraft was of  $\Delta\phi_{AB} \simeq 6.78^\circ$

larger scale as shown by (Cremades & Bothmer, 2004). Similar to the large-scale CMEs the micro-CMEs evolve from bipoles with enhanced magnetic flux compared to the surrounding fields but on much smaller scales. This is similar to the observation that coronal jets seem to arise close to small bipoles within the coronal holes as shown by (Shimojo *et al.*, 1996). However it is beyond the scope of this study to fully investigate the coupling of the coronal and photospheric structures. Overall we found evidence for 5 micro-CMEs in the total set of 79 events.

The list of coronal jet events provides information on the identified morphology of the individual events. However, it should be pointed out that in a number of events a unique classification was not possible because sometimes the jet features were different in each wavelength and sequences at different time cadences had to be investigated as indicated by a question mark in the Appendix A.1.

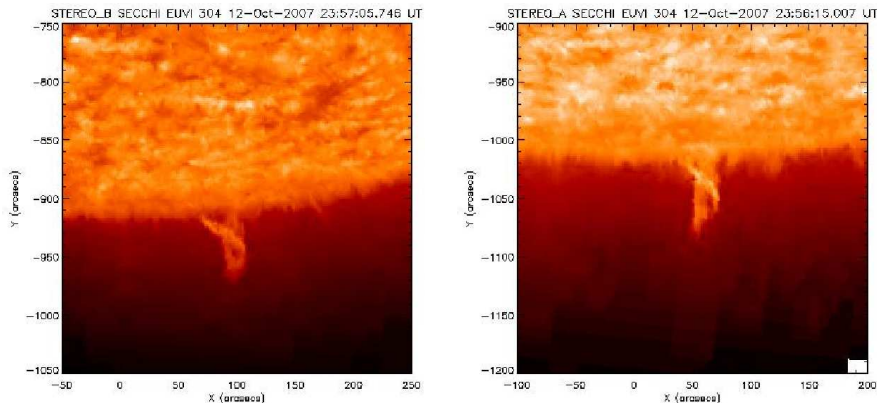


Figure 2.8: Images of twisted prominence material in the trailing portion of a micro-CME observed on 12th October, 2007.

## 2.4 Coronal jet lifetimes

Inspection of the polar jets reported in the catalogue A.1 also allows to obtain some basic information about the duration of observation in the EUVI field of view, *i.e.*, about the lifetime of the jets at the different wavelengths in the low corona. These EUVI visibilities correspond to the lifetimes given in the third column of the catalogue for each wavelength. A statistical distribution for the lifetimes of all jets at the different wavelengths between  $1-1.7 R_{\odot}$  in bins of 10 minutes is presented in Fig. 2.9.

It should be noted that the estimated lifetime is influenced by the different cadence times with which the EUVI telescope operates: usually a time cadence of 2.5 min is used for  $171 \text{ \AA}$ , while the cadence is 10 min for  $195 \text{ \AA}$

and 304 Å. It can be seen from Fig. 2.9 that the lifetimes of the jets analysed in this study at 171 Å and 195 Å are peaked at 20 min, conversely, at 304 Å, the lifetime distribution is peaked at 30 min. The lifetime distribution at 284 Å is peaked at 20 min, but the statistics is lower. The differences

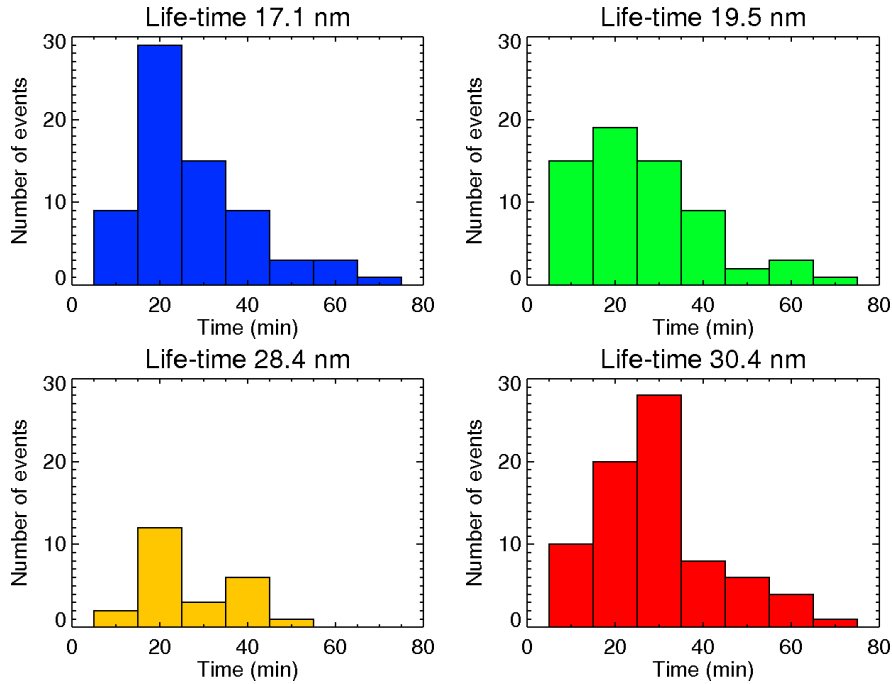


Figure 2.9: Distribution of the lifetime of coronal jets seen by STEREO/SECCHI at 171, 195, 284 and 304 Å. Note the shift of the peak in the lifetime distribution at 304 Å.

in lifetimes emphasize the fact that looking at different wavelengths implies observing the solar corona at different temperatures: the spectral line at 304 Å corresponds to lower temperatures ( $\sim 80,000$  K), which suggests that the duration of the event is usually longer at lower temperatures. On the other hand, the shorter lifetime at shorter wavelengths could also be related to the fact that the 171 and 195 Å jets have coronal temperatures ( $\sim 10^6$  K) and dim very fast with distance, since they travel in the hot corona and contrast is low. On the other hand, 304 Å jets have larger contrast since there is not so strong emission at this wavelength in the corona. With respect to the field of view of EUVI a given mean lifetime at a given wavelength corresponds to a certain speed, *i.e.* 171 Å plasma has an estimated outward propagating speed of about 400 km/s whereas 304 Å cooler material is moving at lower speeds of about 270 km/s, *i.e.* it is not capable to reach a speed sufficient to leave the Sun at the given height, so that material is falling back similar to spicula matter, as can be noted in some events (*e.g.* n° 14–15–71–73).

The escape speed from the Sun at the distance of  $1.7 R_{\odot}$  is  $\sim 360$  km/s.

An estimate of the lifetimes can also be obtained from the coronagraph observations. In COR1 A the peak of the distribution is centered near 70 min, while in COR1 B the peak of the distribution is centered near 80 min. A lifetime of 75 minutes for the field of view of COR1 corresponds to a speed of about 390 km/s which is in good agreement with the speed derived for the hot  $171 \text{ \AA}$  plasma components of the jets. The fact that the estimated lifetime in COR1 B is higher by ten minutes might be explained by its better stray-light rejection.

## 2.5 Analysis of jet speeds

A more detailed analysis of the kinematics of jets can be obtained from image data, following directly the motion of the plasma of the jet. Several strategies can be applied for obtaining speed measurements of the propagation of jets from the Sun, depending also from the quantity of data available. Furthermore, thanks to the capability of STEREO of obtaining images from two different point of view, knowing the “true” direction of the jet in space it is possible to infer the true speed, avoiding issues related to the projections effects along the line of sight.

A first method consists in tracking the position of the jet in time. The position of a specific feature of the jets is measured for several images and the distance is plotted as a function of the time. Since jets evolve in time and change their shape and structure, following the same volume of plasma is really difficult. For this reason, one could track the position of the leading edge, which delineates the visible outer propagating front of the jet. Some measurements of the leading edge (LE) position in time are shown in Fig. 2.10 for the micro-CME, n° 15 of the catalogue in the Appendix A.1 (see Fig. 2.7), and in Fig. 2.11 for the equatorial jet n° 10 of the catalogue in the Appendix B.1 (see also Fig. 2.2). In the former case, the position of the LE is calculated in 3D starting from images of STEREO A and B at  $304 \text{ \AA}$ , using the routine of the SSW package `scc.triangulate`. A parabolic fit yields a maximum jet speed of  $\sim 200 \text{ km s}^{-1}$ , consistent with the estimates at  $304 \text{ \AA}$  in previous section. Also, the inferred (sunward) acceleration is less than the solar gravity, which shows that electromagnetic forces are still acting on the jet material.

In the latter case, the position of the LE is inferred only from STEREO-B images, since the equatorial jet is visible only from this spacecraft. The radial position suddenly grows within 7.5 minutes (between 15:45:54–15:54:24 UT). The slope of the curve during this time-interval yields an estimate of the average speed of about  $180 \text{ km s}^{-1}$ . We fitted the points of the slope for two different time intervals with two quadratic polynomials, in order to calculate the initial speed and the phase of constant acceleration. The

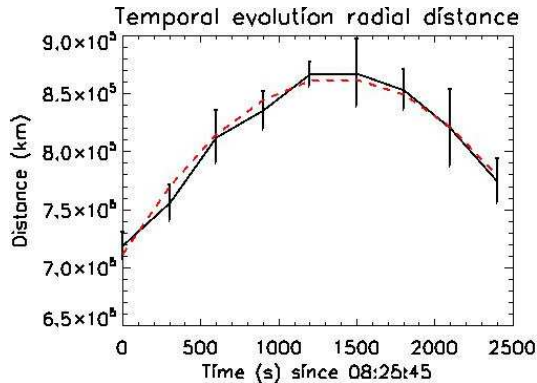


Figure 2.10: Evolution in time of the 3D leading edge position of the micro-CME on 6th May, 2007 (left) along the radial direction.

first fit, before the impulsive growth of the jet (until 1400 s), yields an initial speed  $v_{01} \sim 16.93 \text{ km s}^{-1}$  and an acceleration  $a_{01} \sim 0.00043 \text{ km s}^{-2}$ . From the second fit (1400 to 2700 s), we obtain  $v_{02} \sim 213.94 \text{ km s}^{-1}$  and  $a_{02} \sim -0.11 \text{ km/s}^{-2}$ . As can be seen from Fig. 2.10(right), the fitting curves are within the error bars. A similar two-phase height-time plot was found for the polar jet analysed by Patsourakos *et al.* (2008). Such a development can be interpreted as a first slow phase corresponding to a plasma instability build-up, whereas the second phase could correspond to the impulsive relaxation of the build-up energy, triggering the impulsive eruption of the jet. The acceleration determined for the second phase is negative, indicating a deceleration of ejected material at higher coronal altitudes, however being smaller, in absolute value, than the solar surface gravity ( $g_{\odot} \sim 0.270 \text{ km s}^{-2}$ ). This acceleration discrepancy suggests that some other force, beyond gravity, (either the pressure gradients or  $\mathbf{j} \times \mathbf{B}$  force) has accelerated the plasma. The obtained speeds and acceleration are similar to those found for a larger sample of jets discussed by Nisticò *et al.* (2009). In particular the downward acceleration for the polar jet was found to be  $\sim -0.160 \text{ km s}^{-2}$ , leading to similar inferences on the presence of additional forces beyond gravity.

Another method consists to make time-distance maps (*e.g.*, see Cirtain *et al.*, 2007; Savcheva *et al.*, 2007): the variation of the intensity along a straight line lying on the jet axis is plotted as stacked columns of several frames. In this way, a representation of the intensity variation in distance and time is created. The intensity variation provides us information on the possible speed and acceleration of the jet by simple linear or quadratic fit. The analysis is reliable when a considerable number of data points is considered. The time cadence of the STEREO images does not usually allow to create very nice time-distance maps. The typical cadence is of the order 2.5

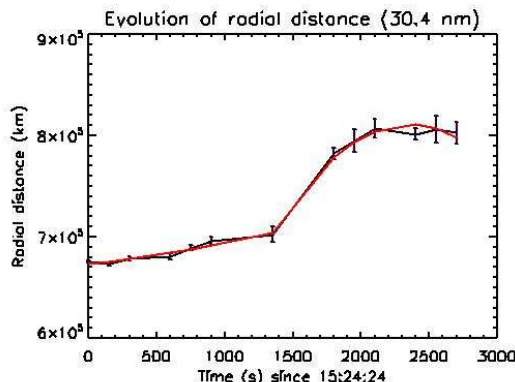


Figure 2.11: Evolution in time of the leading edge position for the equatorial jet on 11th November, 2007, seen from STEREO B at 304 Å.

minutes at 171 Å, and 10 minutes at 195 and 304 Å, which is comparable with the jet duration (20–30 minutes), excepts for the periods on 5th–19th May, 2007, and 7th–20th January, 2008, during which the SECCHI instruments worked with a high cadence resolution of almost 37.5 s at 304 and 75 s at 171 Å respectively. Fig. 2.12 gives images (first two figures from the left) and time-distance maps (last two figures on the right) for the jet happened in the North coronal hole on 9 May, 2007, at 304 Å. We plotted a straight line along the axis of jets in both images from STEREO B and A (the extreme points of the line where found with the routine `scc_measure`). The intensity variation in time along this line is represented in the form of time-distance maps for STEREO B (third figure from the left) and STEREO A (last figure from the left right). We over plotted a white line, whose slope gives an indication of the speed affected by projection effects: the speed is estimated of about  $107 \text{ km s}^{-1}$  in STEREO B, and  $100 \text{ km s}^{-1}$  in STEREO A. By making triangulation of the corresponding positions at a given time, as inferred from time-distance maps and jet images, by the routine `scc_triangulate`, we have the speed of the jet in 3D. More precisely we obtained the values of the  $x$ ,  $y$ , and  $z$  component of the speed in the Heliocentric Earth Equatorial (HEEQ) coordinate system:  $v = (151.77, 41.33, 96.57) \text{ km s}^{-1}$ . The corresponding magnitude is  $184.57 \text{ km s}^{-1}$ , with an accuracy of the estimate of less than the 10%. The same analysis is made for the event on 9th January, 2008 (event n° 71 of A.1), occurred during the period of high temporal resolution at 171 Å. The slopes of the profiles in time-distance maps (Fig. 2.13, third and fourth image from the left), return an apparent speed of about  $136.12 \text{ km s}^{-1}$  in STEREO B, and  $202.51 \text{ km s}^{-1}$  in STEREO A (the jet is also less clear in STEREO B than in A). By triangulation, the components of the speed are  $v = (-38.64, 55.05, 167.19) \text{ km s}^{-1}$ , and the corresponding

## 2.6 3D reconstruction

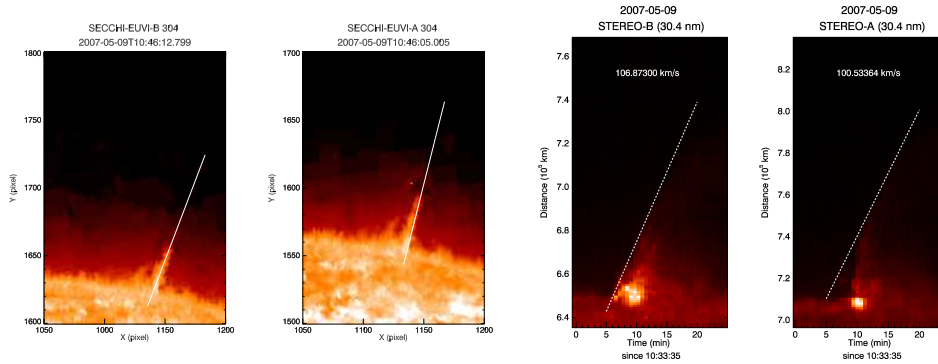


Figure 2.12: Images and speed jet profiles for the polar jet n° 17 of the catalogue in [A.1](#)

magnitude is of  $180.21 \text{ km s}^{-1}$ . The magnitude of the speed is less than the apparent speed estimated in STEREO A: indeed, the accuracy of the estimate by triangulation is about the 25%, since the jet appears less bright in STEREO B than in A, and this can affect the correct identification of the leading edge for making the triangulation.

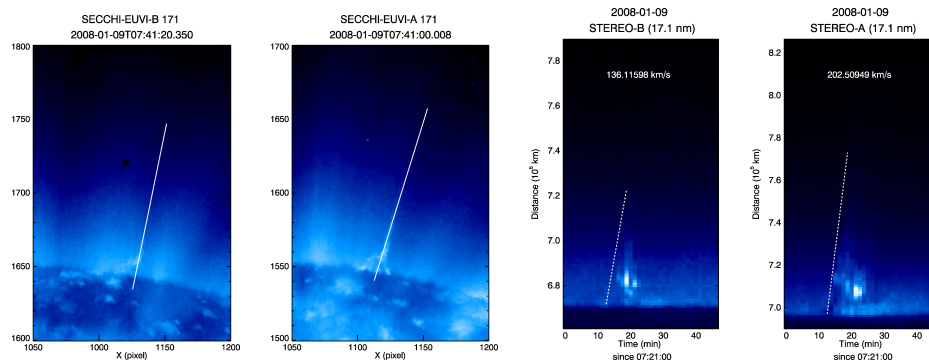


Figure 2.13: Images and speed jet profiles for the polar jet n° 71 of the catalogue in [A.1](#)

## 2.6 3D reconstruction

A unique feature offered by the twin spacecraft STEREO mission is the possibility to perform a three-dimensional reconstruction of coronal structures. Such a reconstruction is most reliable when the angular separation between STEREO A and STEREO B is less than 50 degrees ([Kaiser \*et al.\*, 2008](#)). An interesting example is offered by the jet of 12th October, 2007



(event n° 41 in A.1) that clearly shows an helical structure in Fig. 2.8 at 304 Å. For this event the spacecraft separation was  $35.34^\circ$ . We manually selected

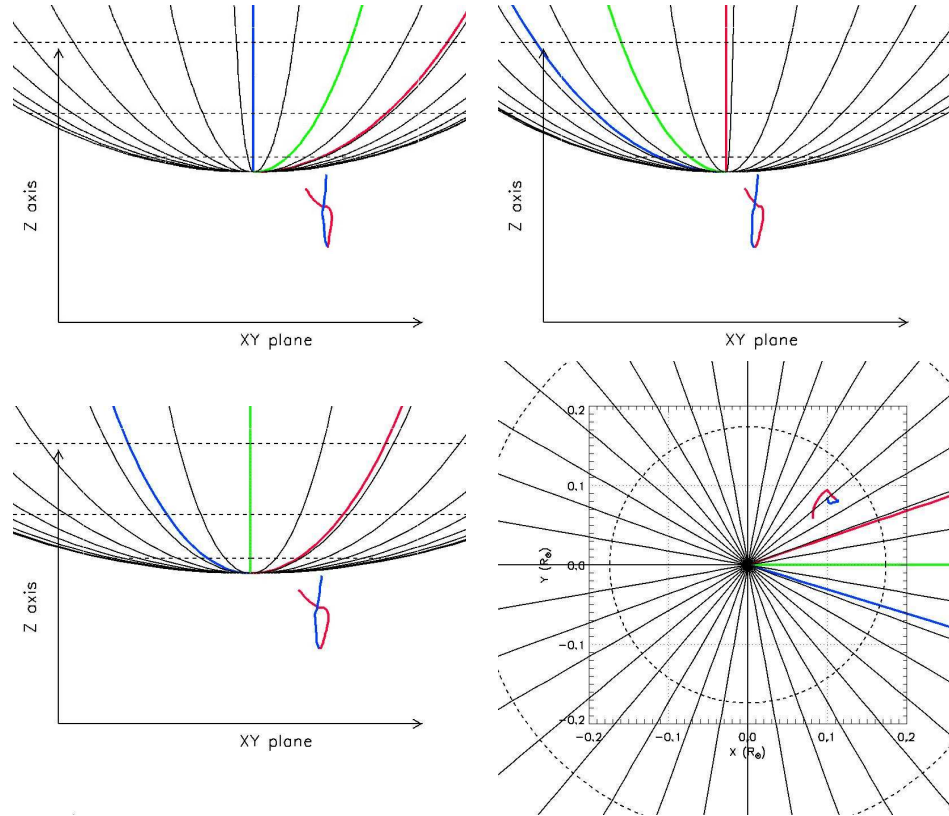


Figure 2.14: Reconstruction of the helical jet observed near the south pole on 12th October, 2007 (n° 41 of the jet list, Fig. 2.8). The spacecraft angular separation was  $35.84^\circ$ . The reconstructed jet is shown from three different viewing angles: STEREO B view (middle-left), STEREO A view (middle-right), and Earth point of view (bottom-left). The North solar pole view is shown (bottom-right). The coloured meridian lines stand for the different central meridians seen by STEREO B (blue), the Earth (green) and STEREO A (red).

10 points in the jets seen in STEREO A and B corresponding to the same feature. Then, the triangulation of these points allowed us to determine the 3D position of each point by the routine `scc_measure` of the SSW package. Finally, we interpolated the 3D points with the `EUVI_SPLINE1` function, obtaining 77 points, for smoothing the jet shape. For better emphasizing the 3D structure of the jet (Fig. 2.14), we coloured the two jet strands differently: the strand in front in STEREO B is in red and the other, behind, is in blue. The 3D reconstruction results show that the helical structure is a real physical feature of the jet and not an effect due to the projection on a

2D image.

## 2.7 Summary

In this chapter we presented the first comprehensive statistical study of polar coronal jets with the SECCHI instrument package on the STEREO spacecraft, using EUVI A and B and COR1 A and B data. A catalogue of 79 jets identified from simultaneous EUVI and COR1 coronagraph observations by both spacecraft has been compiled. The observations were taken during a period at solar activity minimum from March 2007 to April 2008. At the same time, 15 jets were found in middle latitude or equatorial coronal holes. From a systematic investigation of the 79 events observed by both spacecraft at separation angles between 2 and 48 degrees we find the following basic properties of coronal jets:

- there are 37 *Eiffel tower* type jets in which jets show a shape similar to an Y-inverted and they are associated to the magnetic configuration of a small magnetic bipole reconnecting with the ambient coronal field at its looptop;
- 12 *lambda* type jets in which ejection is observed to be shifted from the position of a bright point or a small loop, and this topology is associated to the magnetic configuration of a small bipole reconnecting with the unipolar coronal field at its footpoint;
- besides the previous two morphologies there are 5 micro-CME type events characterized by the evidence of a small loop that elongates from the solar surface and resemble to the CMEs but on smaller scale.

Without more sophisticated analyses of jets it is difficult to provide a reliable interpretation why we have identified about three times more ET than  $\lambda$  events. ET events at looptops are likely have better visibility against the background compared to reconnection processes happening at the footpoints because those appear bright and heating processes are less visible. Another plausible interpretation would be that ET-type jets could require some build-up of magnetic energy and then an instability like discussed by [Patsourakos \*et al.\* \(2008\)](#); [Pariat \*et al.\* \(2009\)](#). Therefore, whenever they occur more energy has been stored and therefore released and the jets are more bright, thus more detectable. On the other hand,  $\lambda$  jets can occur more “easily” without so much energy been stored, and therefore are less observable, even maybe more numerous.

Overall there are 31 events that clearly exhibit a helical structure of the magnetic field. It is important to note that these findings imply that a jet observed by a coronagraph at heights of  $\sim 1.5 R_{\odot}$  can have different low coronal onset scenarios in terms of the magnetic fields structure and its evolution.

The typical lifetimes in the EUVI FOV are 20 minutes at 171 Å, 30 minutes at 304 Å, while in COR1 the lifetimes are peaked at around 70–80

minutes. The corresponding speeds with respect to the FOV of the EUVI and COR1 telescopes are 400 km/s for the hot 171 Å plasma component and only 270 km/s for the cooler 304 Å chromospheric component observed as the jet trailing part. The speed of 400 km/s is comparable to that derived from the COR1 FOV of 390 km/s. In summary we conclude that the cooler chromospheric material in coronal jets commonly falls back to the Sun whereas the hotter leading flow caused by reconnection of fields escapes to larger heights as a jet subsequently visible in COR 1 images.

The present catalogue can serve for several purposes. One is to undertake a more detailed study of specific events to determine the 3D velocity and acceleration and to carry out a 3D reconstruction of the jet, to compare with numerical simulations. A second purpose is to look for the association between jets and other chromospheric phenomena, like spiculae, plumes, etc., (Raouafi *et al.*, 2008) which is useful for constraining more complete physical models of the solar activity in the coronal holes. A third purpose is to fill the gap between large scale coronal phenomena like CME and the small scale phenomena in polar coronal holes. A fourth use is done in Chapter 5, where the jet catalogue is used to study the magnetic deflection of jets and their North-South asymmetry.

## Chapter 3

# The maps of temperature of jets

Determining the conditions of the coronal plasma (*i.e.*, temperature, density, magnetic field, etc., ...) is a meaningful and important step for understanding the physics of the solar corona, and also for validating models and theories. Until now, it is not possible to obtain information of the state of plasma in the corona from in situ measurements (there is not spacecraft able to approach so close to the Sun), but a diagnostic of the corona comes from spectroscopic analysis of emission lines, EUV or X-ray emission, coronagraph observations, with the resulting uncertainties. Here we show temperature measurements for some jet events inferred from EUV STEREO/SECCHI data, using the technique of the filter ratio method at 171 and 195 Å, and applying a technique for subtracting the EUV background radiation. The results show that jets are characterized by electron temperatures ranging between 0.8–1.3 MK. We present the thermal structure of the jet as temperature maps and we describe its thermal evolution.

### 3.1 Temperature measurements in the solar corona

Temperature represents an important parameter which is necessary to know in order to determine the state of the coronal plasma. Temperature measurements generally come from spectroscopic analysis. According the characteristics of the emission lines of a given chemical element, it is possible to know the degree of ionization. Indeed, the million Kelvin degree temperature of the corona was established in the 1940s, associating the several emission lines to iron atoms highly ionized. The line width and the shift of an emission line can give us an estimated of the density and velocity of the plasma. On the other hand, to obtain such measurements is not so immediate, since it is necessary to sample the emission line profile; moreover, this kind of measurements are spatially limited.

Another way for obtaining temperatures estimates in the corona comes from extreme ultraviolet or X-ray image data. Telescopes that observe the corona at wavelengths that fall in this range, like EIT aboard SoHO , EUVI on STEREO spacecraft, SXT and XRT from the Japanese missions Yohkoh and Hinode, use narrowband filters that allow to take images of the corona: each filter selects a specific wavelength that corresponds to a fixed ionization degree of a particular elements, and so a relatively narrow range of temperature can be assigned. In the Table 3.1 we reported the corresponding ionized elements and the electron temperature for the typical wavelengths of the EIT and EUVI instruments. Even if some analysis and image pro-

Wavelength ( $\text{\AA}$ )	Element	Temperature ( $10^6$ K)
304	He II	0.7
171	Fe IX/X	1.0
195	Fe XII	1.5
284	Fe XV	2.0

Table 3.1: Typical EUV wavelengths of the EIT and EUVI instruments corresponding to highly ionized elements and associated peak temperatures.

cessing are necessary for extracting temperature from image data, as well as some special assumptions, this kind of method is useful for analysing solar features that can happen everywhere on the Sun, without the constraint that the observed feature falls in the slit of a spectrometer. Then instruments as EIT and EUVI, and overall the AIA instruments aboard the SDO spacecraft, daily observe the corona with a cadence of the order of some minutes (AIA provides data every 75 seconds with high spatial resolution at several EUV wavelengths): this allow to monitor our object and studying it in great detail.

## 3.2 Temperature from EUV filters

Image data are simple matrices of pixels, each of them has a numeric value that give a measure of the intensity of photons at a given wavelength, that hit the CCD detector of the instrument. The intensity in image data is usually measured in Data Numbers (DNs) which is directly proportional to the number of incoming photons during the exposure time, *i.e.* the time in which the filter of the telescope is open (see also, [Aschwanden \*et al.\*, 2008](#), for some details). The intensity of each pixel depends on the characteristics of the instruments and the plasma observed. More precisely, intensity at a given wavelength  $\lambda$  is given by the convolution of two quantities: the response function of the instrument  $R_\lambda(T, A)$ , depending on the electron temperature  $T$ , the atomic physics processes (*e.g.*, ionization equilibria), the

### 3.2 Temperature from EUV filters

coronal abundances  $A$ , and the instrument calibration; the emission measure  $EM = n_e n_i h$ , which is a quantity that define the amount of plasma (electron and ion densities) along the line of sight  $h$ . Since the coronal plasma is fully ionized, we can suppose that  $n_e \sim n_i$ , and express the  $EM$  as the square of the density. If  $x$  and  $y$  indicate the pixels coordinates of a given image, we can write:

$$I_\lambda(x, y) = R_\lambda(T, A)EM(x, y) \quad (3.1)$$

In Fig. 3.1 response functions of EUVI for STEREO A and B are plotted as intensity (photons/s), given a value of  $EM = 10^{44} \text{ cm}^{-3}$ , in function of the temperature  $T$ . The response functions are obtained assuming the coronal abundances of (Feldman, 1992) and the ionization balance of (Mazzotta et al., 1998). It is possible to note that the instrumental response is not

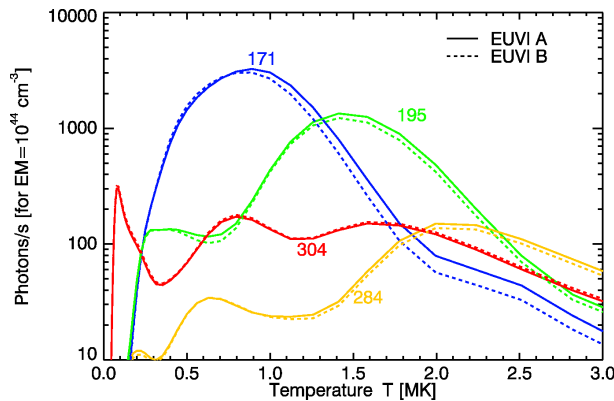


Figure 3.1: Response functions for the EUVI filters (171, 195, 284, and 304 Å) of STEREO A and B.

so narrow, but it shows a broad profile. This can create some ambiguities, since the intensity, emitted by a volume of plasma at a given wavelength, will not necessarily correspond to the peak of the response function, but could be associated with more values of temperatures, at least two. In the order to obtain reliable values of temperature, different strategies of analysis can be applied, according the physical assumptions made for solving the issue: we can consider that the emitting plasma is in *isothermal* condition, *i.e.*, it is associated with a unique value of temperature  $T$ ; or we can use a more realistic approximation of *multithermal* plasma.

#### 3.2.1 Isothermal plasma approximation: filter ratio technique

The isothermal approximation assumes that a specific volume of plasma, observed with two or more passband filters (*e.g.*, 171 and 195 Å), has a

unique value of electron temperature. Since it is not possible to assess a single temperature from one filter, as shown in the past section, at least two filters are usually used and the ratio of the intensities is taken into account. In other words, for a given volume of plasma, with pixel coordinates  $(x, y)$ , we have:

$$I_\lambda(x, y) = R_\lambda(T, A)EM(x, y) \quad I_{\lambda'}(x, y) = R_{\lambda'}(T, A)EM(x, y)$$

where  $\lambda$  and  $\lambda'$  are two different passbands. Making the ratio of the intensity we will obtain a function  $Q(x, y)$ :

$$Q_{\lambda/\lambda'}(x, y) = \frac{I_\lambda(x, y)}{I_{\lambda'}(x, y)} = \frac{R_\lambda(T, A)}{R_{\lambda'}(T, A)} = f[T(x, y)], \quad (3.2)$$

where we assume that the  $EM$  is the same at different wavelengths, because of the isothermal assumption. In Fig. 3.2, we plotted the ratio of the response functions as function of temperature respectively for  $Q_{195/171}$  (blue line),  $Q_{284/195}$  (green line),  $Q_{171/304}$  (red line). We can note that the trend of

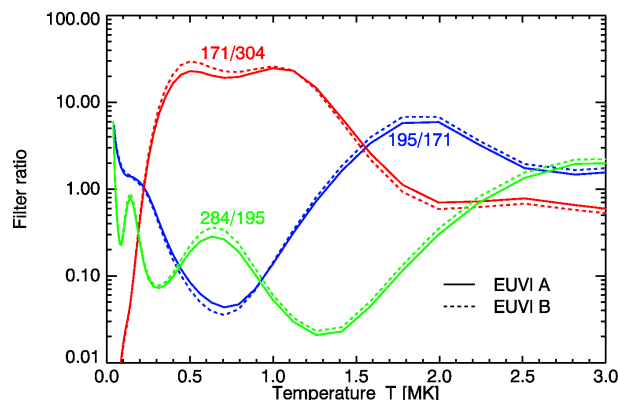


Figure 3.2: Ratio of the response functions respectively  $Q_{195/171}$ ,  $Q_{284/195}$ ,  $Q_{171/304}$ , for EUVI/STEREO.

the ratio of response functions  $Q_{\lambda/\lambda'}$  is not monotonic, but for a given value of the ratio is possible to find two (or more) corresponding values of the temperature. We can overcome this problem if we restrict, on the basis of physical expectations, the temperature range between the relative minimum and the maximum value where the filter ratio grows almost monotonically and the considered temperature range is approximately bounded by the peaks of the original response functions. The function  $Q_{\lambda/\lambda'} = f[T]$  can be easily inverted for obtaining a unique value of temperature  $T$  for a given value of the ratio intensity  $Q_{\lambda/\lambda'}$ .

Another possible way is to use three filters (Patsourakos & Klimuchuk, 2007), as described in Chae *et al.* (2002). Starting from two different ratio

### 3.2 Temperature from EUV filters

of filters, for example 195/171 and 284/195, it is possible to make a curve from a set of point  $c1$  and  $c2$ , where

$$c1 = \log(R(195) - R(171)), c2 = \log(R(284) - R(195)). \quad (3.3)$$

This kind of plot is name “*color-color*” diagram (see, Fig. 3.3): the set of points  $(c1,c2)$  form a curve on the plane  $c1, c2$ , in which a point corresponds to a unique temperature of EUV-emitting plasma, in an analogous way to the two filter ratio technique.

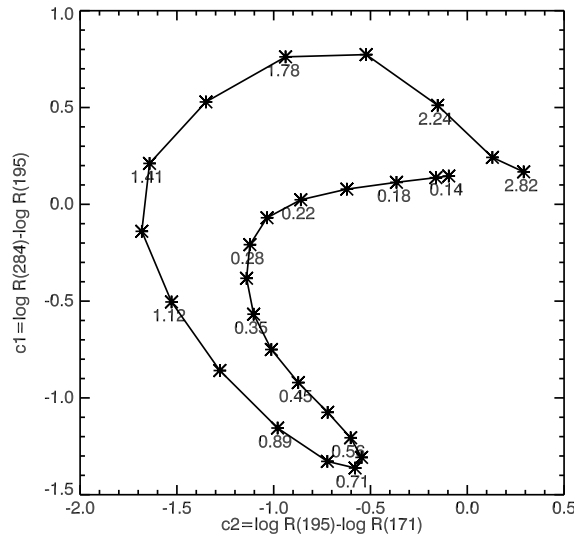


Figure 3.3: Color-color diagram for 171, 195, and 284 filters of STEREO/EUVI.

Furthermore, the isothermal approximation is supported also from the estimate of the collision time. The electron collision time  $\tau_{ce}$  is expressed as:

$$\tau_{ce} = 2.75 \times 10^{-1} \frac{T_e^{\frac{3}{2}}}{n_e \ln \Lambda} (\text{s}) \quad (3.4)$$

where  $n_e$  is the electronic density and it is measured as  $\text{cm}^{-3}$ ,  $T_e$  is the electronic temperature measured in K degrees, and  $\Lambda$  is the Coulomb logarithm. Assuming typical constant values of  $T_e = 10^6$ ,  $n_e = 10^8 - 10^9$ ,  $\ln \Lambda \approx 24 - \ln \frac{n_e^{\frac{1}{2}}}{T_e}$  for  $T_e \geq 10$  eV, obtaining  $\ln \Lambda \approx 27$ . By substituting these values into the expression 3.4, we obtain  $\tau_{ce} \approx 10^{-1} - 10^{-2}$ . On the other hand, the jet density is usually greater than that of the surrounding plasma (Dochek *et al.*, 2010). The electron collision time is much shorter than the



evolution time of the jet, and also shorter than most instability growth rates. Therefore the electron density at  $T_e \approx 10^6$  K is collision dominated, and we can safely assume that the electron distribution function is a Maxwellian.

### 3.2.2 Multithermal plasma approximation: DEM modeling

The isothermal model applied to calculate the temperature of a volume of plasma, corresponds to a simple modeling, but is actually oversimplified. A more realistic approximation comes from considering the plasma of solar corona characterized by a distribution of temperatures: one could think that a volume of plasma is filled by a several flux-tubes, each of them at a specific temperature, that cannot be solved because of the resolution of observational instruments, and they give a response in two or more filters. For this reasons, the concept of Emission Measure is substituted by the Differential Emission Measure ( $dEM(T)/dT$ ). A possible model for characterizing the  $dEM/dT$  or the corresponding differential density distribution  $dn_e(T)/dT$  is to take in consideration a Gaussian function of temperature (see, [Aschwanden, 2006](#), chapter3, pag. 76):

$$\frac{dn_e(\mathbf{x}, T)}{dT} = \frac{n_e(\mathbf{x})}{\sqrt{2\pi}\sigma_T} \exp\left[-\frac{(T - T_0)^2}{2\sigma_T^2}\right], \quad (3.5)$$

which defined by three parameters: the total electron density  $n_e(\mathbf{x})$ , the mean electron temperature  $T_0$ , and the Gaussian temperature distribution width  $\sigma_T$ . An example of DEM distribution modeling is also given in [Aschwanden \*et al.\* \(2008\)](#), for calculating temperature along coronal loops.

## 3.3 Temperature analysis for coronal jets: motivations

In the order to understand and to quantify the jet influence on the coronal dynamics and energy balance, also with respect to the question on how the solar wind is accelerated ([Ryutova \*et al.\*, 2001](#); [Madjarska, 2011](#)), it is necessary a quantitative analysis, in which physical parameters have to be determined.

There are many models which explain the origin and the morphology of jets ([Yokoyama & Shibata, 1996](#); [Moreno-Insertis \*et al.\*, 2008](#); [Pariat \*et al.\*, 2009](#)): jet formation is thought to be due to magnetic reconnection between a small magnetic bipole and the large scale open magnetic field of the coronal hole. The magnetic energy released during the reconnection is converted to bulk kinetic energy and thermal energy of the plasma and the different morphologies are explained by the different magnetic configurations in which magnetic reconnection can occur. By the way, a comparison between numerical simulation results and measurements is necessary for validating or

refusing a model. In this sense, a more precise determination of the temperature will help better to understand the physical process causing the origin and the evolution of jets, understanding if there any process of heating and where they happen. The results allow us to compare the thermal structure of jets with jet model calculations and results from numerical simulations.

In the next sections we show how we obtain temperature measurements from STEREO/EUVI data and we make a comparison with results from numerical simulation modeling.

## 3.4 Temperature analysis

### 3.4.1 Data processing

We give here an overview of the steps followed in order to prepare data for the temperature analysis. Data are downloaded in FITS (Flexible Image Transport System) format from <ftp://stereoftp.nascom.nasa.gov/pub/> at 171 and 195 Å and at specific times, as indicated in the table by (Nisticò *et al.*, 2009). Since we are interested to study also the time evolution of jet temperatures, we downloaded data covering a time range of almost one hour before and after the start time of the jet brightest eruption.

As a first step, FITS files are processed with `secchi_prep`, an IDL routine of the SSW package, which returns as output the header and the calibrated image arrays, normalized to the exposure time. Images have a dimension of 2048×2048 pixels. We identify the jet position and, if necessary, we perform a rotation of the solar disk in order to have the jet axis approximately parallel to the vertical axis of the entire image, in order to facilitate the background subtraction described below. Then, we apply the routine `euvi_fov` for selecting the FOV in which the jet is found and resize the full-resolution images. The resized images are smoothed by calculating 3×3 medians centered on each pixel (median filter) to reduce the noise. After these operations, data are ready for temperature analysis by the filter ratio-method.

### 3.4.2 The filter-ratio method

In order to calculate temperatures, we used the filter ratio method with the hypothesis of isothermal conditions, so that the present temperature measurements are preliminary. However, the isothermal assumption is not necessarily satisfied, so that in practice there are some uncertainties about the results obtained from this type of analysis (Schmelz *et al.*, 2003), in particular in the case of structures where the temperature (along the line of sight) is not constant.

We consider only two filters at different wavelengths (171 and 195 Å) and the corresponding ratio. The response functions of EUVI are plotted

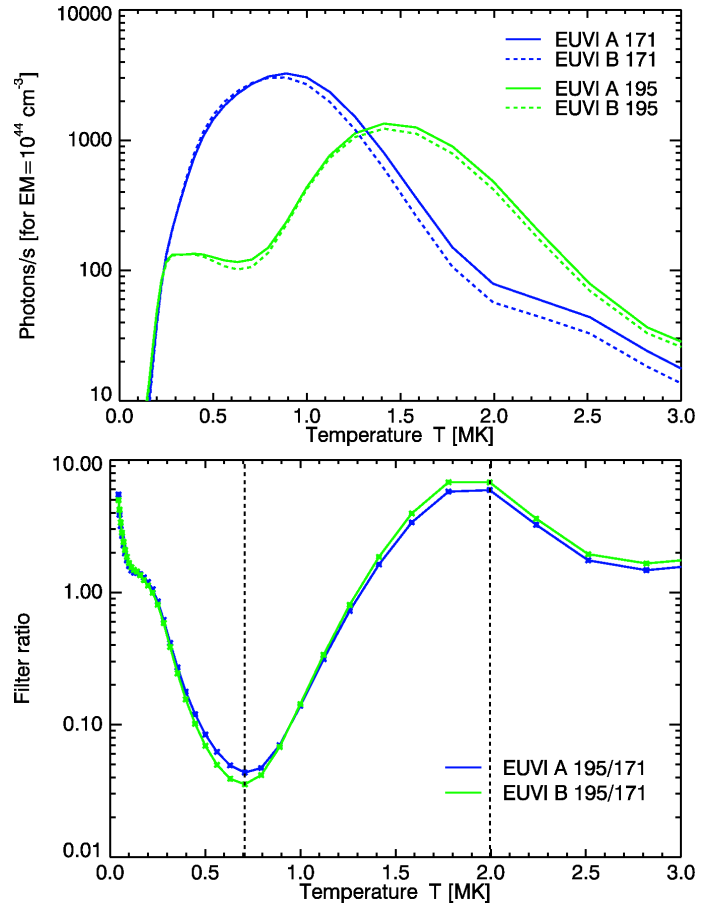


Figure 3.4: Filter response for the EUVI A and B (top) and filter ratio responses (bottom).

for a fixed  $EM$  in Fig. 3.4.2 (top), giving an indication of electron plasma temperatures to which the EUVI filters are sensitive (*e.g.* 1.0 MK at 171 Å, 1.5 MK at 195 Å). These functions have been calculated by the routine `euvi_response` of the SSW, assuming the coronal abundances of [Feldman \(1992\)](#) and the ionization balance of [Mazzotta \*et al.\* \(1998\)](#). However, one cannot uniquely determine which is the “*actual*” temperature for plasma observed “almost ” contemporarily by different filters (for instance in the range 1.0 or 1.5 MK for plasma observed at 171 and 195 Å). For solving this ambiguity we consider the ratio  $Q(x, y)$ :

$$Q(x, y) = \frac{I_{195}(x, y)}{I_{171}(x, y)} = \frac{R_{195}(T, A)}{R_{171}(T, A)} = f[T(x, y)] \quad (3.6)$$

where we assume that the  $EM$  is the same at different wavelengths, *i.e.* we observe an isothermal volume. If we focus on the 195/171 ratio (blue and green line in Fig. 3.4.2, bottom) we note that the trend is not monotonic, but for a given value of the ratio is possible to find two (or more) corresponding values of the temperature. We can overcome this problem if we restrict, on the basis of physical expectations, the temperature range between  $\sim 0.7 - 2.0$  MK where the filter ratio grows almost monotonically; further, this temperature range is approximately bounded by the peaks of the original response functions. Because the filter ratio function is tabulated on  $k$  discrete points, we perform a linear interpolation for determining the temperature  $T(x, y)$  corresponding to an empirical value  $Q(x, y)$  which falls in an interval  $[Q_k(x, y), Q_{k+1}(x, y)]$ .

#### 3.4.3 The background subtraction

A crucial aspect for the temperature determination is the background subtraction: this is necessary in general for separating the jet-plasma from the background and foreground plasmas in the optically-thin corona, since the corresponding emission could affect the image and invalidate the temperature estimates. Background subtraction was applied for temperature analysis of coronal loops ([Schmelz \*et al.\*, 2003](#); [Aschwanden \*et al.\*, 2008](#); [Terzo & Reale, 2010](#)) and several methods were applied and their corresponding problems were also discussed ([Aschwanden \*et al.\*, 2008](#)).

A simple method for eliminating the background contribution is to compute the difference between consecutive images. However we do not adopt this method because the cadence of images is comparable with the jet lifetime ( $\sim 10$  minutes) and jet features could be removed by the difference operation. Indeed, in our analysis we use 195 and 171 Å image data (typical cadence 10 and 1.5 minutes respectively) close in time (usually the time difference is 30 seconds or 1 minute) for filter ratio analysis: we do not take into account the observations at 284 Å, even if the three filter technique would allow to solve some ambiguities, because the cadence is lower (20 minutes).

Instead, for estimating the background, we make a linear fit of the EUVI intensity outside of the jet area.

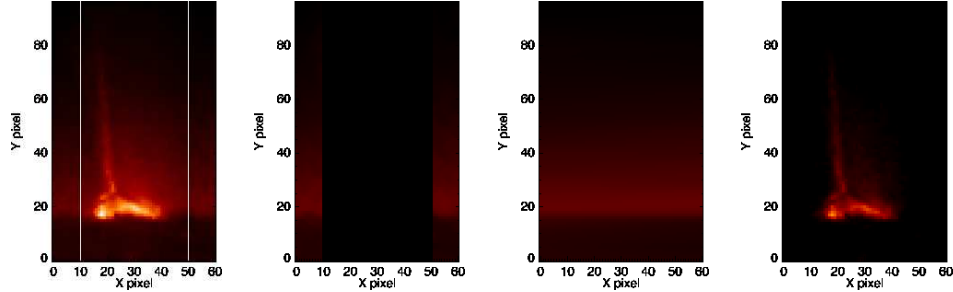


Figure 3.5: Images showing the procedure for background subtraction (see text).

In Fig. 3.5 we exemplify in four steps our procedure, which has been carried out on every single image for each filter:

1. selection of background pixels of the noise-removed image in the neighbouring area of the jet, although distinct from the jet itself: these pixels are at the sides of the jet location (1<sup>st</sup> panel from left: background pixels are enclosed between the image borders and the vertical white lines);
2. removal of the center pixels from the original image (center-left panel);
3. linear fitting of the background pixels along the  $x$ -direction for each  $y$  pixel and interpolation on the “void” pixels (center-right panel);
4. subtracting the “real” image and the “synthetic” background (right panel)

We point out that the background contribution is rather large with respect to the total intensity: if we consider the emission of the background compared to the total flux in the region affected by the presence of the jet (Fig. 3.5), we find that it represents  $\sim 35\%$  of the total flux, almost at the basis of the jet ( $y = 20$  pixel), and  $\sim 55\%$  at middle height ( $y = 40$  pixel) at  $171 \text{ \AA}$ , and respectively  $\sim 15\% - 20\%$  at  $195 \text{ \AA}$ .

After the background is subtracted for both the  $195$  and the  $171 \text{ \AA}$  images, we apply the filter ratio method for each pixel as described above, yielding a temperature map. The error on the computed temperatures depends on how well the background is subtracted. If we consider some points of the Fig. 3.5, for example  $(x, y) = (18, 18)$  and  $(x, y) = (20, 40)$  in pixel coordinates, typical percentage error values on the background are  $2.5\%$  and  $< 1.0\%$  respectively for  $171$  and  $195 \text{ \AA}$ , calculated considering the root-mean-square (RMS) in the background side regions. If we propagate these

### 3.5 Temperature determination results

errors, we obtain a typical percentage error on temperature of about 1.0%, but the uncertainties of the method and of the instrument calibration can add further errors which are difficult to quantify. On the other hand, we exclude pixels that have, after the background subtraction, values below three times the standard deviations. This is necessary for avoiding to obtain pixels with high values of temperatures (usually saturated to the maximum value of the filter 1.95 MK), resulting from the ratio between two imperfect subtracted background intensities, which are not associated with any physical heating process.

We want to remark that the method adopted here is not necessarily better than other ones discussed in literature: for instance, in the loop temperature determination, *e.g.* by [Aschwanden \*et al.\* \(2008\)](#) a 1-D geometrical shape is assumed for describing the the loop structure. However, we do not consider a geometrical configuration for jets since they are more difficult to model and they also show different shapes. We are trying to build an iterative procedure that possibly works for many jet-events and also in which the selection of the background is more possibly observer-independent.

### 3.5 Temperature determination results

Here we apply the procedure, described in the previous section, to two events. In Fig. 3.6 we show a temporal sequence of intensity images at 171 Å

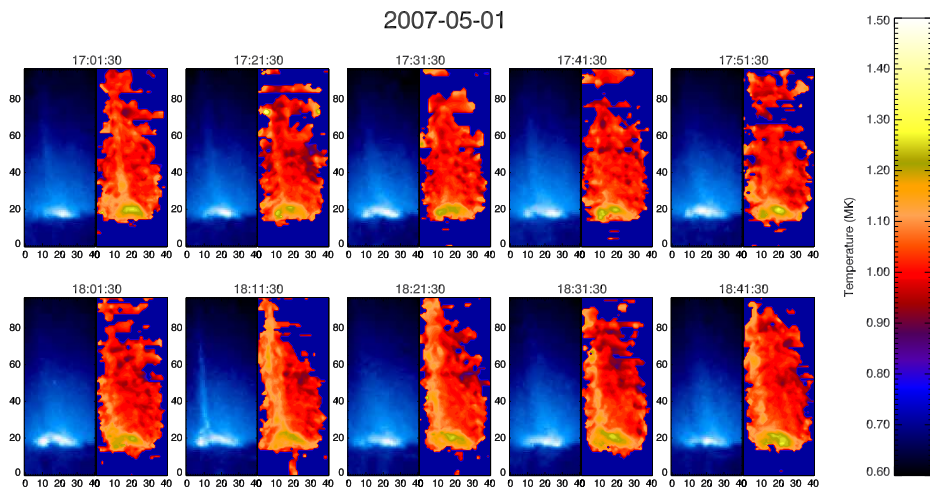


Figure 3.6: Sequence of intensity (in logarithmic scale) at 171 Å (left panel) and temperature maps (right panel) for jet occurring on 1st May, 2007.

Å and the corresponding temperature maps (from top-left to bottom-right) of an ET-type jet which took place on 1st May, 2007, seen by STEREO A. This event is n°10 in the catalogue of the Appendix A.1. This jet is

also shown in Fig. 3.5 at  $171 \text{ \AA}$  during the ejection phase: we note the bright loop footpoints and the ejection coming up almost from the center of this loop. The sequence of temperature maps cannot closely follow the thermal evolution of the jet in time, since maps are made at intervals of 10 minutes because of the cadence of the  $195 \text{ \AA}$  filter. As can be seen from the colorbar, temperatures range from  $0.70 \text{ MK}$ , corresponding to the lowest temperature value estimated with the present technique, to  $\sim 1.50 \text{ MK}$ . More than the temperature values themselves we aim at highlighting the thermal structure of the event: the basis of the jet, corresponding to the bright point or loop visible in intensity images, shows higher temperature than the narrow ejection and a temperature gradient recognizable from the interior to the exterior of jet. Temperature maps clearly pick up the jet base while this also applies to the jet body but in a somehow less clear manner. In the first image it is possible to recognize an ejection, coinciding with the pre-jet, *i.e.* a smaller eruption visible almost 1 hour before the main ejection at 18:11 (see A.1). It is possible to identify other ejections before the main ejection: this give us an indication that the event is recurrent in time, *i.e.* this could be related to a recurrent unsteady reconnection process between the small loop of the jet basis and the ambient field, so that the intensity of the jet varies in time and hot plasma continuously flows to the corona. The footpoints of the jet evolve in time: two hot spots appear (2nd map) which could be identified with plasma heated by magnetic reconnection process. Next, the main, brightest ejection is noted in the 7th map. With respect to the pre-jet, the ejection shows a higher temperature and hot plasma lifts-off.

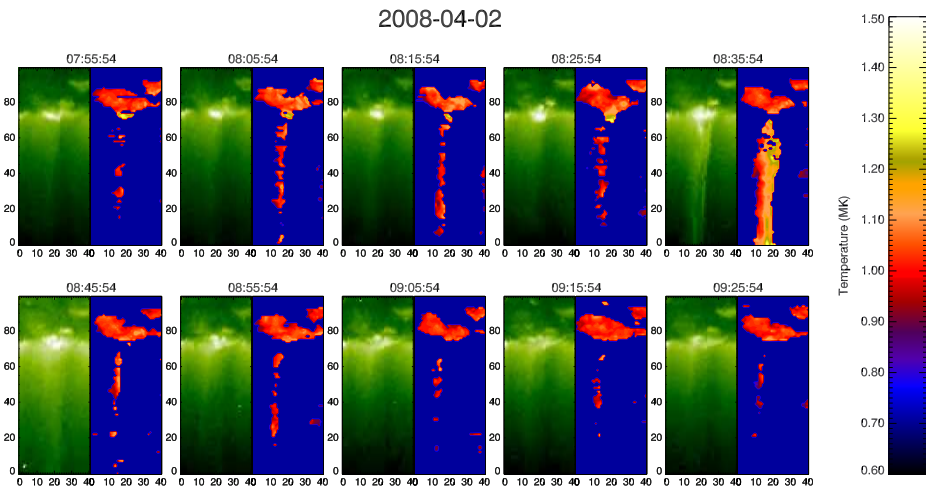


Figure 3.7: Sequence of intensity at  $195 \text{ \AA}$  (in logarithmic scale) and temperature maps for jet occurring on 2nd April, 2008.

Fig. 3.7 shows a sequence of intensity images at  $195 \text{ \AA}$  and the corre-

sponding temperature maps for the jet detected at the South pole on 2nd April, 2008 (n° 75 of [A.1](#)), seen by STEREO B. A bright feature is noted on the limb, similar to a small loop and the ejection clearly appears in the fifth image (same order as in [Fig. 3.6](#)) at 08:35, showing the hot basis of the jet and the plasma ejected: we note the footpoint of the jet associated with temperature of about 1.00–1.10 MK. The jet body is thermally structured: the left part is coloured in red which indicates a temperature around 1.0 MK, according the colorbar scale, the right part is hotter with temperatures between 1.10 and 1.30 MK. Compared to the event in [Fig. 3.6](#), temperatures are similar for the jet body, even if the basis seems to have lower temperatures. This could be due to a bad perspective from STEREO B, so that the loop-basis is not seen entirely and we cannot detected the full thermal evolution. In the other maps, before and after the main ejection at 08:35, some plasma blobs are recognized along the jet axis. This can be interpreted as a signature of recurrent reconnection and continuous plasma outflow from the small loop at the basis to the corona.

The evolution of the temperature maps in [Fig. 3.6](#) and [Fig. 3.7](#) compares well with the numerical simulation of magnetic reconnection and jet formation by [Moreno-Insertis \*et al.\* \(2008\)](#). Indeed, a rather similar morphology (especially for the event of 1st May, 2007) of the temperature maps is obtained in the simulation: the left panel of [Fig. 3.8](#) shows a vertical cut at a specific time of the jet temperature distribution obtained from the simulations. It shows an Y-inverted shape, as pointed-out by [Moreno-Insertis \*et al.\* \(2008\)](#), and temperatures ranging from  $10^5$  to  $10^7$  K degrees. The higher temperatures are located at the X-point forming between the small dipole and the ambient field lines; the upflowing plasma from the reconnection site shows slightly lower temperatures, as well as, the plasma at the right side of the small dipole with temperature at  $10^5$  K (chromospheric jet). The thermal structure obtained by our analysis follows qualitatively the simulation, especially for the event of 1st May, 2007, except for the absolute temperature range; this is probably due to limited over a narrow range temperature sensitivity both to the sensitivity of the filter ratio method and to the specific assumptions of the numerical simulation by [Moreno-Insertis \*et al.\* \(2008\)](#). We can distinguish a current sheet, whose position is close to the small loop, and then the jet body showing a gradient of temperature from one side to the other one. The same thing can be thought for the second event ([Fig 3.8](#), last plot on the right side), even if the temperature distribution at the basis of the jet is not well seen.

## 3.6 Summary

In this chapter we discussed how to obtain the electron temperature maps of jets seen by STEREO/EUVI, and have described the time evolution of



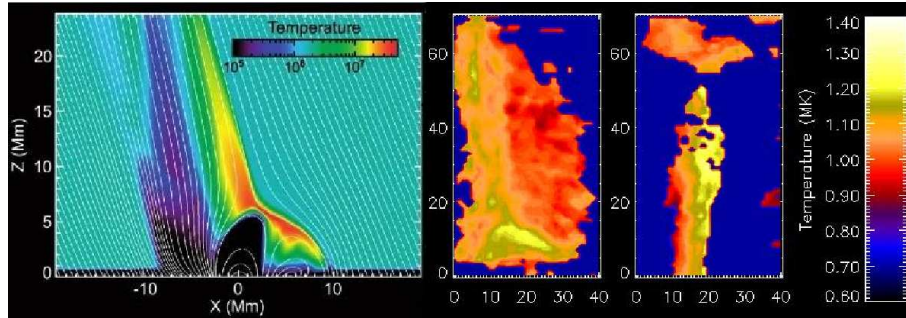


Figure 3.8: Temperature distribution comparison between numerical simulation (left) from [Moreno-Insertis \*et al.\* \(2008\)](#), and analysis by the filter ratio method for jets of 1st May, 2007 (center) and 2nd April, 2008 (right). Note that the color scale for the EUVI temperature maps is slightly different from that of [Fig. 3.6, 3.7](#).

temperature with the purpose to emphasize the jet thermal structure. To this end, we have used the filter ratio method to compute the temperature from EUV observations, and have provided a method to obtain 2-D temperature maps based on the estimation of the background at the sides of the jet region. Keeping in mind the uncertainties implicit in the method used, we obtain jet temperatures in the range 0.70-1.50 MK for two analysed jets. We point out that higher temperatures have been obtained for jets observed in the X-rays, see ([Shimojo & Shibata, 2000](#)). This is possibly due to the fact that jets can have a thermal structure similar to that of nested magnetic surfaces in toroidal plasma: the innermost layers have higher temperature and emit in the X-rays, while the outer envelope has lower temperatures and emits in the UV.

The temperature maps show that a thermal structure of the jet region is present up to 1 h before the jet's main ejection. This implies that heating and reconnection are going on in the jet well before the bright, collimated emission which is easily identified in EUV observation. The hotter temperature are located at the reconnection site between the small-scale dipole emerging from the photosphere and seen in EUV images as a small loop and the large-scale unipolar field of the coronal hole. It appears that the plasma, heated by the reconnection process, escapes following the magnetic field and it is ejected into the corona, redistributing the temperature along the jet body. Our analysis is in good morphological agreement with numerical simulation and this can provide a validation of the models used to explain the formation and evolution of corona hole jets (see, *e. g.*, [Gontikakis \*et al.\*, 2009](#)).

## Chapter 4

# North-South asymmetry in the magnetic deflection of polar coronal hole jets

The presence of magnetic fields on the Sun was shown by George Ellery Hale in 1908. By means of spectropolarimetric analysis and measurements of the splitting of spectral lines due to the Zeeman effect, he was able to assess that sunspots are characterized by strong magnetic fields of the order of 3000 Gauss, while the rest of the Sun shows magnetic fields of the order of 5–10 Gauss. From his studies on sunspot magnetic field, he established two empirical evidence: sunspots always appear in pairs of opposite polarity, with the trailing sunspot bent toward the equator; couple of sunspots in both hemispheres show inverted polarity. It was clear that solar activity cycle of 11 years, found studying the periodicity of the number of sunspots by Schwabe, is related to the presence and evolution in time of magnetic fields.

The discovery of magnetic fields on the Sun had a relevant consequence, mainly for the formulation of models able to describe solar activity and phenomena related to it, and for the development of a new field of research called magnetohydrodynamics, *i.e.* the study of plasma in the presence of magnetic fields. Since the Sun is made by ionized gas, there is a strong coupling between plasma and magnetic field and, especially in solar corona, the magnetic field controls the dynamics of plasma.

Measurements of the magnetic field in the interplanetary medium, of the sunspots area, etc., reveal a possible North-South asymmetry in the magnetic field of the Sun. This asymmetry seems to cause a bending of the heliospheric current sheet of the order of 10 degree in the southward direction, and it appears to be a recurrent characteristic of the Sun during the minimum of solar activity.

In this chapter we discuss the North-South asymmetry as inferred from

measurements of the deflection of polar coronal hole jets when they propagate throughout the corona. Since the corona is an environment with a plasma- $\beta$  less than 1, magnetic pressure is greater than kinetic one and this means that magnetic fields control the dynamics of plasma. Jets during their propagation trace the presence of magnetic field lines, as water is constrained to follow the shape of a channel. We measured the position angle at 1 and 2  $R_{\odot}$  of the 79 jets of the catalogue A.1 and we found that propagation is not radial, in agreement with the deflection due to magnetic field lines and the overexpansion of the solar wind. Moreover, the entity of the deflection is different between jets from the North and the South pole. We found the jets are more deviated in the North than in the South, with an asymmetry which is consistent with that inferred from other datasets and instruments.

## 4.1 The magnetic field structure in the solar corona

The solar corona is an environment highly conditioned by the strength and the topology of magnetic fields. We can think the solar corona as an ambient formed by many flux tubes that are filled by hot plasma and trace the configuration of magnetic field lines, in the same way as the iron filings trace the field lines of a magnetic bar in laboratory experiments.

The corona is far away from being a quiet region but it evolves in time following the solar cycle. The observations of corona in EUV or X-ray wavelengths reveal the presence of bright (dense), coinciding with the presence of active regions, and dark (void) regions, usually named coronal hole. In the same way, white-light observations obtained from coronagraphs show the presence of ray-like features at high latitudes, and helmet streamers at middle equatorial latitudes (Fig. 1.1). Active regions and helmet streamers are regions characterized by closed magnetic field lines, instead EUV dark and ray-like features are associated with open magnetic field lines, in which plasma is able to escape and to diffuse out from the Sun, leading to the formation of fast solar wind. Considering these evidences, the solar magnetic field in the corona during the minimum can be approximated at the lowest order by a dipole field, whose magnetic field lines go out from one pole and enter in the opposite one, changing the direction after the solar maximum. A better and realistic models can be achieved if we consider other magnetic moments, (*i.e.*, quadrupole, esapole, etc.) for reproducing the shape of the solar corona from observations.

The knowledge of the solar magnetic field comes mainly from measurements of splitting lines due to the Zeeman effect. This property can be applied to the radiation coming from the photosphere, allowing to estimate the vector magnetic field, but there is not possibility to infer direct measurements of the magnetic field of the corona. There are some methods

## 4.2 Polar jet deflection measurements

that try to measure the coronal magnetic field directly (effects of the Faraday rotation, polarization of free-free emission, Hanle effect in H Lyman- $\alpha$ , Stokes polarimetry in infrared lines), but the uncertainties associated to the measurements are very large. One accepted method is to infer the magnetic field structure by extrapolation from photospheric magnetic field values using a potential or a force-free field model. In the next section we discuss and we will obtain the expression of the magnetic field components in spherical coordinates from a potential model.

## 4.2 Polar jet deflection measurements

We investigated the influence of the large scale coronal magnetic field on the motion of jets through the corona, starting from the catalogue of 79 polar jets in the Appendix A.1. We exploited data from EUVI and COR1 instruments of SECCHI package aboard the STEREO spacecraft. Our strategy consists to calculate the Position Angle (PA), *i.e.* the angular displacement from the North axis to the jet position in counter clockwise direction, at two given distance from the solar center:  $1 R_{\odot}$ , that corresponds with the solar limb, and  $2 R_{\odot}$ . Since EUVI images cover the full disk to  $1.4 R_{\odot}$ , they are performing for measuring PA at  $1 R_{\odot}$ , that in the most cases correspond with the position of the jet footpoint. COR1 images have a FOV within  $1.4\text{--}4 R_{\odot}$ , but varies due to the offset of the occulter with respect to the Sun center. In order to clearly identify the jet in COR1, we took PAs at  $2 R_{\odot}$ , just over the boundary of the occulter 4.1 from the Sun centre. We used data from STEREO A or B, according where the jet is better seen, and we reserved the calculation of the PA in 3D geometry for future work. The measurements of PAs from the COR1 are plotted in function of PAs

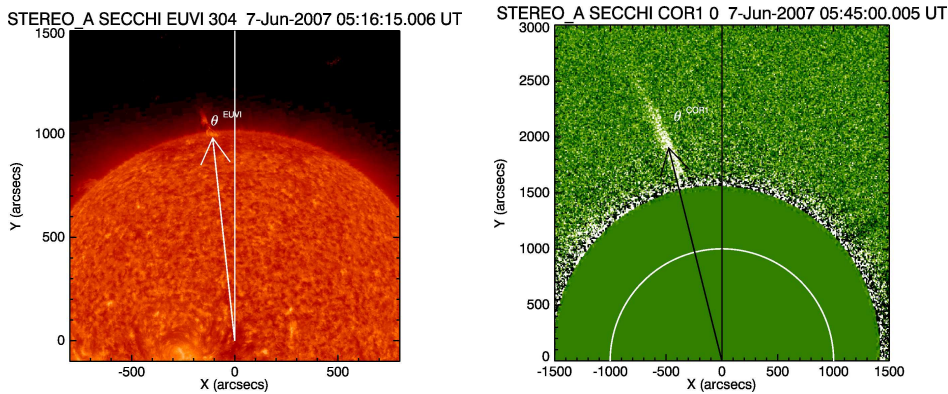


Figure 4.1: Image of the Sun at  $304 \text{ \AA}$  (left) from EUVI and coronagraphic image from COR1 in white light (right). We measured PAs (see the reference frame overlapped on the images) at  $1 R_{\odot}$  in the EUVI FOV and at  $2 R_{\odot}$  in the COR1 FOV.

from EUVI in Fig. 4.2 for the North pole (left) and the South one (right). Data points, represented by void triangles, are fitted by a linear function

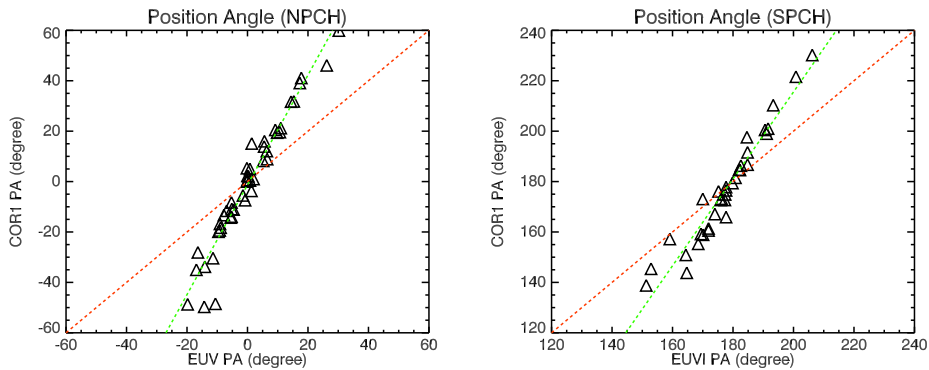


Figure 4.2: Plots of the EUV position angles vs the COR1 position angles for jets occurring at the North polar coronal hole (left) and jets occurring at the South one (right). The red dashed line represents equal position angles between the EUVI and COR1 FOV; the green dashed line fits the data points. Events rooted significantly away from the poles in EUV seem to have a large deviation in COR1 FOV, indicating that the jet motion could be following the diverging magnetic field lines.

(green dashed line) respectively for the North and South pole, according the equation:

$$\theta^{COR1} = k + m\theta^{EUVI} \quad (4.1)$$

where  $\theta$  is the PA for EUVI and COR1,  $k$  is the constant term of the linear fit and  $m$  is the slope of the line. The red line is an hypothetical line if the jets showed the same PAs at 1 and 2  $R_{\odot}$ . Although some scatter of the data points is present, an overall trend is evident: jets having small PAs (if in the NPCH) or small displacements from the south polar axis (if in the SPCH) in EUVI FOV show a small deviation in the COR1 FOV (they are near or on the red line, representing events that have same PA in both instruments); jets having larger PAs (if in the NPCH) or large displacement from the south polar axis (if in the SPCH) in the EUVI FOV (they occur at lower latitudes) show greater deviation in COR1 on average. The trajectory of the jets is not simply radial but bends towards the equator (see the green dashed line that clearly is far from the red one): we can suppose that jets appear to propagate along the magnetic field lines, which are almost radial near the solar dipole axis, while field lines deviate from the radial direction because of the dipolar structure at lower latitudes. This is also consistent with the over expansion towards low latitudes of the fast solar wind in polar coronal holes (*e.g.*, Fisk, 1996). The non-radial outward propagation of the jets is also a feature noted in other coronal structure: *e.g.*, coronal streamers

## 4.2 Polar jet deflection measurements

and polar plumes extend non radially (Wang, 1996), as well as non-radial seems to be the propagation of CMEs, as found in earlier studies (*e.g.*, Cremades & Bothmer, 2004; Patsourakos *et al.*, 2010).

The somewhat larger number of events in the north coronal hole is due to the orbital features of STEREO, which allow a better view of the northern region in the investigated time period (Nisticò *et al.*, 2009). It can be seen that when going from the EUVI to COR1 position angle, the changes in PA are larger in the North coronal hole than in the South one. More precisely, linear fits of data point for the North and the South give the following values of the parameter  $k$  and  $m$ , that are summarized in the Table 4.1. If we carefully look the slope  $m$ , we find that it is greater in the North

Pole	$k$ (degrees)	$m$
North	$-1.28 \pm 0.97$	$2.17 \pm 0.09$
South	$-129.20 \pm 15.44$	$1.72 \pm 0.09$

Table 4.1: Values of the parameters coming from the fits of the jet EUVI and COR1 position angles respectively for the North and the South pole.

than in the South, giving an indication that jets are more deviated from their origins. This is evident also in Fig. 4.2, where we plotted the quantity  $(\theta^{COR1} - \theta^{EUVI})/\theta^{EUVI}$  as function of time expressed in Carrington rotation numbers for North polar jets (black void triangles) and South polar jets (red void squares). We can infer that there is not a particular dependence of the position angle displacement from EUVI to COR1 FOV in time, and this variation is larger in the North pole than in the South one.

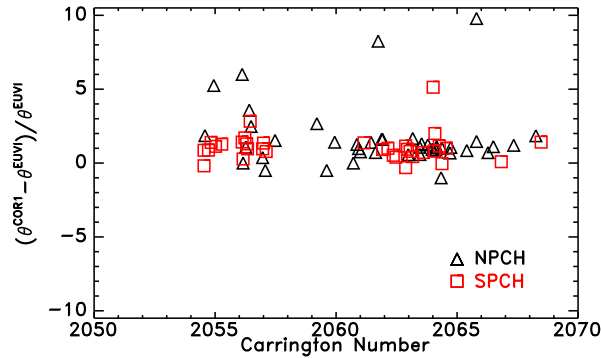


Figure 4.3: Angular displacement normalized to the EUVI PA in function of time, expressed in Carrington rotation number, for jets occurred in the North (black void triangles) and in the South (red void squares).

The evidence that jets are more deflected in one pole than in the opposite one, could be associated with the different inclination of the open magnetic field lines: in our case, jets occurring in the North, are more deviated from their origin since the magnetic field lines are more bent than in the South, and, of consequence, the radial magnetic field intensity is greater in the South pole. By analogy, we can think of the magnetic field lines of a dipole, produced for example by a magnetic bar: close to poles, field lines are almost straight since they are directed along the dipole, while if we move further, magnetic field lines are inclined to distance.

### 4.3 North-South asymmetry

From the results shown in the last section, a natural question arises: “Is the different deflection of jets, in the North and in the South pole, an indication of North-South asymmetry?”. The N-S asymmetry is object of discussion inside the scientific community, and of scientific investigation. Until nowadays, N-S asymmetry constitutes an unsolved problem, and the causes why this asymmetry exists are not well understood.

There are several experimental evidences of North-South asymmetry in literature. First evidences come from direct measurements of the photospheric magnetic field thanks to magnetographs, which were extrapolated to the source surface by [Hoeksema \(1995\)](#), who showed that magnetic field strength in the North cap is less than in the South one.

The Space mission Ulysses provided new insights about N-S asymmetry: thanks to its special orbit, perpendicular to ecliptic plane, it allowed to explore high latitudes regions of the heliosphere, and during its passage close to the Sun, at about 1 AU, gave us measurements of the interplanetary magnetic field ([Erdős & Balogh, 1998](#)) and particle data. Indeed, an indication of N-S asymmetry comes from latitudinal gradients of energetic particle fluxes ([Simpson \*et al.\*, 1996](#); [Heber \*et al.\*, 1996a,b](#)). Moreover, [Erdős & Balogh \(2010\)](#) studied magnetic field data of Ulysses during the fast latitude scans, showing that the radial component of the magnetic field at the source surface is greater in the South pole, and calculating the offset of the heliospheric current sheet of the order of 3–5 degrees (see also, [Virtanen & Mursula, 2010](#)). Their results are summarized in the Table 4.2.

	$B_S$ (nT)	$B_N$ (nT)	$B_S/B_N$	Offset (degree)
Cycle 22	3.41	3.05	1.12	3.249
Cycle 23	2.61	2.16	1.21	5.459

Table 4.2: Radial component of the magnetic field from Ulysses. Adapted from [Erdős & Balogh \(2010\)](#).

### 4.3 North-South asymmetry

---

The possible idea for explaining the N-S asymmetry is to consider the global magnetic field as the sum of several multipole components, and ascribe the mismatch between North and South to the contribution of the quadrupole moment (see Fig. 4.4), as suggested by [Bravo & Gonzales-Esparza \(2000\)](#); [Mursula & Hiltula \(2005\)](#). Indeed, Fig. 4.4 suggested us as this asymmetry could be due: if we look the direction of magnetic field lines for the dipole (left) and the quadrupole (right) at different solar minima (top: cycle 21; bottom: cycle 22), we note that they are opposite in the North pole, and concordant in the South one. This means that the northern magnetic field is weakened, while the southern field is more enhanced, causing the evident asymmetry and the shift of the heliospheric current sheet in the southward direction of some degrees. In the following sections we try to calculate how much is the influence of the quadrupole moment and to give an estimate of the corresponding southward shift of the heliospheric current sheet, starting from the deflection of polar jets.

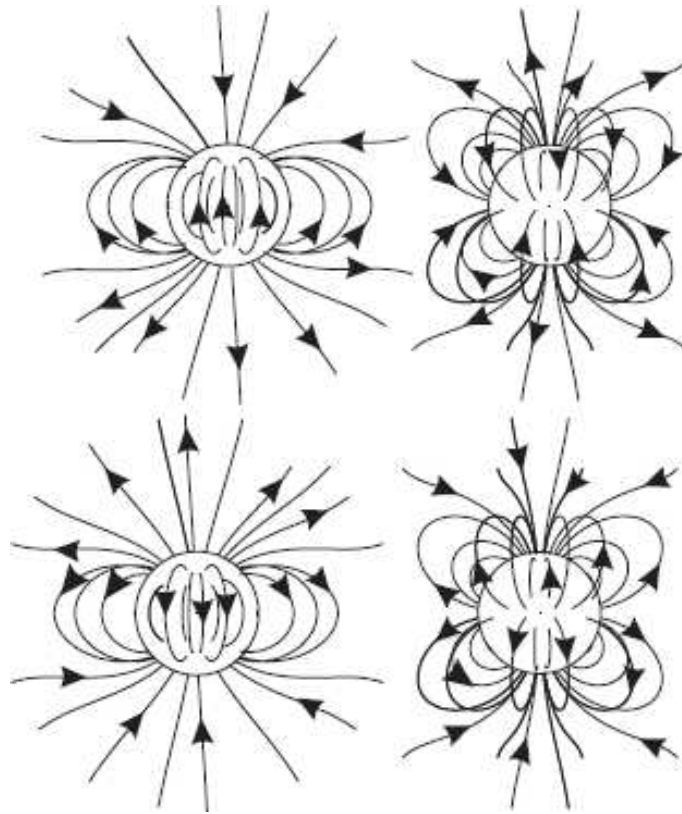


Figure 4.4: Sketches of the configuration of magnetic field lines for the dipole (left) and quadrupole (right) moment, for the minimum of cycle 21 (top) and cycle 22 (bottom). Adapted from [Bravo & Gonzales-Esparza \(2000\)](#).



#### 4.4 A model for the coronal magnetic field

Direct measurements of the solar magnetic field can be obtained only at the photosphere. Coronal magnetic field data are still hard to obtain and, for the moment, only extrapolations from photospheric data are made. There are several extrapolation methods for obtaining a magnetic configuration of the solar corona (for details see, [Altschuler & Newkirk, 1969](#); [Aschwanden, 2006](#), chapter 5). A first one was introduced by Gauss over 150 years ago (see, [Kivelson & Russel, 1995](#)), showing that the magnetic field on Earth could be described as the gradient of a scalar potential:

$$\mathbf{B} = -\nabla\Phi = -\nabla(\Phi^i + \Phi^e), \quad (4.2)$$

where  $\Phi^i$  is the magnetic scalar potential due to currents inside the Earth,  $\Phi^e$  is the scalar potential to due external sources. In a similar way, coronal magnetic field can be expressed as a potential field  $\mathbf{B}(\mathbf{r})$ , coming from the gradient of a scalar potential function  $\Phi$ , if we assume the current-free approximation.

The scalar potential function can be expressed in spherical coordinates as an expansion in terms of the Legendre polynomials  $P_l^m(\cos\theta)$ :

$$\Phi(r, \theta, \phi) = R_\odot \sum_{l=1}^N \sum_{m=0}^l f_l(r) P_l^m(\cos\theta) (g_l^m \cos(m\phi) + h_l^m \sin(m\phi)), \quad (4.3)$$

with

$$f_l(r) = \frac{\left(\frac{r_w}{r}\right)^{l+1} - \left(\frac{r_w}{r}\right)^l}{\left(\frac{r_w}{R_\odot}\right)^{l+1} - \left(\frac{r_w}{R_\odot}\right)^l}, \quad (4.4)$$

where  $f_l(r)$  is a function that defines the position of the solar source surface at  $r_w$  solar radii, after that the magnetic field lines are purely radial, reproducing the configuration of the magnetic field in the solar wind.

The components of the magnetic field can be found as the derivative of the scalar potential  $\Phi$ :

$$\begin{aligned} B_r(r, \theta, \phi) &= -\frac{\partial\Phi}{\partial r}, \\ &= -R_\odot \sum_{l=1}^N \sum_{m=0}^l \frac{\partial}{\partial r} f_l(r) P_l^m(\cos\theta) (g_l^m \cos(m\phi) + h_l^m \sin(m\phi)), \end{aligned} \quad (4.5)$$

$$\begin{aligned} B_\theta(r, \theta, \phi) &= -\frac{1}{r} \frac{\partial\Phi}{\partial\theta}, \\ &= -\frac{R_\odot}{r} \sum_{l=1}^N \sum_{m=0}^l f_l(r) \frac{\partial}{\partial\theta} P_l^m(\cos\theta) (g_l^m \cos(m\phi) + h_l^m \sin(m\phi)), \end{aligned} \quad (4.6)$$

$$\begin{aligned}
 B_\phi(r, \theta, \phi) &= -\frac{1}{r \sin \theta} \frac{\partial \Phi}{\partial \phi}, \\
 &= \frac{R_\odot}{r \sin \theta} \sum_{l=1}^N \sum_{m=0}^l f_l(r) P_l^m(\cos \theta) (g_l^m \sin(m\phi) + h_l^m \cos(m\phi)).
 \end{aligned} \tag{4.7}$$

We can further simplify the expressions of the magnetic field components, if we assume axial symmetry: the component  $B_\phi$  is null. This condition is obtained for  $m = 0$ ; and so, the magnetic field components become as:

$$B_r(r, \theta) = -R_\odot \sum_{l=1}^N \frac{\partial}{\partial r} f_l(r) P_l^0(\cos \theta) (g_l^0), \tag{4.8}$$

$$B_\theta(r, \theta) = -\frac{R_\odot}{r} \sum_{l=1}^N f_l(r) \frac{\partial}{\partial \theta} P_l^0(\cos \theta) (g_l^0), \tag{4.9}$$

$$B_\phi = 0. \tag{4.10}$$

The expansion depends only from the index  $l$ . If we truncate the series at  $l = 3$ , we have three contributions that give the dipole ( $l = 1$ ), the quadrupole ( $l = 2$ ), and the esapole (at  $l = 3$ ) term, with the corresponding moments (or harmonic coefficients)  $g_1^0, g_2^0, g_3^0$ . The contribution of the monopole ( $l = 0$ ) is not taken under consideration, since it is physically unacceptable.

Making some calculations, we find the magnetic field components of the dipole:

$$B_r^{(1)}(r, \theta) = \left(\frac{R_\odot}{r}\right)^3 \left(\frac{2r_w^3 - r^3}{r_w^3 - R_\odot^3}\right) g_1^0 \cos \theta, \tag{4.11}$$

$$B_\theta^{(1)}(r, \theta) = \left(\frac{R_\odot}{r}\right)^3 \left(\frac{r_w^3 - r^3}{r_w^3 - R_\odot^3}\right) g_1^0 \sin \theta; \tag{4.12}$$

the components of the quadrupole:

$$B_r^{(2)}(r, \theta) = \frac{1}{2} \left(\frac{R_\odot}{r}\right)^4 \left(\frac{3r_w^5 - 2r^5}{r_w^5 - R_\odot^5}\right) g_2^0 (3 \cos^2 \theta - 1), \tag{4.13}$$

$$B_\theta^{(2)}(r, \theta) = 3 \left(\frac{R_\odot}{r}\right)^4 \left(\frac{r_w^5 - r^5}{r_w^5 - R_\odot^5}\right) g_2^0 \cos \theta \sin \theta; \tag{4.14}$$

and the components of the esapole:

$$B_r^{(3)}(r, \theta) = \frac{1}{2} \left(\frac{R_\odot}{r}\right)^5 \left(\frac{4r_w^7 - 3r^7}{r_w^7 - R_\odot^7}\right) g_3^0 (5 \cos^3 \theta - 3 \cos \theta), \tag{4.15}$$

$$B_\theta^{(3)}(r, \theta) = \frac{1}{2} \left(\frac{R_\odot}{r}\right)^5 \left(\frac{r_w^7 - r^7}{r_w^7 - R_\odot^7}\right) g_3^0 (15 \cos^2 \theta \sin \theta - 3 \sin \theta); \tag{4.16}$$

In the limit of  $r_w \rightarrow \infty$ , we have the classical expressions for the dipole, the quadrupole, and the esapole.

$$B_r^{(1)}(r, \theta) = 2 \left( \frac{R_\odot}{r} \right)^3 g_1^0 \cos \theta, \quad (4.17)$$

$$B_\theta^{(1)}(r, \theta) = \left( \frac{R_\odot}{r} \right)^3 g_1^0 \sin \theta, \quad (4.18)$$

$$B_r^{(2)}(r, \theta) = \frac{3}{2} \left( \frac{R_\odot}{r} \right)^4 g_2^0 (3 \cos^2 \theta - 1), \quad (4.19)$$

$$B_\theta^{(2)}(r, \theta) = 3 \left( \frac{R_\odot}{r} \right)^4 g_2^0 \cos \theta \sin \theta, \quad (4.20)$$

$$B_r^{(3)}(r, \theta) = 2 \left( \frac{R_\odot}{r} \right)^5 g_3^0 (5 \cos^3 \theta - 3 \cos \theta), \quad (4.21)$$

$$B_\theta^{(3)}(r, \theta) = \frac{1}{2} \left( \frac{R_\odot}{r} \right)^5 g_3^0 (15 \cos^2 \theta \sin \theta - 3 \sin \theta). \quad (4.22)$$

The complete magnetic field can be written as the sum of the dipole, quadrupole, and esapole contributions:

$$B_r(r, \theta) = B_r^{(1)} + B_r^{(2)} + B_r^{(3)}, \quad (4.23)$$

$$B_\theta(r, \theta) = B_\theta^{(1)} + B_\theta^{(2)} + B_\theta^{(3)}. \quad (4.24)$$

It is useful to calculate the expressions for the potential vector  $\mathbf{A}$ . Since  $\mathbf{B} = \nabla \times \mathbf{A}$  and  $\mathbf{B} = (B_r, B_\theta, 0)$ , the vector  $\mathbf{A}$  will have the component  $A_\phi \neq 0$ . By components, we have:

$$B_r(r, \theta) = \frac{1}{r \sin \theta} \frac{\partial}{\partial \theta} (\sin \theta A_\phi(r, \theta)), \quad (4.25)$$

$$B_\theta(r, \theta) = -\frac{1}{r} \frac{\partial}{\partial r} (r A_\phi(r, \theta)). \quad (4.26)$$

Making the appropriate integrals, we obtain  $A_\phi = A_\phi^{(1)} + A_\phi^{(2)} + A_\phi^{(3)}$ , where

$$A_\phi^{(1)}(r, \theta) = \frac{1}{2} \left( \frac{R_\odot^3}{r^2} \right) \frac{2r_w^3 + r^3}{r_w^3 - R_\odot^3} g_1^0 \sin \theta, \quad (4.27)$$

$$A_\phi^{(2)}(r, \theta) = \frac{1}{2} \left( \frac{R_\odot^4}{r^3} \right) \frac{3r_w^5 + 2r^5}{r_w^5 - R_\odot^5} g_2^0 \cos \theta \sin \theta, \quad (4.28)$$

$$A_\phi^{(3)}(r, \theta) = \frac{1}{24} \left( \frac{R_\odot^5}{r^4} \right) \frac{4r_w^7 + 3r^7}{r_w^7 - R_\odot^7} g_3^0 (15 \cos^2 \theta \sin \theta - 3 \sin \theta). \quad (4.29)$$

#### 4.4 A model for the coronal magnetic field

Using the cylindrical coordinates  $(\rho, \phi, z)$ , with  $r^2 = \rho^2 + z^2$ , we find the quantity  $\rho A_\phi(r, \theta) = \rho A_\phi^{(1)}(r, \theta) + \rho A_\phi^{(2)}(r, \theta) + \rho A_\phi^{(3)}(r, \theta)$ , where

$$\rho A_\phi^{(1)}(r, \theta) = \frac{1}{2} \left( \frac{R_\odot}{r} \right)^3 \left( \frac{2r_w^3 + r^3}{r_w^3 - R_\odot^3} \right) g_1^0 \rho^2, \quad (4.30)$$

$$\rho A_\phi^{(2)}(r, \theta) = \frac{1}{2} \left( \frac{R_\odot}{r} \right)^4 \left( \frac{3r_w^5 + 2r^5}{r_w^5 - R_\odot^5} \right) g_2^0 \frac{\rho^2 z}{r}, \quad (4.31)$$

$$\rho A_\phi^{(3)}(r, \theta) = \frac{1}{24} \left( \frac{R_\odot}{r} \right)^5 \left( \frac{4r_w^7 + 3r^7}{r_w^7 - R_\odot^7} \right) g_3^0 \frac{15\rho^2 z^2 - 3r^2 \rho^2}{r^2}. \quad (4.32)$$

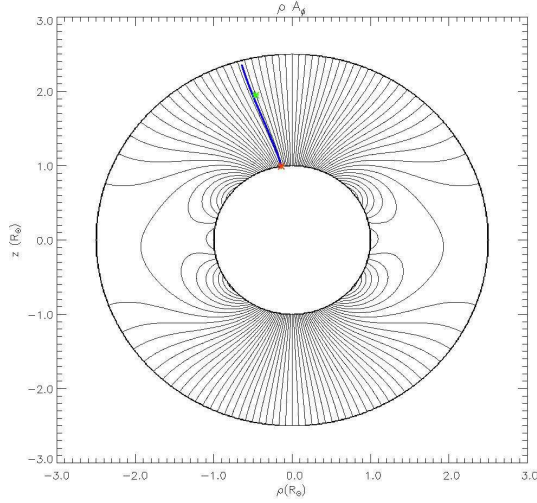


Figure 4.5: Magnetic field lines obtained as a contour levels of the magnetic flux function  $\Phi(\mathbf{B})$ . The blue curve is a magnetic field line obtained by integration with a Runge-Kutta scheme of the 4th order of the curvilinear equations, the red symbol is the position of the jet measured in the EUVI FOV, and the green one is the corresponding position at  $2 R_\odot$ , as measured in the COR1 FOV.

The magnetic flux function is equal to  $\Phi(\mathbf{B}) = 2\pi\rho A_\phi$  in cylindrical coordinates. We can plot the magnetic field lines as contour levels of the flux  $\Phi(\mathbf{B})$ . An example is shown in Fig. 4.5, where the coronal magnetic field structure is given between 1 and  $2.5 R_\odot$ . We considered as typical values of harmonic coefficients  $g_1^0 = 24.642$ ,  $g_2^0 = -1.065$ ,  $g_3^0 = 27.156$ , as given by the Wilcox Solar Observatory for the Carrington rotation number 2062, in classical approximation. The red and green asterisks are, respectively, the jet position at  $1 R_\odot$ , as measured in the EUVI FOV, and  $2 R_\odot$ , as measured in the COR1 FOV. The blue line is the magnetic field line, obtained by

integrating, with a Runge-Kutta scheme of the 4th order, the two first order differential equations:

$$\begin{cases} \frac{dr}{ds} = \frac{B_r}{B}, \\ \frac{d\theta}{ds} = \frac{B_\theta}{rB}. \end{cases} \quad (4.33)$$

where  $s$  is the distance along the field line. The integration is made starting from the PA at  $1 R_\odot$ ; we can note that the magnetic field lines moves near the measured position of the jet at  $2 R_\odot$ .

## 4.5 Calculation of the magnetic moments

Given the model for the coronal magnetic field, we search which values for the magnetic moments  $g_1^0$ ,  $g_2^0$ ,  $g_3^0$ , are suitable for describing the jet deflections. These coefficients are usually calculated from magnetograms data, provided and published by the Wilcox Solar Observatory (visit the website <http://wso.stanford.edu/>). For inferring values of these coefficients from magnetograms, two kind of hypothesis are assumed according the inner boundary conditions in the photosphere (Wang & Shelley, 1992). Indeed, from magnetographs we can measure the line-of-sight (LOS) component of the photospheric field at a given latitude  $\alpha$  on the solar disk. A “classical” model takes in consideration the projection of the LOS photospheric field along the radial and latitudinal component ( $B_r = B_{LOS} \cos \alpha$ ,  $B_\theta = B_{LOS} \sin \alpha$ ); a “radial” model if the photospheric field is thought totally radial in the photosphere ( $B_r = B_{LOS}$ ,  $B_\theta = 0$ ). Since the magnetic field is non potential and nearly radial at the photosphere (Wang & Shelley, 1992), a better approach is to consider the radial model. According the literature, this give better results and extrapolations in corona more appropriate. A correction is usually applied to the classical model: since it cannot describe more appropriately the polar magnetic field, a field of  $11.5 \cos^8 \theta G$  is added, where  $\theta$  is the colatitude.

The top figures (Fig. 4.6) show the temporal evolution of the coefficients for the “classical” and the “radial” model, as calculated by the Wilcox Solar Observatory. The bottom plots are the ratio between  $g_2^0/g_1^0$  and  $g_3^0/g_1^0$ . The region bounded by the dashed lines is the temporal window in which our jets are observed.

We can look that harmonic coefficients evolve in time, and the harmonic coefficient for the quadrupole is less in magnitude than the other ones and change in time showing, especially in the radial approximation, an indication of periodicity. Then the dipole and esapole moment show the same sign. We try to calculate these coefficients in a different way and to compare them with those obtained from the Wilcox, and find the associated coronal field structure and the position of the heliospheric current sheet on the solar surface.

## 4.6 Comparison model vs observations: results and discussion

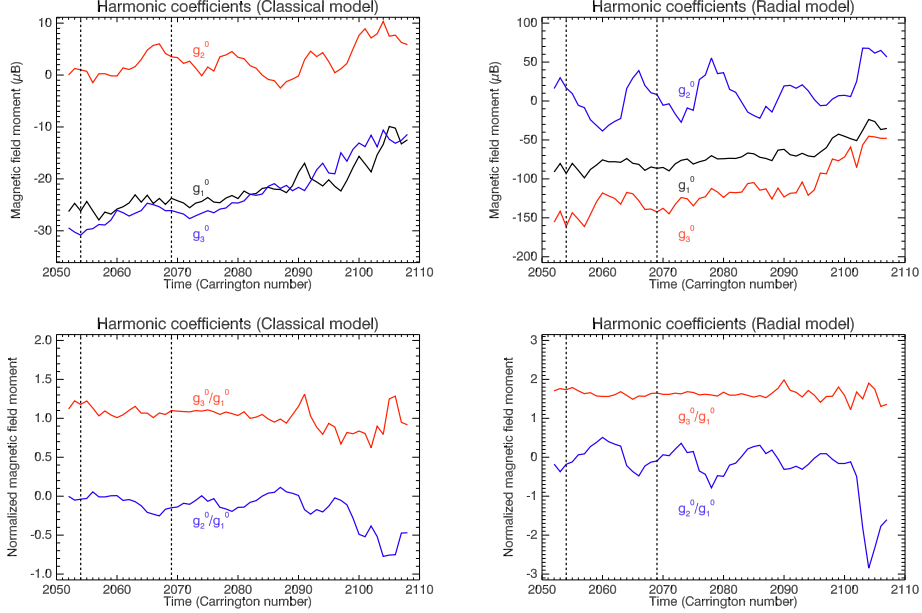


Figure 4.6: Time evolution of the harmonic coefficients  $g_1^0, g_2^0, g_3^0$ , as calculated by the Wilcox Solar Observatory.

## 4.6 Comparison model vs observations: results and discussion

Now we try to estimate the best coefficients that fit our jet observations. For several values of  $g_2^0$  and  $g_3^0$  coefficients, relative to the dipole moment (that is imposed equal to 1), we integrate the magnetic field lines with a program written in Fortran90 from the basis of the jets, as measured in the EUVI FOV, until  $2 R_\odot$ . Then we calculate the standard deviation  $\sigma(g_2^0, g_3^0)$ , taking into account the final position angle from the numerical integration  $\theta^{COR1(Sim)}$  and that one as measured in the COR1 FOV  $\theta^{COR1(Obs)}$ , as:

$$\sigma(g_2^0, g_3^0) = \sqrt{\frac{\sum_{n=1}^N (\theta_n^{COR1(Sim)}(g_2^0, g_3^0) - \theta_n^{COR1(Obs)})^2}{N - 1}}, \quad (4.34)$$

with  $N$ , the total number of jets. The coefficient  $g_2^0$  spans from  $-3$  to  $3$ , and  $g_3^0$  from  $0$  to  $3$ . We created some maps representing the variation of the standard deviations for different cases, classical and radial model (Fig. 4.7), and for different distances of the source solar surface, as found in literature:  $2.5$  and  $3.25 R_\odot$ .

The first row are maps obtained for the classical (left) and radial (right) model considering the source solar surface at  $2.5 R_\odot$  (top); the second ones at  $3.25 R_\odot$  (bottom). The purpose of these maps is to give us an indication

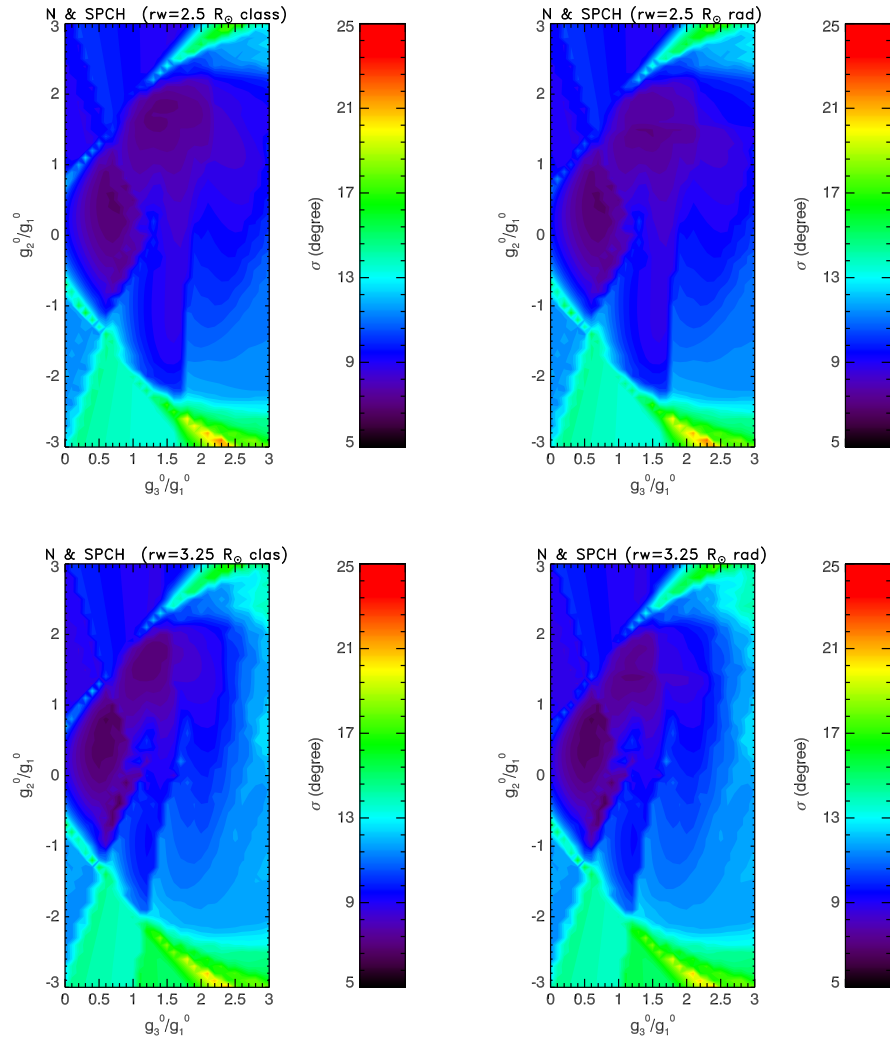


Figure 4.7: Standard deviation maps for different values of the  $r_w$  (top:  $2.5 R_\odot$ , bottom:  $3.25 R_\odot$ ) parameter for the classical (left) and radial (right) model.

#### 4.6 Comparison model vs observations: results and discussion

which values of  $g_2^0/g_1^0$  and  $g_3^0/g_1^0$  minimize the standard deviation (dark regions in the maps), and better fit the deflections of jets. It is possible to note that there is not a large difference in standard deviation maps between the classical and the radial model, and also considering the different distances of the source surface. We obtain several possible values of  $g_2^0$  and  $g_3^0$  that minimize the standard deviation: a minimum is found for  $g_2^0/g_1^0 = -0.4$  and  $g_3^0/g_1^0 = 0.8$ , by standard deviation maps with the source surface at  $3.25 R_\odot$ . These estimates are much reliable: indeed, the quadrupole moment is negative and assume a value that is very close to those tabulated by the Wilcox Solar Observatory; instead, the esapole moment is smaller. We can infer the structure of the coronal magnetic field. This is shown in Fig. 4.8: the heliospheric current sheet is coned southward, forming an angle of about 7.45 deg, which is not so different from some other estimates found in the literature.

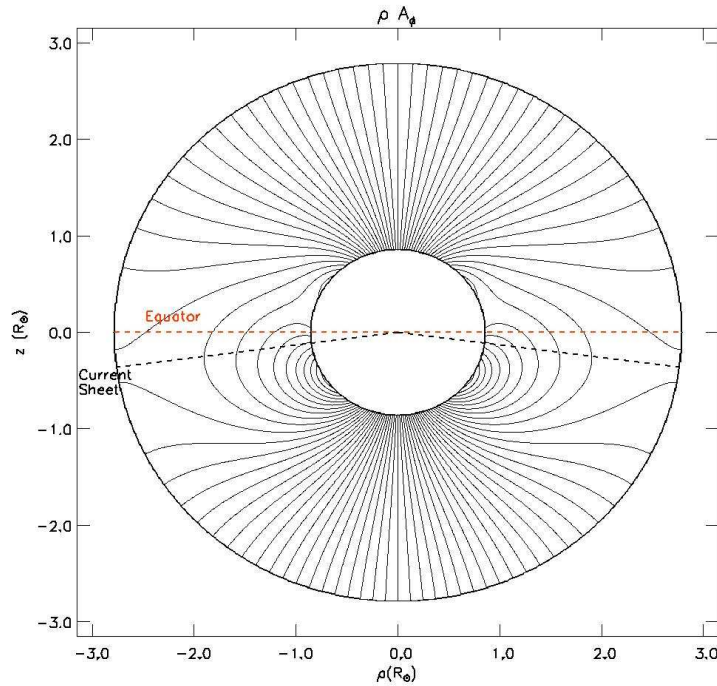


Figure 4.8: Structure of the coronal magnetic field lines with  $g_2^0/g_1^0 = -0.4$  and  $g_3^0/g_1^0 = 0.8$ , and the corresponding heliospheric current sheet position projected on the source surface at  $3.25 R_\odot$ .



## 4.7 Summary

We used polar corona jets as a probe for understanding the magnetic field structure of the solar corona. We assumed that jets, because the corona is an environment with a plasma- $\beta$  parameter less than 1, propagate along open magnetic field lines. We measured the PA of jets at  $1 R_{\odot}$  in the EUVI FOV, and at  $2 R_{\odot}$  in the COR1 FOV, and analysed the deflection of jets. We found that jets are deflected toward low latitudes, in agreement with assumption the magnetic field lines are bent toward the equator, and this deflection is more pronounced in the North Pole than in the South one. This North-South asymmetry has also found in other datasets, starting from photospheric magnetic field measurements (Hoeksema, 1995), latitudinal gradient in solar energetic particles (Simpson *et al.*, 1996; Heber *et al.*, 1996a,b), and also from magnetic field measurements in the interplanetary medium by the Ulysses spacecraft (Erdős & Balogh, 2010). This asymmetry can be explained in terms of multipole components of the global magnetic field (Bravo & Gonzales-Esparza, 2000; Mursula & Hiltula, 2005): the quadrupole moment tends to affect the total magnetic field weakening it in the North pole and enhancing it in the South one. We tried to estimate the contribution of the quadrupole moment, starting from jet PA data, and compare with other results. We expressed the coronal magnetic field as the sum of the dipole, quadrupole, and esapole moments, starting from the expression of a scalar potential function  $\Phi$  in terms of spherical harmonic expansion. We traced magnetic field lines from the footpoint of jets (at  $1 R_{\odot}$ ) until  $2 R_{\odot}$  for different values of the magnetic moments with a Runge-kutta scheme of the 4th order. We considered more realistic values for the harmonics coefficients  $g_2^0$  and  $g_3^0$ , that ones which minimize the standard deviation of position angles coming from the numerical simulation and the observation. We obtained as reliable values  $g_2^0 = -0.4g_1^0$  and  $g_3^0 = 0.8g_1^0$ . From these estimates, we were able to give a structure of the magnetic field lines (Fig. 4.8) in which the heliospheric current sheet shows an offset of 7.45 degrees, a value close to that coming from other works (Mursula & Hiltula, 2005; Erdős & Balogh, 2010). Therefore, we have an independent indication that the solar magnetic field can indeed exhibit a North-South asymmetry, a result that can have profound implications on the models of solar dynamo.

## Chapter 5

# Three dimensional structure of CMEs: observations and modeling comparison

This chapter is devoted to study the three dimensional shape of coronal mass ejections (CMEs) and to compare the CME modeling results with observations from the STEREO mission. We give a brief introduction to CMEs, explaining some basic properties and their possible origins. Then, we discuss the so-called *croissant* model introduced by [Thernisien \*et al.\* \(2009\)](#), used for explaining the different shape of CME observations. From a catalogue of almost 500 CMEs, compiled by Eckhard Bosman at the University of Göttingen, occurred during the years 2007-2010, we tried to compare the modeling results of almost one hundred of the best visible CMEs with the observations of their source regions, in order to test the validity of the model. This study has been made during a period of research of six months during the Ph.D., at the University of Göttingen, in Germany, with the supervision of the dr. Volker Bothmer and in collaboration with his Ph.D. student Eckhard Bosman, whose research activity is framed in the EUropean Seventh Framework Programme (EU 7 FP) project SOTERIA (SOLar TERrestrial Investigations and Archives).

### 5.1 Coronal Mass Ejections: a brief introduction

Since the corona can be observed from Earth only during solar eclipses for a few minutes, daily coronagraph observations performed with space missions in the early 1970s, as the *Orbiting Solar Observatory 7* (OSO7) and Skylab (Gosling 1974), allowed to discover huge emissions of plasma from the corona. These large bubbles of plasma were termed “*Coronal Mass Ejections*”, and in literature they are indicated with the acronym of CMEs. With the starting of the SoHO mission in 1995, they are object of a

deep scientific investigation thanks to coronagraph observations performed by the *Large Angle Spectrometer and Coronagraph Observatory* (LASCO) instruments, which observed more than one thousand CMEs during almost 10 years of activity. This large number of CMEs detected by the LASCO instruments is organized in a list, available on-line at the following address: <http://cdaw.gsfc.nasa.gov/CME/list>.

Their size is usually greater than the solar radius, increasing as they move far away from the Sun, and the mass carried out is estimated to be of the order of  $10^{12}$  kg, about a tenth of the total coronal mass. CMEs lift off from the Sun at speeds of the order of several hundred  $\text{km s}^{-1}$  and propagate in the interplanetary medium. The typical speed measured is 300–500  $\text{km s}^{-1}$ , but literature documents some events with a speed of 2000  $\text{km s}^{-1}$ . Because of their high velocity, they could lead to the formation of shock in front of their leading edge, and accelerate particles at high energies. Moreover, since they transport magnetic fields, rushing from the inner corona of the Sun, they can magnetically interact with the magnetosphere of planets, if they encounter them, creating sudden disturbances and leading to the formation of the so-called *geo-magnetic storms*. In this sense, we can say the CMEs are the main causes that determine the conditions of the *space-weather*.

From statistical analysis, it is known that CME frequency is influenced by the 11-cycle of the solar activity, and numerous studies were done about their relationship with other coronal phenomena, like flares or prominences. Another important issue is their association with global waves, propagating on the solar disk.

## 5.2 2D or 3D shape?

White-light coronagraphic images give us some pretty images of CMEs that erupt and leave the Sun. Most of the CMEs, that are detected by coronagraphs, typically show a three-part structure, as can be seen in Fig. 5.1. The first part is a bright rim that marks the position of the leading front of the CME; it is followed by a dark void region, characterized by low density plasma, and finally a bright trailing core, associated with prominence material (first and second snapshot of Fig. 5.1 from left). Not all the CMEs show this morphology: if the CME is directed toward Earth, a circular expanding front is seen around the occulter that hides the solar disk (third snapshot of Fig. 5.1 from left). In other cases, we can observe events which do not show any particular shape, characterized only by the presence of the leading edge, or in other cases events that exhibit a twisted shape.

Understanding the real shape of a CME is a crucial aspect that cannot be solved by a single point of observation: CME features are projected on the plane, overlap and to disentangle them is a hard work. In first studies,

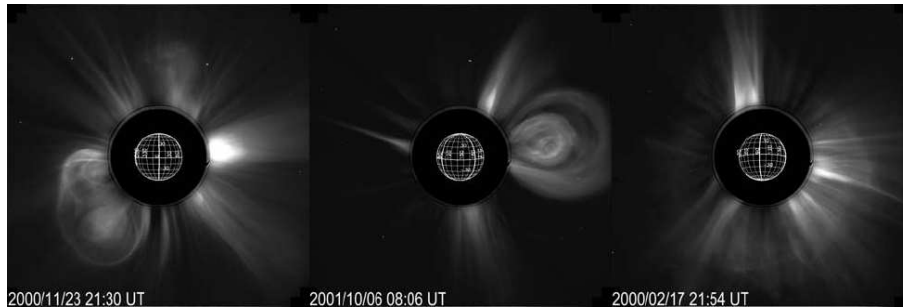


Figure 5.1: Typical CMEs (the first two from left) that clearly reveal the three part structure. The third CME is an halo event (adapted from [Cremades & Bothmer, 2004](#)).

it was proposed that CMEs are mostly developed in two dimensions and not three ([Trotter & McQueen, 1980](#)): because of their association with erupting prominences, a loop planar geometry was thought to be suitable for CME morphology. Even if today the three dimensional shape is accepted in literature, it is still unclear what kind of 3D geometrical shape can be associated.

An improvement in the CME observations comes from the STEREO mission, which was designed for solving this issue: the observatories, STEREO A and B, allow to take images from two different perspectives and combine them in a three-dimensional view ([Howard & Tappin, 2008](#)). Different models can be taken into account for reconstructing the 3D shape of CMEs: in the next section we will present the forward modeling technique by [Thernisien \*et al.\* \(2009\)](#)

### 5.3 Forward Modeling technique of flux rope CMEs

From detailed studies performed on CMEs detected by LASCO instruments (see, [Cremades & Bothmer, 2004](#)), many CMEs present a three part structure, as described in the last section. The dark cavity region, between the outer front and the core of the CME, can be interpreted as a magnetic flux rope ([Cremades & Bothmer, 2004](#)). The existence of large scale expanding flux ropes is validated by the presence of faint striations in white-light images; from satellite observations of magnetic clouds in the solar wind, associated with disappearing filaments on the solar disk ([Bothmer & Schwenn, 1998](#)). It is also evident from [Cremades & Bothmer \(2004\)](#) that CMEs are originating from loop/flux rope systems that already exist in the low corona and expand in a self-similar manner. [Cremades & Bothmer \(2004\)](#) found that bipolar regions in the photosphere are generally the underlying source

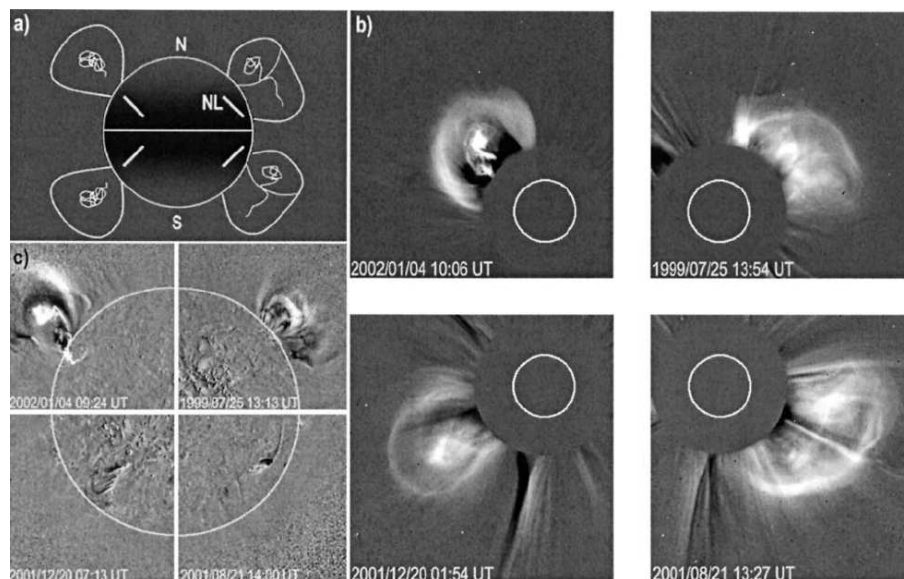


Figure 5.2: The empirical scheme for classify the shape of CMEs according the position of the source region on the photosphere (adapted from [Cremades & Bothmer, 2004](#)).

regions of CMEs. At higher latitudes they are associated with prominences. From these consideration, an empirical scheme for limb events was inferred for defining the CME shape, starting from the heliographic position and orientation of the associated source region neutral line (Fig. 5.2). According to the Hale’s law, the neutral line of bipolar region is usually bent toward the solar equator: when it is positioned on the solar disk near the East limb, the associated CME is viewed face on, with its axis directed along the line-of-sight (LOS); instead, when the neutral line is near the West limb, the CME is seen edge-on, with its axis perpendicular to the LOS (see Fig. 5.2: first figure top-left).

Starting from this empirical scheme, [Thernisien et al. \(2006, 2009\)](#) developed a forward-modeling technique for flux-rope CMEs, called *Graduated Cylindrical Shell* (GCS) model (Fig. 5.3). The model consists of a tubular section of radius  $a$ , forming the main body, which is attached to two cones of height  $h$ , representing the legs of the CME. The two legs are separated of an angle  $2\alpha$  and they are connected at the centre of the Sun  $O$ , and tilted of an angle  $\gamma$ . This model is also popular as the *croissant model*. For obtaining synthetic images, an electron density profile is assigned on the shell according to the expression:

$$N_e(d) = N_e \exp \left[ - \left( \frac{d - a}{\sigma_s} \right)^2 \right], \sigma_s = \{ \sigma_{\text{trailing}}, d < a; \sigma_{\text{leading}}, d > a \},$$

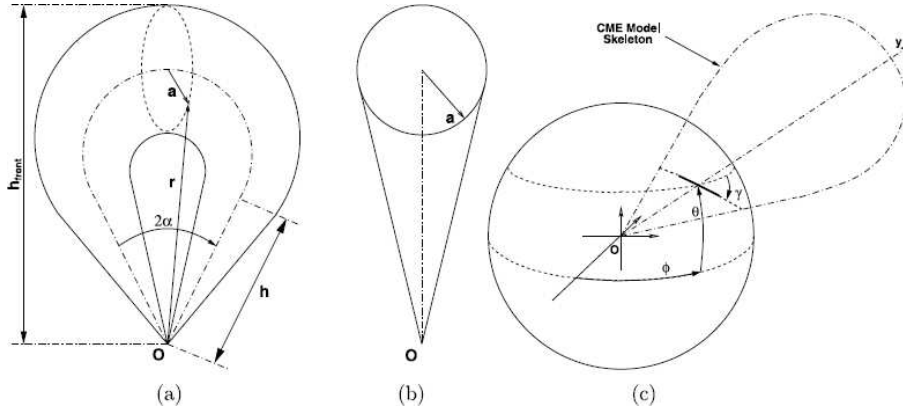


Figure 5.3: The Graduated Cylindrical Shell model for flux-rope CMEs .Courtesy [Thernisien \*et al.\* \(2009\)](#).

The model is implemented by a *Ray-tracing* code, that simulates the Thomson scattering of the photospheric light by the electrons of the corona and produces coronagraphic synthetic images. The software is written in C++ and can be run via IDL command lines (the software is distributed by the SSW package). It also gives as output the position of the apex of the modeled CME, *i.e.* the position of the leading edge projected on the solar disk, the positions of the intersection between the two legs of the *croissant* and the solar surface, the angles  $\alpha$  and  $\gamma$ , as defined before.

## 5.4 Source Region Identification

From a catalogue of almost one hundred CMEs, that show flux rope features, compiled by Eckhard Bosman at the University of Göttingen, using SECCHI/COR2 data, we searched the corresponding source regions on the solar disk ([Bosman \*et al.\*, 2011](#)). We inspected solar movies from STEREO/EUVI data and looked mostly at 195 and 304 Å (images are available at the address [http://cdaw.gsfc.nasa.gov/stereo/daily\\_movies](http://cdaw.gsfc.nasa.gov/stereo/daily_movies)). For easily identifying source regions (SRs) of CMEs, we looked for EUVI events happening in a temporal window before and close to the time appearance of CMEs in COR2, and that have a position in agreement with the position angle of CMEs measured in COR2. We were able to identified 76 source regions events.

After we have identified the SRs, we extracted the Carrington coordinates of the Source regions from EUVI images. We followed this procedure:

- we downloaded EUVI data in FITS (Flexible Image Transport System) format, which is the common format for astrophysical data, from the

website <ftp://stereoftp.nascom.nasa.gov/pub/> ;

- FITS files were processed with the `secchi_prep` routine of the SSW package, which gives as output the header, that contains several information of the file data, and the image array;
- we used the routine `fitshead2wcs.pro`, which interprets the World Coordinates System (WCS) information in the FITS header;
- finally, for obtaining the Carrington coordinates of the SR that has pixel coordinates  $(x, y)$ , we used the routine `wcs_jet_coord.pro`.

All these steps are implemented in IDL scripts, in order to get coordinates in an easy way starting from the visual inspection of the SR by EUVI images.

In the next session, we give the comparison between the positions of the SR coming from observations, and the positions of CMEs coming from the CGS model.

## 5.5 Observations vs modeling: some results

We compared the position of the SR, as obtained by observations in the EUVI FOV, and the position of the apex and the legs as obtained from modeling (Bosman *et al.*, 2011). We chose to plot the positions, from observations and modeling, on a SoHO/MDI (Michelson Doppler Imager) synoptic charts, for associating the SR with the underlying photospheric magnetic field.

In Fig. 5.4, we show two examples of MDI synoptic charts in which we marked the positions of the source regions (white colours) and the apex and legs positions (green colours) for the CMEs n° 111, 113, and 179 of the CME catalogue by Eckhard Bosman. We can note that in the first synoptic charts, there is a good agreement between the modeling results and the observations, especially for the event n° 111. The source regions of the CME are cospatial with the two active regions, and a wave is seen in the EUVI FOV at 195 Å, propagating while the CME lifts off. For the event n° 179 (bottom), there is a good agreement in longitude but an off-set in latitude. In this case, the CME is associated with the eruption of a prominence.

For better understanding the association with CMEs and corresponding source regions in the low corona, we show an event in Fig. 5.5 (top). Images from COR1 and EUVI at 195 and 304 Å are presented for the CME n° 111. It occurred on 25th March, 2008, and it clearly appears at the East limb in STEREO-B/COR1. It is evident also in A, although partially hidden by the helmet streamer. It show the typical three-part structure: a bright circular front the moves away from Sun, the dark void and the core, just above the East limb. In the low corona the source region of the CME is located in an active region where a flare occurred and trigger the expansion of the CME

## 5.5 Observations vs modeling: some results

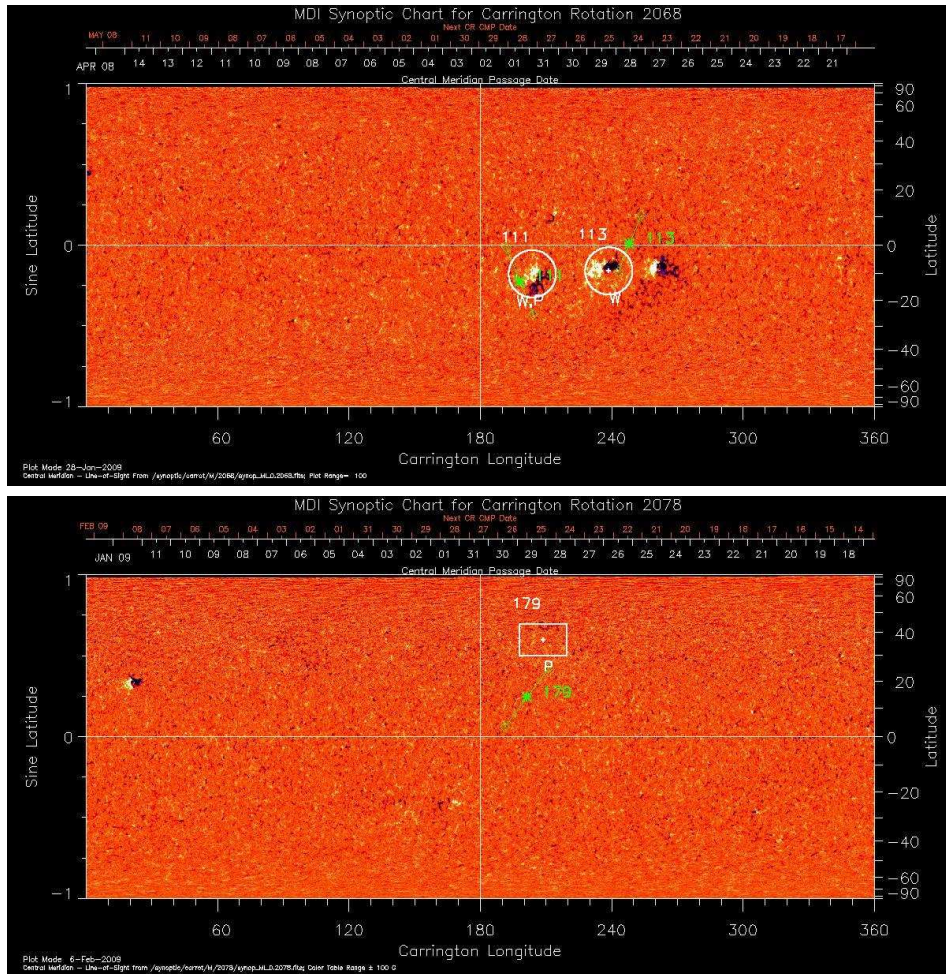


Figure 5.4: MDI synoptic charts for number Carrington 2068 (top) and 2078 (bottom). The positions of the source region from observation is in white: it is surrounded by a circle when a wave (W) is noted, and by a rectangular when the CME is caused by the eruption of a prominence. Positions from modeling are in green: the central point is the apex and the two sided points are the positions of the legs on the solar disk.



and the propagation of a wave in the low corona at 195 Å (Fig. 5.6), and the lift-off of chromospheric plasma is also seen at 304 Å (Fig. 5.5, bottom).

In order to understand how the model fits the shape of CMEs, we took into account the coordinates of the apex for every analysed CME, and the corresponding coordinates of the source region, as inferred from EUVI. We separately analysed the Carrington longitude and latitude of source region and apex for all CMEs. We considered  $\Delta_{lon} = lon_{obs} - lon_{mod}$  and  $\Delta_{lat} = lat_{obs} - lat_{mod}$ . In Fig. 5.7 we show histogram plots of longitude difference (left) and latitude difference (right) between observational data and model results, and fitted the distributions with a Gaussian. The fit give a Gaussian distribution centered near 0 for the longitude ( $\langle \Delta_{lon} = 0.51 \text{ deg} \rangle$ ), while the latitude distribution is centered at ( $\langle \Delta_{lat} = 17.18 \text{ deg} \rangle$ ). The width of the distributions is large ( $\sigma_{\Delta_{lon}} = 25.50 \text{ deg}$  and  $\sigma_{\Delta_{lat}} = 25.07 \text{ deg}$ ), suggesting that most events have a not perfect matching between observations and model, but about the 30% of the total modeled events are in good agreement with the observations.

On the other hand, a latitudinal and longitudinal off-set can be justified, since CMEs probably do not propagate radially from their source regions, but they can deviate somewhat, as found for jets, too. Cremades & Bothmer (2004) found that CMEs are inclined to shift from their source regions to low latitudes of about 20 degrees. This could explain also the peak in the histogram distribution in latitude at about +30 degrees. Moreover, the deviation could be influenced by the different ways how the CME expansion is triggered: impulsive CMEs from flares events are fast, and so they could be affected less by the surrounding coronal environment than CMEs from prominences, since they erupts slowly, with times of the order of several hours and they could be conditioned by the global magnetic field of the Sun.

The propagation of CMEs from the inner to the outer corona seems to show a similarity with the propagation of jets, as discussed in Chapter 4. Both events are subject to a deviation from their source, and the jet deflection was charged to the overall structure of the magnetic field in the solar corona. Are CMEs deviated because of the influence of the global magnetic field of the solar corona and are they reflecting the N-S asymmetry, too? The analysis undertaken in this section show that there is a discrepancy between the position of the SR as observed in EUVI images and that one obtained as a result of the model of the flux rope CMEs. Moreover, we found  $lat_{obs} > lat_{mod}$  in most of the events ( $\sim 80 \%$ ), giving us an indication of a deviation always directed towards low latitudes. This evidence could reflect the structure of the magnetic field lines (*e.g.*, see Fig. 4.8), which are generally bent toward lower latitudes. Furthermore, the peak of the distribution in Fig. 5.7 (left) for the latitudinal difference ( $\Delta_{lat}^{peak} = lat_{obs} - lat_{mod} \approx 30 \text{ deg}$ ), seems to suggest an eventual N-S asymmetry, showing

## 5.5 Observations vs modeling: some results

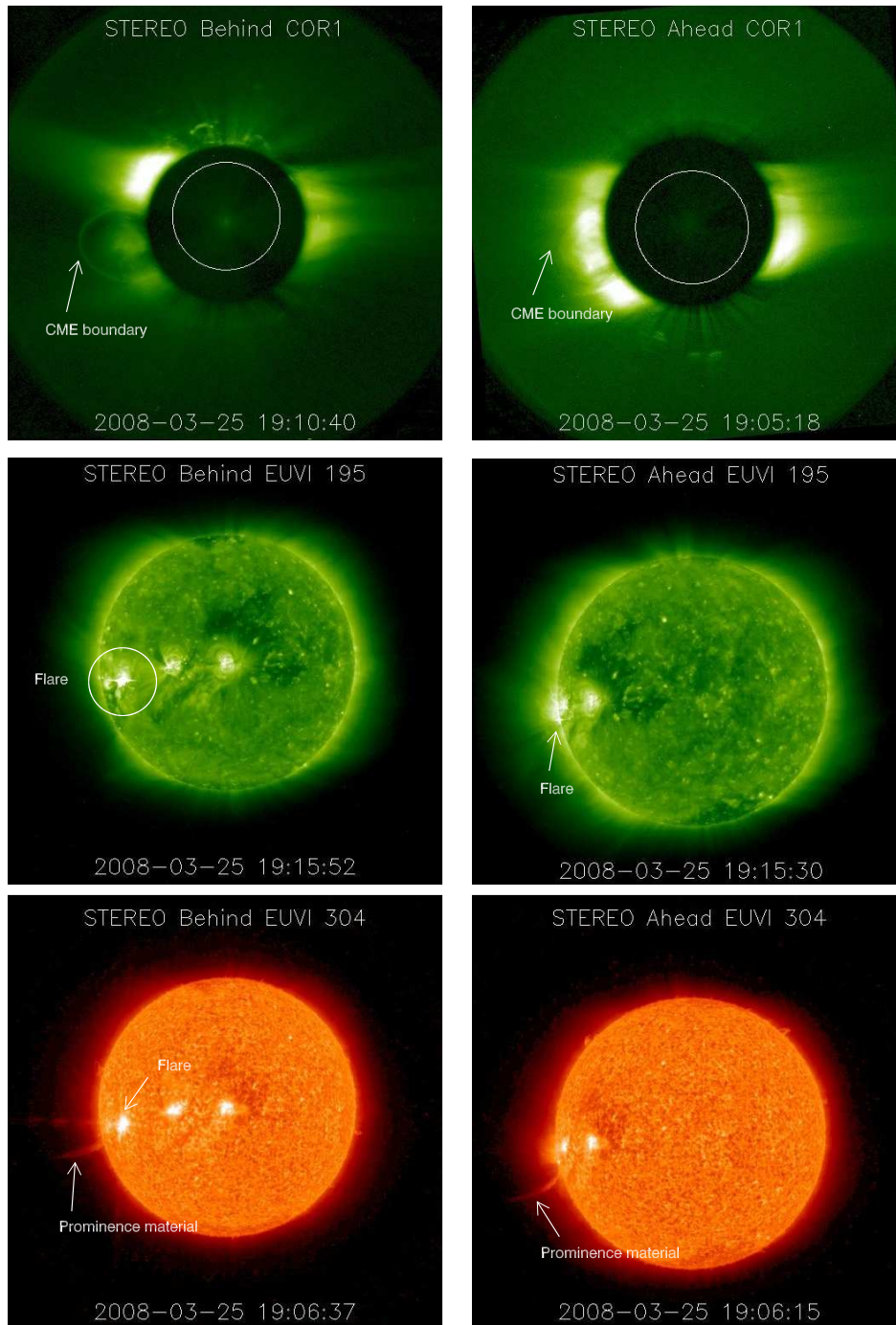


Figure 5.5: CME occurred on 25 March, 2008 (n° 111). Top: COR1 images from STEREO B (left) and A (right). The bubble CME is clearly noted on the East limb. Middle: 195 EUVI images showing the flare near the East limb in B, which is associated with the CME. Bottom: 304 images from STEREO. Note the chromospheric material elongating in the space, following the ascending of the CME. Courtesy of SECCHI consortium.

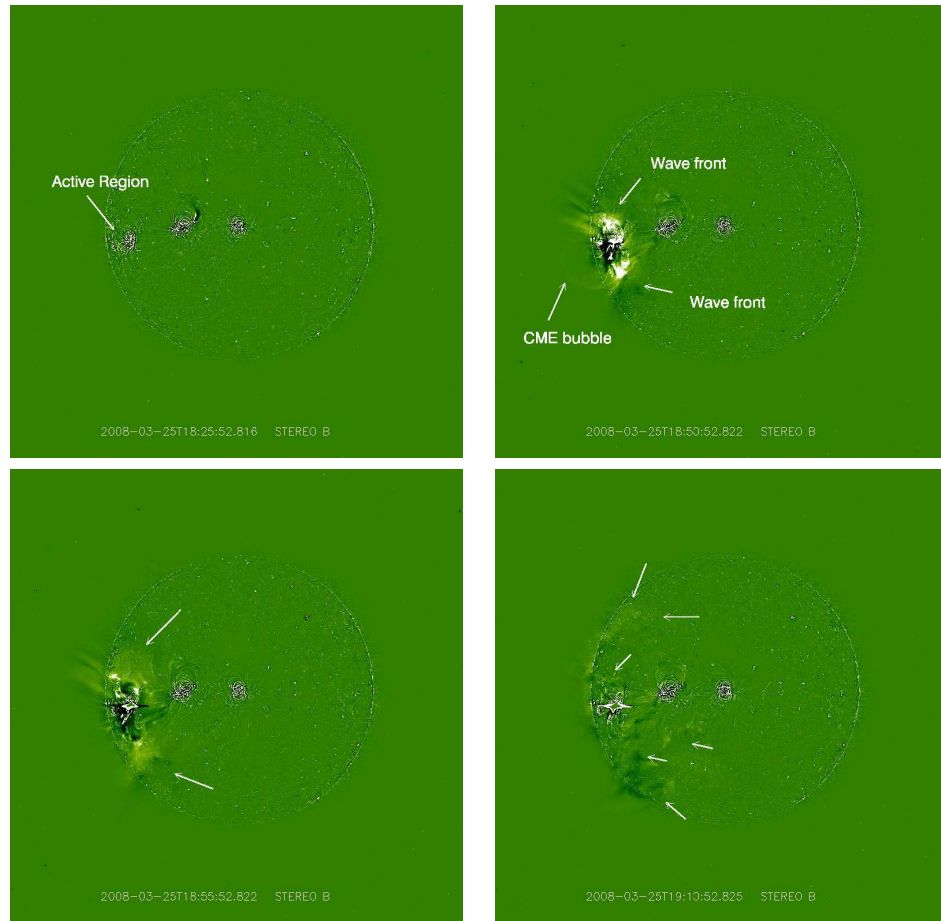


Figure 5.6: Smoothed STEREO/SECCHI images of the event occurred on 25 March, 2008, at  $195 \text{ \AA}$  (see also Fig. 5.5). In the first frame an active region, near the east solar limb, is the site of a flare, which trigger the expansion of the CME, whose bubble appears in the second frame, and the propagation of a wave from the flare site. Wave fronts are indicated by the white arrows in the third and fourth frame.

that CMEs are more deviated in the northern hemisphere, as found also for jets (Chapter 4, see Fig. 4.1). By the way, this cannot be fully proved since the most of the analysed events occurred in the North hemisphere ( $\sim 80\%$ ) than in the South ( $\sim 20\%$ ). More analysis will be undertaken in the future for assessing better the validity of the model and understanding the CME deflection in relationship with the coronal structure.

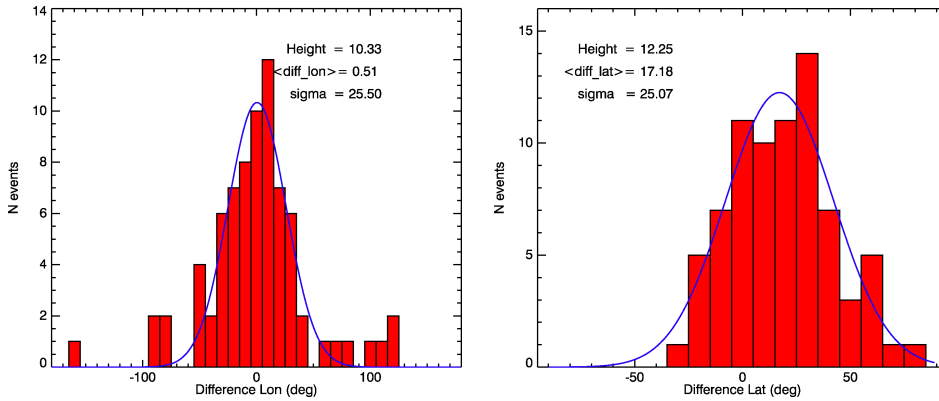


Figure 5.7: Carrington longitude (left) and latitude (right) difference distribution between the observed positions of the source region and the apex positions of CMEs from the CGS modeling. We note that there is a good agreement for the longitude ( $\Delta_{lon}^{peak} \approx 0$  deg), while the latitude difference is centered at  $\Delta_{lat}^{peak} \approx 30$  deg, giving us an idea of a possible non radial propagation of CMEs, which probably move toward low latitude during their expansion because of the supposed influence of the coronal magnetic field structure.

## 5.6 Summary

In this chapter we presented a study of the 3D structure of CMEs performed by analysing data from the STEREO observatories, from a catalogue of flux rope CMEs identified in SECCHI/COR2 by Eckhard Bosman, at the University of Göttingen (Bosman *et al.*, 2011), and analysed by the forward modeling technique from Thernisien *et al.* (2006). We identified the associated source regions, in order to make a comparison between observations and modeling results and to test the goodness of the model.

We found that there is a good agreement between observations and modeling for about the 30% of all 76 CMEs events. The other events shows an offset in latitude and longitude, which is ascribed to a global deviation of the CME during its expansion, from its source regions in the low corona to  $10 R_{\odot}$ , where it appears in COR2 FOV, since the model does not take in consideration a possible deflection of CMEs. The latitude off-set is con-

sistent with that measured by [Cremades & Bothmer \(2004\)](#), and could be also explained by an effect of the fast solar wind from corona holes, which deviates CMEs toward low latitudes, encompassing the CME expansion at higher latitudes, or by a direct influence of the coronal magnetic field structure on the CMEs, whose lines constrain CMEs to propagate toward lower latitudes, following magnetic field lines, as found for polar jets, too.

## Chapter 6

# Heating heavy ions in the polar corona by collisionless shocks: a one-dimensional simulation

Spectroscopic analysis of emission lines from the solar corona, in the 1940s, made by Bengt Edlén, allowed to assert that the corona has a temperature of the order of million Kelvin degrees. This evidence was totally unexpected and surprising, since the photosphere has a temperature of about 6,000 K and it is closer to the Sun centre than the corona. Also SoHO/UVCS spectroscopic measurements show that heavy ions like  $O^{5+}$ ,  $Mg^{9+}$ , and  $Ca^{2+}$  are heated more than protons in the polar solar corona. The common sense suggests that heat cannot flow from a cooler body to a warmer one. Also SoHO/UVCS spectroscopic measurements show that heavy ions like  $O^{5+}$ ,  $Mg^{9+}$ , and  $Ca^{2+}$  are heated more than protons in the polar solar corona. And so, the question still unsolved is: “Why the corona is so much hotter? What are the physical reasons?”

A model for explaining the observations of preferential heating of heavy ions in the polar solar corona was proposed ([Zimbardo, 2010, 2011](#)). In that model the ion energization mechanism is the ion reflection off supercritical quasi-perpendicular collisionless shocks in the corona and the subsequent acceleration by the motional electric field  $\mathbf{E} = -\mathbf{V} \times \mathbf{B}/c$ . The mechanism of heavy ion reflection is based on ion gyration in the magnetic overshoot of the shock. The acceleration due to the motional electric field is perpendicular to the magnetic field, giving rise to large temperature anisotropy with  $T_{\perp} \gg T_{\parallel}$ , in agreement with SoHO observations. In this chapter, we try to validate the test of such a model by means of a one dimensional test particle simulation where ions are launched toward electric and magnetic profiles representing the shock transition. We study the dynamics of  $O^{5+}$ , as representative of

coronal heavy ions for Alfvénic Mach numbers of 2–4, as appropriate to solar corona. It is found that  $O^{5+}$  ions are easily reflected and gain more than mass proportional energy with respect to protons.

## 6.1 Introduction to the coronal heating problem

The observations of the solar corona raise a fundamental question: “What is the source of energy and the heating mechanism able to rise temperature to these values?”. In solar coronal plasma, a natural source can be found in the magnetic reconnection processes. The energy stored in the magnetic field is thought to be released by means of magnetic reconnection as heat, acceleration of particles, and fast plasma flows, the so-called reconnection outflow jets, and shocks can be formed in the reconnection jet. Observational evidence of magnetic reconnection is given by small scale plasma jets (Nisticò *et al.*, 2009, 2010), which could be associated with fast shocks (Yokoyama & Shibata, 1996; Tsuneta & Naito, 1998). Shock waves are considered to be common in the corona and in the chromosphere/transition region (*e.g.*, Yokoyama & Shibata (1995, 1996); Ryutova *et al.* (2008)). Further, recent X-ray Hinode and UV STEREO observations have shown that many more plasma jets are present in the polar corona than previously thought (Cirtain *et al.*, 2007; Patsourakos *et al.*, 2008). Higher in the corona large scale shocks are associated with the emergence of coronal mass ejections and with flaring phenomena (Mancuso *et al.*, 2002; Bemporad & Mancuso, 2010).

Recently Zimbardo (2009, 2010) proposed a model where the heavy ion energization mechanism is, essentially, the ion reflection off supercritical quasi-perpendicular collisionless shocks in the corona and the subsequent acceleration by the motional electric field  $\mathbf{E} = -\mathbf{V} \times \mathbf{B}/c$ . Energization by shock waves is customarily considered in solar corona physics in connection with the observations of X-rays flares and radio burst (*e.g.*, Tsuneta & Naito, 1998; Aurass and Mann, 2004). In those cases, first order Fermi acceleration (Tsuneta & Naito, 1998) or second order Fermi acceleration (Petrosian & Liu, 2004; Perri *et al.*, 2009) are invoked to explain the observations of high energy particles which are related to the X-ray emission. Fermi acceleration requires many repeated interactions with the shock (or the magnetic clouds). On the other hand, here we are interested in the energy gain which ions undergo during a single shock encounter, and which affects the majority of the ions (the thermal plasma), not only the high energy tails. This is the case, for instance, of the coronal heating observed by Mancuso *et al.* (2002) after the passage of a CME-driven shock.

In the low  $\beta$  corona, a shock wave is formed when a superAlfvénic plasma flow having velocity  $V_1 > V_A$  collides with the ambient coronal plasma. Here,

the plasma  $\beta$  is given by  $\beta = 8\pi p/B^2$ , where  $p$  is the gas kinetic pressure,  $B$  is the magnetic field magnitude,  $V_1$  is the plasma velocity upstream of the shock, and  $V_A = B/\sqrt{4\pi\rho}$  is the Alfvén velocity, with  $\rho$  the mass density. The Alfvénic Mach number is defined as the ratio between the upstream plasma velocity and the Alfvén speed,  $M_A = V_1/V_A$ . Considering that a shock wave modifies the plasma state in an irreversible way, we define the upstream region as the unperturbed region where the plasma flow is supersonic and superAlfvénic, and the downstream region as the behind shock medium where a heated, perturbed plasma is found.

It is well known both from laboratory (Paul *et al.*, 1965; Phillips & Robson, 1972) and from spacecraft experiments (Sckopke *et al.*, 1983; Gosling & Robson, 1985; Scudder *et al.*, 1986; Bale, 2005) that when  $M_A$  is larger than a critical Mach number  $M_A^*$ , a fraction of ions is reflected off the shock, leading to the so-called supercritical shocks. Ion reflection is related to the inability of a laminar shock to dissipate the plasma flow energy by resistivity alone, and ion reflection sets in approximately when the downstream thermal speed equals the downstream flow speed  $V_2$  (*e.g.*, Leroy *et al.*, 1982). The critical Mach number  $M_A^*$  varies from 1.5 to 2.7, depending on the upstream plasma  $\beta$  and the shock normal angle  $\theta_{Bn}$  (Edmiston & Kennel, 1984). When the angle  $\theta_{Bn}$  between the shock normal (pointing in the upstream direction) and the upstream magnetic field is larger than about  $45^\circ$ , the reflected ions reenter the shock after gyrating in the upstream magnetic field. Such shocks are termed quasi-perpendicular. Conversely, for  $\theta_{Bn} < 45^\circ$ , the reflected ions propagate upstream, forming the ion foreshock which characterizes the quasi-parallel shocks.

Ion reflection can be considered to be the main mechanism by which collisionless shocks convert the flow directed energy into heat, while the electrons are heated much less (Gosling & Robson, 1985; Veltri & Zimbardo, 1993a,b).

The acceleration due to  $\mathbf{E}$  is perpendicular to the magnetic field, giving rise to large temperature anisotropy with  $T_\perp \gg T_\parallel$ , in agreement with SoHO observations. This is a typical effect of collisionless shocks, and is also obtained with the model of Lee & Wu (2000), which mostly considers subcritical shocks. On the other hand, in the model of Zimbardo (2010, 2011), heavy ion heating is easily found to be more than mass proportional with respect to protons, because the heavy ion orbit is mostly upstream of the quasi perpendicular shock foot (Zimbardo, 2009, 2010, 2011). In such a case, the heavy ions gyrate in the upstream magnetic field, which is weaker than the foot magnetic field and so have a larger non adiabatic displacement in the direction of the electric field, boosting the heavy ion energization. In particular, Zimbardo (2011) has shown that a for protons a 30 fold energy increase can be obtained in a single shock encounter with



$M_A \simeq 7$ , while for heavy ions the energy increase can be larger and the ratio of temperatures, for an exactly perpendicular shock, can be expressed as  $T_{heavy}/T_p \sim (1.5 - 2) \times (m_{heavy}/m_p)$ .

In order to check this model, we develop here a test-particle code to study the ion dynamics in the presence of a model shock profile. The shock is described by a stationary, one dimensional profile of magnetic and electric fields. The magnetic field has a transverse component ( $B_z$ ) which exhibits the well know foot-ramp-overshoot-undershoot structure, while the electric field corresponding to the cross shock electric potential which slows down the ions (*e.g.*, Phillips & Robson, 1972). Both hydrogen and oxygen  $O^{5+}$  ions are injected upstream of the shock with a random thermal velocity plus the bulk velocity  $V_1$ . Many particles are injected, and typical trajectories are shown, together with the velocity and energy distribution functions. Early results are presented, which show that heavy ions are reflected due to the combined effects of the shocks magnetic foot, the electric potential jump, and the magnetic overshoot. The  $O^{5+}$  reflection rate appears to be large enough to give an important contribution to heavy ion preferential heating, and a more than mass proportional energy gain is found.

## 6.2 The numerical model

As a first model, we consider an exactly perpendicular supercritical collisionless shock, and we assume a simple one dimensional stationary shock structure. We note that the structure of quasi-perpendicular collisionless shocks in neither steady nor onedimensional. Both PIC numerical studies (*e.g.*, Quest, 1986; Lembége and Savoini, 1992; Yang *et al.*, 2009) and data analysis (Lobzin *et al.*, 2007) show that quasi-perpendicular shocks exhibit strong variability of the “average” fields on the scale of the proton gyroperiod, with a shock reformation cycle which also involves the ion reflection process. However, here we are interest mostly in the heavy ion reflection process, so that, following Gedalin (1996), we neglect the time variability of the shock structure.

The upstream quantities are indicated by the subscript 1, and the downstream quantities by the subscript 2. We adopt the Normal Incidence Frame (NIF) of reference, in which the shock is at rest, the upstream plasma velocity is along the  $x$  axis and perpendicular to the shock surface,  $\mathbf{V}_1 = (V_{x1}, 0, 0)$ , the upstream magnetic field lays along the  $z$  axis,  $\mathbf{B}_1 = (0, 0, B_{z1})$ , so that the motional electric field  $\mathbf{E} = -\mathbf{V} \times \mathbf{B}/c$  is in the  $y$  direction,  $E_y = V_{x1}B_{z1}/c$ . For quasi-perpendicular supercritical shocks, the magnetic field profile is characterized by the foot-ramp-overshoot-undershoot sequence (*e.g.*, Phillips & Robson, 1972; Leroy *et*

## 6.2 The numerical model

---

*al.*, 1982; Gosling & Robson, 1985). Throughout the shock layer, these are modeled by the components of the steady state electric and magnetic fields which are defined in the following way:  $B_x = 0, B_y = 0$ , and:

$$B_z(x) = B_1 + (B_2 - B_1) \left[ \frac{1 + \tanh(x/\lambda)}{2} \right] + \text{over}(x) + \text{foot}(x), \quad (6.1)$$

with

$$\text{over}(x) = \begin{cases} B_{\text{over}} \exp \left[ \frac{-x^2}{2\Delta^2} \right] & x \leq 0, \\ B_{\text{over}} \exp \left[ \frac{-x^2}{2(5\Delta)^2} \right] & x > 0, \end{cases} \quad (6.2)$$

$$\text{foot}(x) = \frac{1}{2} (B_{\text{foot}} - B_1) \left[ \tanh \left( \frac{x+2}{2\lambda} \right) - \tanh \left( \frac{x}{\lambda} \right) \right], \quad (6.3)$$

which respectively define the overshoot and the foot of the magnetic field. We point out that the magnetic overshoot plays an important role in the magnetic reflection of ions (*e.g.*, see Gedalin, 1996; Zimbardo, 2011) that is, ion reflection is not due solely to the electric potential jump.  $B_1$  and  $B_2$  are the upstream and downstream magnetic field respectively, while the shock ramp is centered at  $x = 0$ . Above,  $\lambda$  represents the shock ramp thickness,  $B_{\text{over}}$  the overshoot height, and  $B_{\text{foot}}$  the magnetic foot height. The components of the electric field are modeled as:

$$E_x = -\frac{\xi}{2\sqrt{\pi}} \frac{v_u^2}{\Delta} (f_1 + f_2), \quad (6.4)$$

with

$$f_1 = -\exp \left[ -\frac{x^2}{\Delta^2} \right], \quad (6.5)$$

$$f_2 = 2\alpha \frac{x - \frac{\Delta}{\sqrt{2}}}{\Delta^2} \exp \left[ -\frac{(x - \frac{\Delta}{\sqrt{2}})^2}{\Delta^2} \right]. \quad (6.6)$$

The  $x$  component of the electric field corresponds to the cross shock electric potential which develops self-consistently in collisionless shocks, and which has an important role in the ion slowing down and reflection. The parameter  $\xi$  above describes the magnitude of the electrostatic potential barrier in terms of the upstream kinetic energy in dimensionless units. The electric field  $E_x$  in the region of the shock ramp is directed toward upstream, thus slowing down the ions, while beyond the ramp  $E_x$  is directed downstream, in agreement with the findings of hybrid numerical simulations (*e.g.*, Leroy *et al.*, 1982). On the other hand Particle In Cell (PIC) numerical simulations have shown that a substantial part of the cross shock potential occurs already in the foot region (Burgess *et al.*, 1989; Gedalin, 1996). For the present runs we use the electric field profile shown in Fig. 6.1, and reserve the use of a

broader electric potential barrier for future work. The  $y$  component of the electric field corresponds to the  $\mathbf{V} \times \mathbf{B}$  electric field, and is conserved across the shock layer:

$$E_y = \left[ -\frac{1}{c} \mathbf{V} \times \mathbf{B} \right]_y = \frac{V_{x1} B_{z1}}{c}, \quad E_z = 0. \quad (6.7)$$

We point out that the constancy of  $E_y$  breaks down in the more realistic

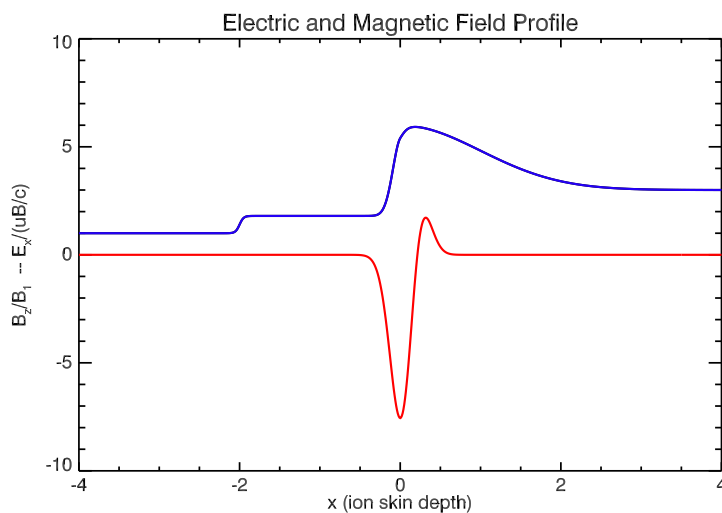


Figure 6.1: Profile along the  $x$  axis of the electric (red) and magnetic (blue) fields for the given values of the parameters:  $v_u = 2.5$ ;  $\Delta = 0.2$ ;  $\alpha = 0.1$ ;  $\xi = 0.6$ ;  $B_1 = 1.0$ ;  $B_2 = 3.0$ ;  $B_{foot} = 1.8$ ;  $B_{over} = 3.0$ ;  $\lambda = 0.1$ .

case of an intrinsically time dependent shock structure. The presence of fluctuations in the shock fields is reserved for future work, too.

The parameters  $B_{over}$ ,  $B_{foot}$ ,  $\xi$ ,  $\alpha$ ,  $\lambda$ ,  $\Delta$  define quantitatively the shape of the magnetic and electric profiles. The profiles used in the present paper are shown in Fig. 6.1. We used some characteristic quantities, with the purpose to give a dimensionless description of our system, useful for implementing the numerical code. The characteristic length is given by the ion skin depth of the proton, defined as

$$d = \frac{c}{\omega_{pi}}, \quad (6.8)$$

where  $c$  is the light speed and  $\omega_{pi}$  is the proton plasma frequency. A typical time  $\tau$  is derived by the ion Larmor frequency

$$\tau = \Omega_i^{-1} = \frac{m_p c}{e B_1}, \quad (6.9)$$

## 6.2 The numerical model

---

where  $m_p$  is the mass proton,  $e$  the elementary charge and  $B_1$  is the value of the upstream magnetic field. Considering the 6.8 and 6.9 we can define a normalization speed  $u$  as

$$u = \frac{d}{\tau} = \frac{\ell}{\omega_{pi}} \cdot \frac{eB_1}{m_p \ell}, \quad (6.10)$$

Reminding the expression of the ion plasma frequency,  $\omega_{pi} = \sqrt{\frac{m_p}{4\pi n_0 e^2}}$  and substituting into 6.10, we have:

$$u = \frac{m_p^{\frac{1}{2}}}{(4\pi n_0)^{\frac{1}{2}} \ell} \cdot \frac{\ell B_1}{m_p} = \frac{B_1}{(4\pi n_0 m_p)^{\frac{1}{2}}} = V_{A1}. \quad (6.11)$$

It is interesting to note from 6.11 that the normalization speed is equal to the Alfvén velocity upstream the shock. We can define the first dimensionless quantities like time, position and speed:

$$\hat{t} = \frac{t}{\tau}, \quad (6.12)$$

$$\hat{\mathbf{x}} = \frac{\mathbf{x}}{d}, \quad (6.13)$$

$$\hat{\mathbf{v}} = \frac{\mathbf{v}}{u}, \quad (6.14)$$

As just seen for the expression of the time unit  $\tau$ , we introduced the value of the upstream magnetic field  $B_1$  which we take as unit measure of the magnetic field. In this way the magnetic field is reduced to the dimensionless form:

$$\hat{\mathbf{B}} = \frac{\mathbf{B}}{B_1}. \quad (6.15)$$

Now, we give an the units for the electric field. From (6.7) we have:

$$\mathbf{E} = \frac{\mathbf{v} \times \mathbf{B}}{c} = \frac{\hat{\mathbf{v}} u \times \hat{\mathbf{B}} B_1}{c} = \hat{\mathbf{v}} \times \hat{\mathbf{B}} \left( \frac{u B_1}{c} \right). \quad (6.16)$$

In this way, the electric field assumes the form

$$\mathbf{E} = \hat{\mathbf{E}} \cdot E_{norm} = \hat{\mathbf{E}} \left( \frac{u B_1}{c} \right).$$

Considering also the same thing for the mass and the charge we have:

$$\hat{m} = \frac{m}{m_p}, \quad (6.17)$$

$$\hat{q} = \frac{q}{e}, \quad (6.18)$$

where  $m$  and  $q$  are the respectively the mass and charge of the particle, compared with the mass and elementary charge of proton. Now, we can put in dimensionless form the equations of particle motions, which are:

$$\frac{d\mathbf{x}}{dt} = \mathbf{v} \rightarrow \frac{d\hat{\mathbf{x}}}{d\hat{t}} \cdot \frac{d}{\tau} = \hat{v}u \rightarrow \frac{d\hat{\mathbf{x}}}{d\hat{t}} = \hat{v}, \quad (6.19)$$

and the equation:

$$m \frac{d\mathbf{v}}{dt} = q \left( \mathbf{E} + \frac{\mathbf{v} \times \mathbf{B}}{c} \right) \rightarrow \quad (6.20)$$

$$(\hat{m}m_p) \frac{d\hat{v}}{d\hat{t}} \frac{\mu}{\tau} = (\hat{q}e) \left( \frac{\mu B_1}{c} \right) (\hat{\mathbf{E}} + \hat{\mathbf{v}} \times \hat{\mathbf{B}}). \quad (6.21)$$

Knowing that  $\tau \left( \frac{eB_1}{m_p c} \right) = 1$  (see equation 6.5), we obtain:

$$\frac{d\hat{\mathbf{v}}}{d\hat{t}} = \tau \left( \frac{eB_1}{m_p c} \right) \left( \frac{\hat{q}}{\hat{m}} \right) (\hat{\mathbf{E}} + \hat{\mathbf{v}} \times \hat{\mathbf{B}}) = \frac{\hat{q}}{\hat{m}} (\hat{\mathbf{E}} + \hat{\mathbf{v}} \times \hat{\mathbf{B}}). \quad (6.22)$$

And so, the dimensionless equations are the following:

$$\frac{d\hat{\mathbf{x}}}{d\hat{t}} = \hat{v}, \quad (6.23)$$

$$\frac{d\hat{\mathbf{v}}}{d\hat{t}} = \frac{\hat{q}}{\hat{m}} (\hat{\mathbf{E}} + \hat{\mathbf{v}} \times \hat{\mathbf{B}}). \quad (6.24)$$

We use a *leap-frog* scheme of the second order for integrating the motion equations, advancing the positions at steps  $n\Delta t$  and the velocities at  $(n + \frac{1}{2})\Delta t$ . We have checked that the leap-frog scheme is much more reliable than the 4th order Runge-Kutta method, which indeed does not accurately describe trajectories in a magnetic field. A time step  $\Delta t = 2^{-8}\omega_{pi}^{-1}$  was used in order to have a good accuracy.

### 6.3 The integration scheme

We discuss the numerical scheme for integrating particle trajectories. Usually, a Runge-Kutta scheme (fourth or fifth order) is applied, but we developed a “*leap-frog*” scheme of the second order. The leap-frog scheme uses the method of finite difference for solving differential equations like other numerical schemes (*e.g.* Runge-Kutta). The differential equations are transformed into an algebraic form. Space and time are discretized with a fixed spacing:

$$\mathbf{x}_i = i\Delta\mathbf{x}, \quad (6.25)$$

$$t_n = n\Delta t. \quad (6.26)$$

### 6.3 The integration scheme

---

A general function is defined on the grid points and advanced forward in time for steps of  $\Delta t$  amplitude. In our case, the functions which we wish to integrate are defined, as seen in the last section, by the equation 6.23 and 6.24, where  $\hat{\mathbf{x}}$  and  $\hat{\mathbf{v}}$  are calculated at  $\Delta t$  steps. Using a centered Euler scheme for discretizing time derivatives, at a given  $t_n$  step we have:

$$\frac{x_i(t_n + \Delta t) - x_i(t_n)}{\Delta t} = v_i \left( t_n + \frac{\Delta t}{2} \right) + o(\Delta t^2), \quad (6.27)$$

$$\frac{v_i \left( t_n + \frac{\Delta t}{2} \right) - v_i \left( t_n - \frac{\Delta t}{2} \right)}{\Delta t} = f(x_{i,j,k}(t_n), v_{j,k}(t_n)) + o(\Delta t^2), \quad (6.28)$$

where the subscript  $i, j, k$  indicate the different components of the position and velocity vector (we do not put the hat on the variables for simplicity), and  $f$  is the second member of the equation 6.24 (it is possible to note that the function  $f$  depends on positions because the electric and magnetic fields depend on them). From 6.27 and 6.28, the positions and the speeds advanced in time are:

$$x_i(t_n + \Delta t) = x_i(t_n) + \Delta t v_i \left( t_n + \frac{\Delta t}{2} \right) + o(\Delta t^3), \quad (6.29)$$

$$v_i \left( t_n + \frac{\Delta t}{2} \right) = v_i \left( t_n - \frac{\Delta t}{2} \right) + \Delta t f(x_{i,j,k}(t_n), v_{j,k}(t_n)) + o(\Delta t^3). \quad (6.30)$$

The difficulty of this scheme is that for evaluating velocities at  $\frac{\Delta t}{2}$  steps, it is necessary to know also velocities at  $\Delta t$  steps because of the force term  $f$ . This problem can be solved by a forward scheme of velocities which allows to calculate  $v(t_n + \Delta t)$  from  $v(t_n + \frac{\Delta t}{2})$  at the first order:

$$v_i(t_n + \Delta t) = v_i \left( t_n + \frac{\Delta t}{2} \right) + \frac{\Delta t}{2} f \left( x_{i,j,k} \left( t_n + \frac{\Delta t}{2} \right), v_{j,k} \left( t_n + \frac{\Delta t}{2} \right) \right), \quad (6.31)$$

which requires to know the position at  $\frac{\Delta t}{2}$  that can be calculated by a simple mean:

$$x \left( t_n + \frac{\Delta t}{2} \right) = \frac{1}{2} [x(t_n + \Delta t) + x(t_n)]. \quad (6.32)$$

In this way, all positions and speeds are known for each time steps and can be advanced. Now we resume all steps that are implemented beginning from the initial conditions  $(x_i(0), v_i(0))$ :

- we initially advance speeds with an forward Euler scheme of the first order

$$v_i \left( \frac{\Delta t}{2} \right) = v_i(0) + f(x_{i,j,k}(0), v_{j,k}(0)) + o(\Delta t^2);$$

- positions can be advanced with a centered Euler scheme of the second order

$$x_i(\Delta t) = x(0) + v \left( \frac{\Delta t}{2} \right);$$

- we calculate positions at  $\frac{\Delta t}{2}$

$$x_i \left( \frac{\Delta t}{2} \right) = \frac{1}{2}(x_i(\Delta t) - x_i(0));$$

- we advance speeds at  $\Delta t$  with a forward scheme

$$v_i(\Delta t) = v_i \left( \frac{\Delta t}{2} \right) + f \left( x_{i,j,k} \left( \frac{\Delta t}{2} \right), v_{j,k} \left( \frac{\Delta t}{2} \right) \right);$$

- we finally calculate speeds at  $\frac{3\Delta t}{2}$

$$v_i \left( \frac{3\Delta t}{2} \right) = v_i \left( \frac{\Delta t}{2} \right) + f(x_{i,j,k}(\Delta t), v_{j,k}(\Delta t)).$$

At this point we can repeat the sequence of steps just described (except the first which starts from the initial conditions) and calculate position  $(x_i(2\Delta t), x_i(3\Delta t), \dots, x_i(n\Delta t))$  and speeds  $(v_i(\frac{5\Delta t}{2}), v_i(\frac{7\Delta t}{2}), \dots, v_i(n + \frac{\Delta t}{2}))$  for  $n$  steps with an accuracy of the second order in time.

## 6.4 Numerical results

We performed numerical simulations for different values of the upstream Mach number  $M_A = V_{x1}/V_{A1}$ , ranging from 2 to 4. These Mach numbers appear to be appropriate to the solar corona: for instance, recently [Bemporad & Mancuso \(2010\)](#) reported a CME driven shock in the corona at  $4 R_\odot$  with  $M_A \sim 1.81$ . We consider that the Mach number can be larger at lower altitudes, where the CME is originating from. Indeed, the explosive energy realised at the origin of CMEs should give stronger shocks near the source.

We inject particles with random speeds corresponding to a Maxwellian distribution such that the thermal speed is  $v_{th} = \frac{1}{2}V_{A1}$ . This corresponds to an upstream plasma  $\beta = \frac{1}{4}$ . For all particles, the bulk speed  $V_{x1}$  is added to the random “thermal” velocity, while the initial position is  $\mathbf{x} = (-20, 0, 0)$  for all particles. Since the present shock configuration is strictly 1-D, there would be no sense in changing the initial coordinates of the injected particles. The parameters of the simulations in dimensionless units are:  $B_1 = 1; B_2 = 3; \lambda = 0.1; B_{over} = 3; B_{foot} = 1.8; \xi = 0.6; \Delta = 0.2; \alpha = 0.1$  (Fig. 6.1).

## 6.4 Numerical results

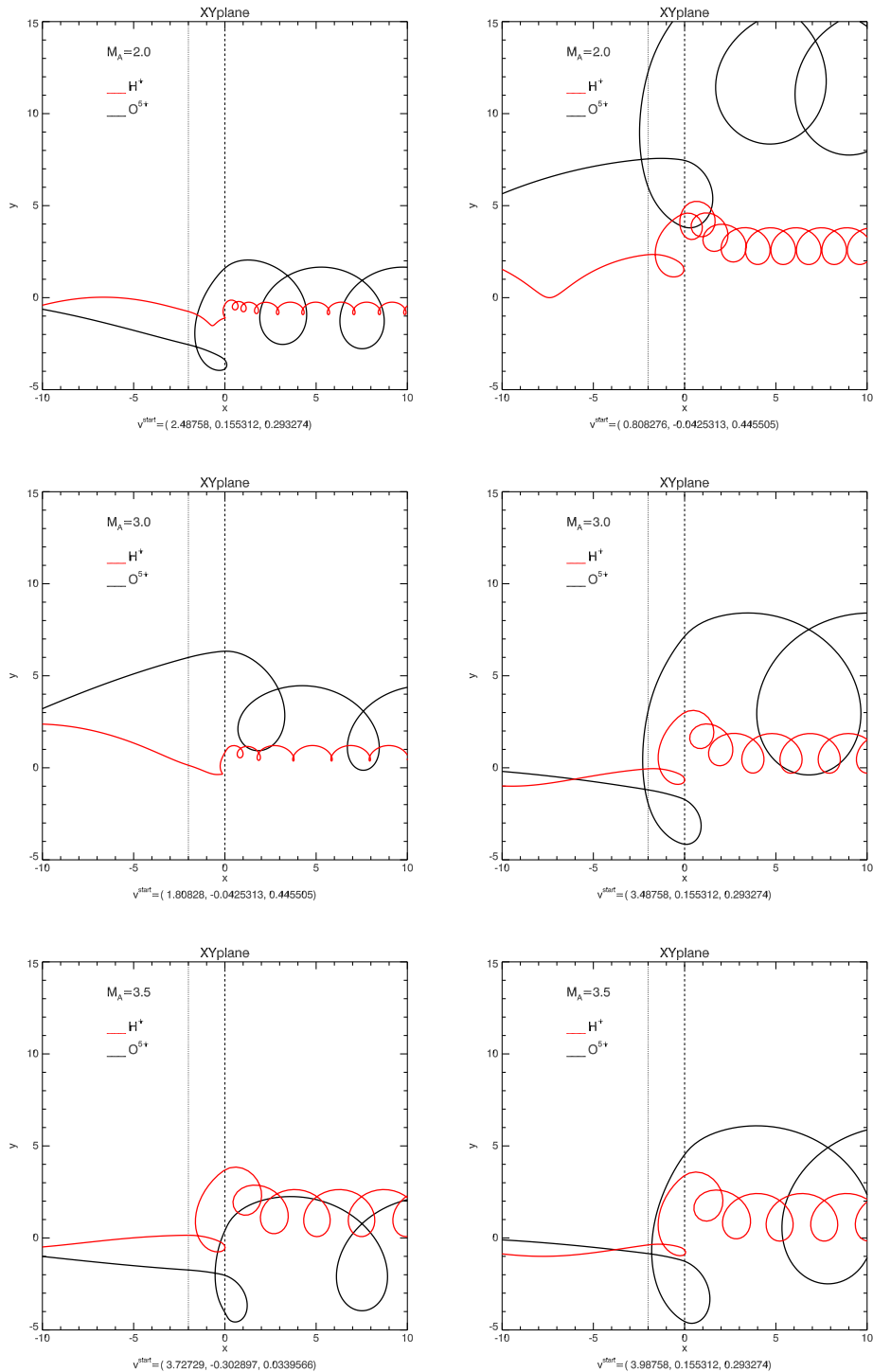


Figure 6.2: Sample trajectories in the  $xy$  plane. Top:  $M_A = 2$ . Middle:  $M_A = 3$ . Bottom:  $M_A = 3.5$ . Black line: oxygen, red line: proton. For each Mach number, two sample trajectories with different initial velocity (left and right panels) are shown. The dashed vertical bar at  $x = 0$  represents the shock ramp, while the dotted vertical bar represents the shock foot extent (color online). The upstream (downstream) region is found for  $x < 0$  ( $x > 0$ ).



Runs are performed simultaneously for protons and ions  $O^{5+}$ . Here we show the results for  $O^{5+}$  ions, since they have the largest mass to charge ratio, compared to  $He^{2+}$  and to  $Mg^{9+}$ , so that the  $O^{5+}$  reflection is more critical than that of other ion species. We show some trajectories in the  $xy$  plane for protons (red lines) and oxygen ions (black lines) (Fig. 6.2). Of the many trajectories which have been traced for different initial conditions of the ions, two couples of trajectories are shown for each of the Mach numbers ranging from  $M_A = 2, 3$  and  $3.5$ . In previous runs (not shown) we have verified that both the presence of the shock magnetic foot and of the magnetic overshoot are necessary to have efficient ion reflection, confirming the results of Leroy *et al.* (1982) and Gedalin (1996). These trajectories allow to distinguish the various behaviours (reflection or transmission) of particles for different upstream velocities. The shape of the trajectories during the reflection phase is consistent with that envisaged by Zimbardo (2009, 2011), with the  $O^{5+}$  ions performing a large arched orbit after reflection.

On the other hand, as far as the reflection is concerned, oxygen  $O^{5+}$  ions show an opposite behaviour with respect to protons: they are more easily reflected at low  $M_A$  (Fig. 6.2, right column), while protons are more easily reflected at larger Mach number. We have computed the proton and oxygen reflection rates by analyzing the particle trajectories. A particle is considered to be reflected if it crosses the shock ramp at  $x = 0$  and thereafter moves in the upstream direction for at least half of the foot length ( $x = -1c/\omega_{pi}$ ). By injecting 1000 particles of each species, we obtain the reflection rates reported in Table 6.1 for Mach numbers varying from  $M_A = 2$  to  $M_A = 4$ . This simple computation confirms that protons are more easily reflected for

$M_A$	$R_{H^+}(\%)$	$R_{O^{5+}}(\%)$
2.0	3.3	52.8
3.0	14.6	31.8
3.5	33.0	22.4
4.0	55.1	13.7

Table 6.1: Per cent reflection rates of protons and  $O^{5+}$  ions for different values of Mach number  $M_A$ .

large Mach number and oxygen ions for low Mach number, but, on the other hand, our test particle simulation uses the same shock structure for all Mach numbers, while the shock structure (like foot and ramp thickness, overshoot height, and electrostatic potential) is known to change with  $M_A$ . Therefore, a more reliable determination of the ion reflection rate requires the use of a self-consistent particle in cell simulation.

The ion dynamics can be also understood by studying the evolution

## 6.4 Numerical results

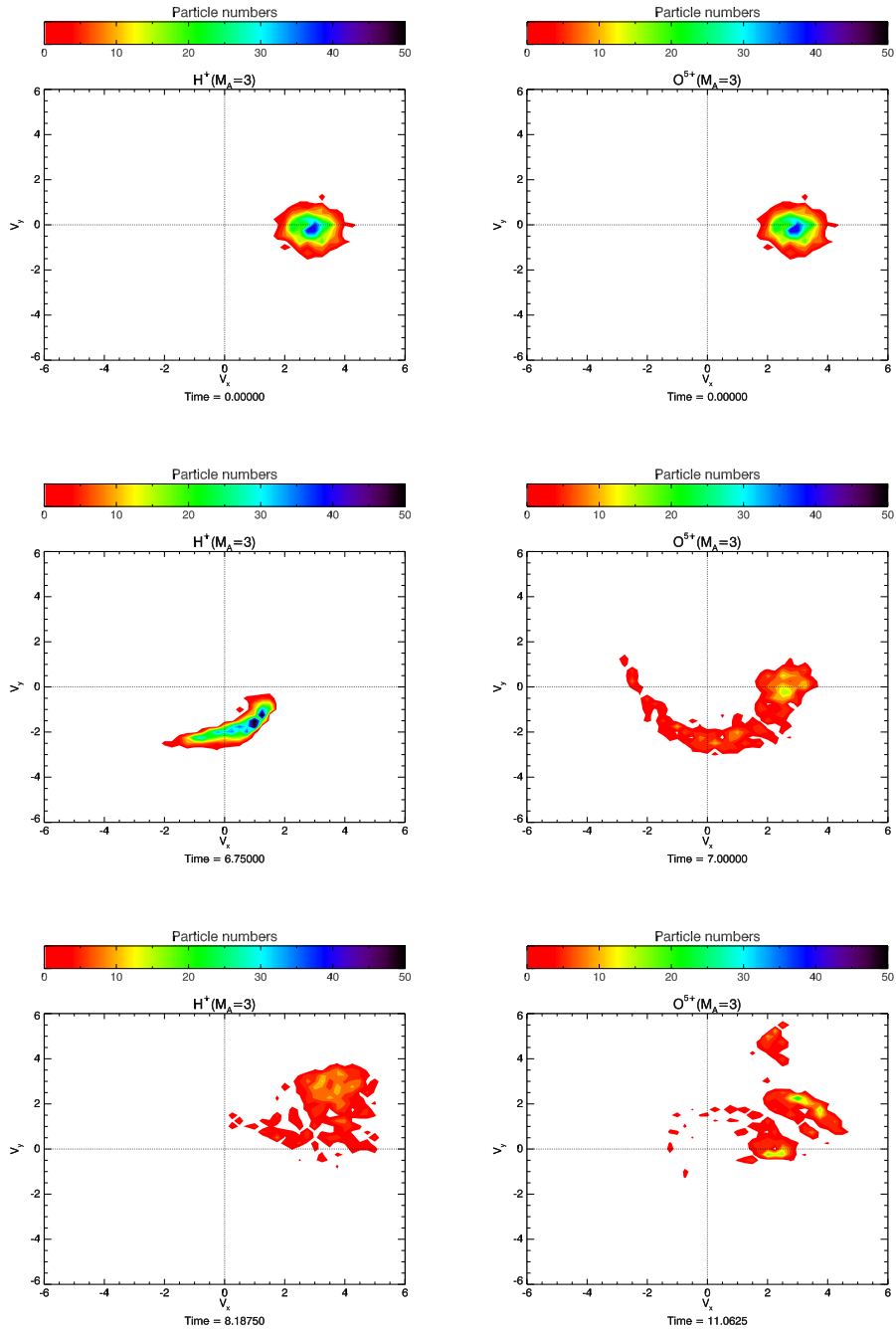


Figure 6.3: Ion velocity distribution in the  $v_x - v_y$  plane for Mach number  $M_A = 3$ . Left column: protons. Right column: oxygen ions. Top: upstream of the shock. Middle: at the shock ramp. Bottom: downstream of the shock (color online).

in time of the velocity distribution through the shock crossing. Fig. 6.3 shows the evolution of the proton (left column) and oxygen (right column) distributions in the  $v_x - v_y$  plane at different times: at particle injection upstream of the shock (upper panels), when crossing the shock ramp (middle panels), and downstream of the ramp (bottom panels). A total of 1000 particles of each species was injected. The middle panels show the ion reflection process, when the particle velocity attains  $v_y < 0$  due to the magnetic deflection in the magnetic ramp and overshoot, and  $v_x < 0$  because of the reflection itself. It can be seen that a “tail” of reflected particles is created both for protons and  $O^{5+}$  ions. Downstream of the ramp a broader distribution is found, which will gradually thermalize thanks to wave-particle interactions (which are not included in the present study).

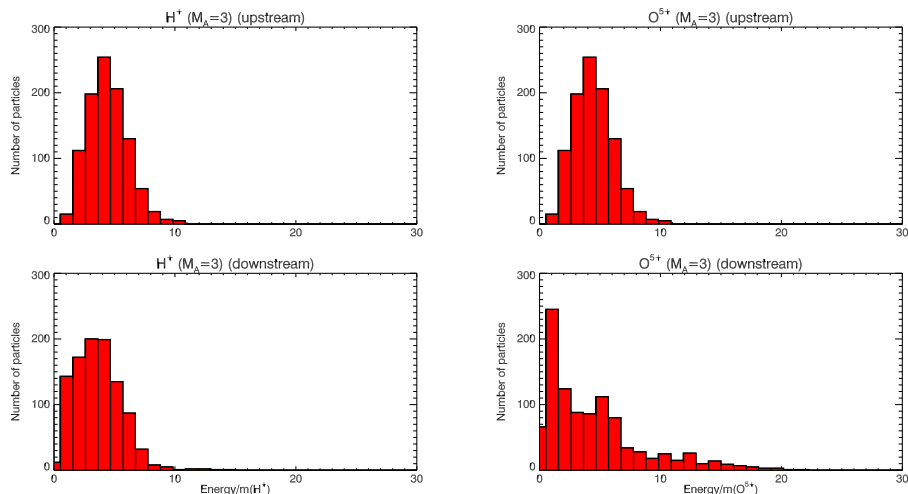


Figure 6.4: Evolution of the energy distribution per unit mass for protons (left) and oxygen ions (right) for  $M_A = 3$ . The energy distribution upstream of the shock (top) and downstream of the shock (bottom) are shown (color online).

Fig. 6.4 shows the distribution of energy per unit mass both upstream and downstream of the shock ramp, for  $M_A = 3$ . The energy distributions have been averaged over a gyroperiod, both upstream and downstream. For both protons and oxygen ions, the upstream distribution corresponds to the injected shifted Maxwellian. On the other hand, downstream both for protons and oxygen ions a low energy population appears which corresponds to particles which have just climbed the potential barrier (thus losing kinetic energy). Also, a high energy tail appears, but this is much more populated (and higher energies are reached) for oxygen than for protons. In other words, for  $M_A = 3$ , oxygen ions have both a larger reflection rate and a

larger velocity gain when compared with protons. Since what is actually plotted is  $v^2$ , when the latter quantity is multiplied times the mass, a more than mass proportional energy gain is obtained. Also, the different energies of the reflected and the transmitted populations, corresponding to different peaks, can be seen from the plots.

## 6.5 Summary

The preferential heating of heavy ions in the solar corona, as observed both by SoHO-UVCS and by in situ measurements in the solar wind, could be explained by the crossing of a supercritical quasi perpendicular shock (Zimbardo, 2009, 2010, 2011). In order to clarify the heating mechanism we have presented preliminary results of test-particle simulations for protons and oxygen ions crossing a model perpendicular shock. Runs have been performed for different Alfvénic Mach numbers. We have shown that heavy ions like  $O^{5+}$ , as well as protons, can be reflected and energized at shocks with Alfvénic Mach number  $M_A \sim 2 - 4$ . We have shown that oxygen ions have a reflection rate comparable to or larger than that of protons (depending in the Mach number), and that they have a larger energy gain per unit mass than protons. This corresponds to a preferential heating of oxygen  $O^{5+}$  ions.

These first numerical results show that this mechanism could work in the solar corona, so that ion reflection at collisionless shocks is a promising mechanism for explaining the more than mass proportional heating of heavy ions. In the present runs we only used the average electric and magnetic fields, neglecting their fluctuations. However, such fluctuations have a fundamental role in creating a thermal distribution, and will be included in the forthcoming runs. These will include electromagnetic fluctuations which can provide the thermalization mechanism by means of the wave particle interactions, as well as self-consistent Particle In Cell (PIC) codes, which will allow to study self-consistently the two populations of transmitted and reflected ions. These population should tend to merge when the fluctuating field will be included in the simulation.

Finally, we would like to point out that this model of heavy ion heating is an interesting example of cross-fertilization in space plasma physics, and in particular it tries to link the physics of solar corona heating to the physics of collisionless shocks, as best investigated by spacecraft in the solar wind. Various part of solar and space physics concur to the formulation of the proposed model. The non adiabatic heating of heavy ions comes from Speiser orbits in the magnetotail, where it can be shown that “resonant” ions can be accelerated to tens of keV (Zelenyi *et al.*, 2007; Dolgonosov *et al.*, 2010). In that case the ion acceleration is due to the constant dawn-dusk electric

field which is effective on the non magnetized part of the ion trajectory in the quasi-neutral sheet. This suggested that a similar acceleration can be obtained for reflected ion at shocks. Observations of preferential heating of heavy ions at shocks comes from Ulysses data on Corotating Interaction Regions (CIRs) shocks (Berdichevsky *et al.*, 1997); indeed, clearly enhanced heating of  $O^{6+}$  and  $He^{2+}$  with respect to  $H^+$  was observed by Ulysses. Heavy ion reflection from a magnetic barrier like the shock magnetic overshoot is akin to the ion orbits in the Ferraro-Rosenbluth sheath considered for the magnetopause, (*e.g.* Hughes, 1995). The formation of shocks in the reconnection outflow regions comes from solar flare models (Tsuneta & Naito, 1998) and from the numerical simulations of Yokoyama & Shibata (1996), and experimental evidence of reconnection and fast flows in the polar corona comes from Hinode and STEREO observations of coronal hole jets.

# Conclusions

The aim of this Ph.D. thesis has been to study some of the phenomena happening in the solar corona, like coronal hole jets and Coronal Mass Ejections, to investigate their complex dynamics and to probe the coronal structure of the Sun by assessing their physical properties, using data provided by STEREO, a solar space mission launched in 2006.

The STEREO mission (Solare TERrestrial Relations Observatory) consists of two identical spacecraft which orbit at about 1 AU respectively preceding (STEREO-Ahead) and trailing (STEREO-Behind) the Earth. They carry instruments for making in situ-measurements (*e.g.*, interplanetary magnetic field, solar wind speeds, particle densities) and remote sensing observations of the Sun. We exploited data provided by the SECCHI (Sun-Earth Connection Coronal and Heliospheric Investigation) package, more in particular data from the EUVI (Extreme UltraViolet Imager) telescope and COR1 (CORonagraph 1) coronagraph. The particularity of the STEREO mission, which distinguishes it from other solar missions, is the possibility to observe the Sun from two different perspectives, allowing the 3D reconstructions of solar features (*e.g.*, prominence, waves, CMEs,...). Indeed, the mission was conceived for determining the 3D shape of CMEs, useful for understanding how they influence the interplanetary medium, what is the true direction of propagation into space, whether they can impact on Earth and how they are leading to the formation of geomagnetic storms; these are all questions that cannot be answered using observations from a single point of view.

In this thesis we mainly focused on typical phenomena occurring in the solar corona: coronal hole jets, coronal mass ejections, and the associated shock waves. We presented the first comprehensive statistical study of jets occurred in polar coronal holes and in equatorial coronal holes, identified by both the EUVI and COR1 instruments of the STEREO/SECCHI mission. Our observations are made during a period of one year from March 2007 to April 2008, during the solar minimum, when activity is low and poles are occupied by large coronal holes, and the angular separation of the satellite spanned from 2 to 40 degrees. Observations were organized in two catalogues, in which we listed 79 polar and 15 equatorial jets (see Appendix [A.1](#) and [B.1](#)); the catalogues report the time of observations for each in-

struments, the position on the solar disk and the morphology associated to the event. As a matter of fact, a straightforward classification of equatorial jet morphology was not possible because of the difficult visibility of the jets observed at low latitudes, due to the presence of ambient brighter coronal structures, such as helmet streamers.

As a first step, we investigated the morphologies of polar jets (Chapter 2), and we classified them into three categories, in association with the possible underlying magnetic configuration of the field lines: *Eiffel tower* (ET) type jets in which jets show a shape similar to an Y-inverted and they are associated to a small magnetic bipole reconnecting with the ambient coronal field at its looptop; *lambda* ( $\lambda$ ) type jets in which ejection is observed to be shifted from the position of a bright point or a small loop, and this topology is associated to the magnetic configuration of a small bipole reconnecting with the unipolar coronal field at its footpoints; 5 events called *micro-CMEs* were seen, characterized by the evidence of a small loop that elongates from the solar surface and are similar to the CMEs but on smaller scale.

About 39% of the total 79 events exhibit a helical structure, can be associated with a twist of the magnetic field lines. For some event, we show the three dimensional reconstruction (see, Fig. 2.14, Chapter 2), performed thanks to STEREO data, showing that the twist is not a projection effect but it is a intrinsic feature.

The typical lifetimes in the EUVI FOV are 20 minutes at 171 Å, 30 minutes at 304 Å, while in COR1 the lifetimes are peaked at around 70–80 minutes. The corresponding speeds are 400 km/s for the hot 171 Å plasma component and only 270 km/s for the cooler 304 Å chromospheric component observed as the jet trailing part. The speed of 400 km/s is comparable to that derived from the COR1 FOV of 390 km/s. In summary we can conclude that the cooler chromospheric material in coronal jets commonly falls back to the Sun whereas the hotter leading flow caused by reconnection of magnetic fields escapes to larger heights as a jet subsequently visible in COR 1 images.

In order to determine physical parameters that are involved in the formation and evolution of jets, which are useful for giving a quantitative analysis and for having a good tool for comparison with numerical model, we calculated the electron temperature of jets from STEREO/EUVI data (Chapter 3). We discussed how to obtain the temperature maps and described the temperature evolution of jets in time with the purpose to emphasize the thermal structure. We adopted the filter ratio method and have provided a method to obtain 2-D temperature maps based on the estimation of the background at the sides of the jet region (Chae *et al.*, 2002; Schmelz *et al.*, 2003; Aschwanden *et al.*, 2008). Keeping in mind the uncertainties implicit in the method used, we obtained jet temperatures in the range 0.70–1.50 MK for two analysed jets, depending on the sensitivity of the filters. But the analysis for X-ray jets shows that they can have higher temperatures,

---

of the order of 5 MK (Shimojo & Shibata, 2000). The temperature maps show that heating and reconnection are going on in the jet well before the bright, collimated emission which is easily identified in EUV observations (1 hour before). This shows that the visible jet is only a part of the ongoing phenomenon of reconnection between the large scale field and the emerging magnetic bipoles. The hotter temperature are located at the reconnection site between the small-scale dipole emerging from the photosphere and seen in EUV images as a small loop and the large-scale unipolar field of the coronal hole. It appears that the plasma, heated by the reconnection process, escapes following the magnetic field and it is ejected into the corona, redistributing the temperature along the jet body. Our analysis is in good morphological agreement with numerical simulations (see Fig. 3.8, Chapter 3) and this can provide a validation of the models used to explain the formation and evolution of corona hole jets (Moreno-Insertis *et al.*, 2008).

Thanks to the relatively large number of jets in the catalogue, we were able to use polar coronal jets as a probe for understanding the magnetic field structure of the solar corona (Chapter 4). We assumed that jets, because the corona is an environment with a plasma- $\beta$  parameter less than 1, propagate along magnetic field lines. We measured the PA of jets at 1  $R_{\odot}$  in the EUVI FOV, and at 2  $R_{\odot}$  in the COR1 FOV, and analysed the deflection of jets. We found that jets are deflected toward low latitudes, in agreement with the assumption that magnetic field lines of the large scale dipole are bent toward the equator, but this deflection is more pronounced in the North Pole than in the South one. This North-South asymmetry has also been found in other datasets, starting from photospheric magnetic field measurements (Hoeksema, 1995), latitudinal gradient in solar energetic particles (Simpson *et al.*, 1996; Heber *et al.*, 1996a,b), and also from magnetic field measurements in the interplanetary medium by the Ulysses spacecraft (Erdős & Balogh, 2010). This asymmetry can be explained in terms of multipole components of the global magnetic field (Bravo & Gonzales-Esparza, 2000; Mursula & Hiltula, 2005): the quadrupole moment tends to affect the total magnetic field weakening it in the North pole and enhancing it in the South one. We tried to estimate the contribution of the quadrupole moment, starting from jet PA data, and compared with other results. We expressed the coronal magnetic field as the sum of the dipole, quadrupole, and esapole moments, starting from the expression of a scalar potential function  $\Phi$  in terms of spherical harmonics expansion. We traced magnetic field lines from the footpoint of jets (at 1  $R_{\odot}$ ) until 2  $R_{\odot}$  for different values of the magnetic moments with a Runge-Kutta scheme of the 4th order. We calculated the harmonics coefficients  $g_2^0$  and  $g_3^0$  and took into account that ones that minimize the standard deviation of position angles coming from the numerical simulation and the observation. We obtained as reliable values  $g_2^0 = -0.4 g_1^0$  and  $g_3^0 = 0.8 g_1^0$ . From these estimates, we were able to give a structure of the magnetic field lines (Fig. 4.8) in which the heliospheric current sheet



shows an offset of 7.45 degrees, a values close to that coming from other works (Mursula & Hiltula , 2005; Erdös & Balogh, 2010). This is an interesting result because it shows that the North-South asymmetry can be obtained from a dataset (the jet catalogue) independent than those quoted above, so that a more complete picture of this asymmetry is gained.

We also were interested to study the 3D structure of CMEs performed on a sample of 76 flux rope CMEs identified in SECCHI/COR2. They were analysed by the forward modeling technique from Thernisien *et al.* (2006), which allow to define the 3D shape of CMEs. In order to test the goodness of the model, we identified the source regions of the CMEs and compared their position with that obtained from the model. We found that there is an agreement between observations and modeling for about the 30% of all 76 CMEs events. The latitude and longitude off-set found for the other events could be due to a global deviation of the CME during its expansion, from the source regions in the low corona to  $10 R_{\odot}$ . The latitude off-set is consistent with that measured by Cremades & Bothmer (2004), and could be also explained by an effect of the fast solar wind from corona holes, which deviates CMEs toward low latitudes, encompassing the CME expansion at higher latitudes.

The possible formation of shocks in the reconnection outflow region of coronal hole jets or also CMEs, could give an explanation of preferential heating of heavy ions in the solar corona, as observed both by SoHO-UVCS and by in situ measurements in the solar wind (Chapter 6). We tested the validity of the model by Zimbardo (2009) in which  $O^{5+}$ , as well as protons, can be reflected and energized at shocks with test-particle simulations. These first numerical results show that  $O^{5+}$  energy distribution, after shock crossing, have a tail at higher energy with respect to that obtained for protons (Fig. 6.4), suggesting that ion reflection at collisionless shocks is a promising mechanism for explaining the more than mass proportional heating of heavy ions.

In summary, the various phenomena considered above show that coronal physics is a very rich research field, and that many connection exist between the various phenomena, highlighting the complexity of this field. All the properties of coronal hole jets and CMEs, that we discussed in this thesis, could be the subject of future investigations, thanks to the new planned solar mission *Solar Probe* and *Solar Orbiter*. Indeed, Solar Probe will fly close to the Sun at about  $10 R_{\odot}$ , providing direct measurements of the physical state of the solar corona, and Solar Orbiter will be able to observe the Sun poles, since its orbit will be out of the ecliptic plane up to more than 25 degrees in latitude, giving us information of these region that are difficult to observe in detail. These new missions will yield us new insights on jets, the propagation of CMEs, the structure of the solar corona, and solutions for the observed N-S asymmetry and the issue of the heavy ion heating.

## Appendix A

# Catalogue of polar coronal hole jets

In this appendix, polar and equatorial jet events are organized in a catalogue. Each event is labeled by progressive number, date of observation, angular separation  $\Delta\phi_{AB}$  between STEREO A and STEREO B, time of visibility in EUVI and in COR1, position angle in EUVI ( $\alpha$ ) and in COR1 ( $\beta$ ), brief indication on the morphology of the event and presence of helicity. The position angles are given for STEREO A, except when differently noted. The following abbreviations are used: **ET**: Eiffel tower;  $\lambda$ : lambda jet; **N(S)PCH**: North (South) polar coronal hole; **L**: limb; **I**: internal; **EDGE**: edge of coronal hole; **Hel**: evidence of helical structure. The question mark ? indicates unclassified jets events.

N°	Date $\Delta\phi_{AB}$	EUVI	COR1	Position Morphology
1	2007-03-19 2.16°	171 16:08-16:38	A:16:20-17:30	SPCH, L
		195 16:01-16:31	B:16:20-17:20	$\alpha(A) = 164^\circ$
		284 16:08-16:38		$\beta(A) = 158^\circ$
		304 16:01-16:31		?
2	2007-03-19 2.16°	171 16:08-16:28	A:16:10-17:20	SPCH, L
		195 16:01-16:31	B:16:20-17:30	$\alpha(A) = 176^\circ$
		284 15:58-16:28		$\beta(A) = 175^\circ$
		304		?
3	2007-03-20 2.20°	171	A:	NPCH, EDGE
		195	B: 08:51-09:31	$\alpha(B) = 6^\circ$
		284		$\beta(B) = 6^\circ$
		304 08:31-09:01		<b>Lambda</b>
4	2007-03-24 2.44°	171 00:38-00:58	A:01:10-02:20	SPCH, L
		195 00:31-00:51	B:01:10-02:30	$\alpha(A) = 181^\circ$
		284 00:48-00:58		$\beta(A) = 182^\circ$
		304 00:51 (very faint)		<b>ET</b>
5	2007-03-27 2.72°	171 not very clear	A:22:10-23:50	SPCH, L
		195 21:41-22:01 ?	B:22:10-23:30?	$\alpha(A) = 176^\circ$
		284 21:58-22:08		$\beta(A) = 167^\circ$
		304 21:51-22:11		?
6	2007-03-30 2.92°	171 14:49-15:01	A:15:20-16:30	NPCH, I
		195 14:42-14:52	B:15:10-16:30	$\alpha(A) = 1^\circ$
		284 14:40-15:00		$\beta(A) = 2^\circ$
		304 14:51		<b>ET</b>
7	2007-04-01 3.08°	171 14:24-14:54	A:14:40-16:00?	SPCH, L
		195 14:22-14:52	B:14:50-15:30?	$\alpha(A) = 170^\circ$
		284		$\beta(A) = 166^\circ$
		304 14:31-14:51		<b>Lambda</b>
8	2007-04-08 3.68°	171 15:09-15:31	A:15:30-16:30	SPCH, I
		195 15:12-15:22	B:15:40-16:50	$\alpha(A) = 192^\circ$
		284		$\beta(A) = 200^\circ$
		304 15:11-15:22		<b>Lambda</b>

Catalogue of polar coronal hole jets

9	2007-05-01	171 11:19-11:34 195 11:22-11:42 284 304 11:11-11:41	A:11:20-12:20 B:11:30-12:15	SPCH, L $\alpha(A) = 183^\circ$ $\beta(A) = 186^\circ$ ?
	6.15°			
10	2007-05-01	171 18:04-18:29 195 18:12-18:32 284 18:20 304 18:11-18:31	A:18:30-20:00 B:18:20-20:00?	NPCH, L $\alpha(A) = 0^\circ$ $\beta(A) = 1^\circ$ <b>ET-Hel</b>
	6.18°			
11	2007-05-02	171 13:01-13:16 195 13:02-13:22 284 13:00 304 13:01-13:51	A:13:10-14:30 B:13:15- ?	SPCH, EDGE $\alpha(A) = 153^\circ$ $\beta(A) = 152^\circ$ <b>ET-Hel</b>
	6.28°			
12	2007-05-02	171 20:59-21:21 195 21:02-21:22 284 304 21:01-21:31	A:21:20-22:10 B:21:10-22:35	NPCH, L $\alpha(A) = 0^\circ$ $\beta(A) = 1^\circ$ <b>ET-Hel</b>
	6.33°			
13	2007-05-04	171 09:48-10:01 195 09:46-10:01 284 09:46-10:01 304 09:50-10:20	A: B: (diff.movie(A):10:15)	SPCH, L $\alpha(A) = 177^\circ$ $\beta(A) = 175^\circ$ <b>Lambda</b>
	6.52°			
14	2007-05-05	171 04:03-04:18 195 04:06-04:21 284 04:06 304 04:05-04:35	A: B: (diff.movie(B):04:25-05:05)	NPCH, L $\alpha(B) = 16^\circ$ $\beta(B) = 26^\circ$ <b>Mini-CME</b>
	6.62°			
15	2007-05-06	171 08:26-08:48 195 08:26-08:56 284 08:26-08:56 304 08:31-09:10	A:08:40-09:15 B:08:55-09:40	SPCH, L $\alpha(A) = 172^\circ$ $\beta(A) = 167^\circ$ <b>Mini-CME</b>
	6.78°			
16	2007-05-07	171 195 14:46 284 304 14:50-15:05	A:15:30-16:30 B:difficult better seen in diff.movie	SPCH, L $\alpha(A) = 176^\circ$ $\beta(A) = 177^\circ$ ?
	6.94°			
17	2007-05-09	171 10:40 195 10:41 284 10:41 304 10:35-11:06	A:10:50-11:50? B:10:40-11:50?	NPCH, W, L $\alpha(A) = 346^\circ$ $\beta(A) = 316^\circ$ ?
	7.19°			
18	2007-05-10	171 195 284 304 07:33-07:51	A:08:10-09:30 B:	SPCH, I $\alpha(A) = 175^\circ$ $\beta(A) = 187^\circ$ ?
	7.31°			
19	2007-05-11	171 17:04-17:31 195 17:06-17:26 284 17:11-17:26 304 17:10-17:35	A: B: (diff.movie(A):17:45)	NPCH, L/EDGE $\alpha(A) = 346^\circ$ $\beta(A) = 333^\circ$ ?
	7.50°			
20	2007-05-24	171 09:28-09:46 195 09:25-09:55 284 304 09:36-09:56	A:09:55-10:35 B:09:55-10:35 very difficult observing signal in COR1	NPCH, L $\alpha(A) = 7^\circ$ $\beta(A) = 6^\circ$ <b>ET</b>
	9.38°			
21	2007-05-24	171 21:48-22:16 195 21:55 284 304 21:46-21:56	A:22:05-23:05 B:22:15-23:05	SPCH, L $\alpha(A) = 169^\circ$ $\beta(A) = 165^\circ$ <b>ET-Hel?</b>
	9.46°			
22	2007-05-25	171 03:18-03:41 195 03:25 284 03:26 304 03:16-03:46	A:02:45-04:45 B:03:05-03:55	SPCH, L $\alpha(A) = 182^\circ$ $\beta(A) = 185^\circ$ <b>ET-Hel</b>
	9.50°			
23	2007-05-27	171 19:38-19:58 195 19:45-19:55 284 19:46 304 19:46-19:56	A:20:05-21:15? B:20:05-21:25	NPCH, L $\alpha(A) = 2^\circ$ $\beta(A) = 0^\circ$ <b>ET-Hel</b>
	9.92°			
24	2007-05-28	171 23:46-00:08 195 23:45-00:15 284 304 23:56-00:16	A:00:15-00:45 B:	SPCH, L $\alpha(A) = 176^\circ$ $\beta(A) = 175^\circ$ ?
	10.11°			
25	2007-06-07	171 04:58-05:43 195 04:55-05:55 284 05:06-05:46 304 05:06-05:56	A:05:25-07:05 B:05:25-07:05	NPCH, I $\alpha(A) = 7^\circ$ $\beta(A) = 12^\circ$ <b>ET-Hel</b>
	11.65°			
26	2007-06-13	171 not clear 195 19:25-20:15 284 19:26 304 19:26-19:46	A: B:19:55-20:25	NPCH, I $\alpha(B) = 0^\circ$ $\beta(B) = 2^\circ$ <b>ET</b>
	12.81°			
27	2007-07-24	171 00:58-01:06 195 01:05-01:15 284 304 00:56-01:26	A:01:15-02:05 B:01:15-02:35 very faint in COR1A	NPCH, I $\alpha(B) = 359^\circ$ $\beta(B) = 356^\circ$ <b>?-Hel?</b>
	20.57°			
28	2007-08-04	171 20:38-20:48 195 20:45 284 20:46 304 20:36-20:46	A:20:55-22:15 B:	NPCH, L $\alpha(A) = 1^\circ$ $\beta(A) = 0^\circ$ <b>ET</b>
	22.97°			
29	2007-08-13	171 01:08-01:26 195 01:15-01:25	A:01:35-02:45 B:01:35-03:06	NPCH, I $\alpha(A) = 356^\circ$

	24.63°	284 01:06 304 01:16-01:36		$\beta(A) = 351^\circ$ <b>ET</b>
30	2007-09-03	171 08:36-09:01 195 08:35-08:55 284 08:46 304 08:36-09:06	A: B:08:55-10:05?	NPCH, L $\alpha(B) = 1^\circ$ $\beta(B) = 359^\circ$ <b>ET-Hel</b>
	28.85°			
31	2007-09-07	171 16:16-16:46 195 16:25-16:35 284 16:26 304 16:16-16:46	A:16:40-17:15 B:16:40-17:20 faint in A	NPCH, EDGE $\alpha(B) = 18^\circ$ $\beta(B) = 26^\circ$ <b>Lambda-Hel</b>
	29.68°			
32	2007-09-09	171 13:08-14:16 195 13:05-14:15 284 13:26-13:46 304 13:36-13:56	A:13:35-15:00 B:13:35-15:05	NPCH, L/I $\alpha(A) = 10^\circ$ $\beta(A) = 16^\circ$ <b>ET-Hel</b>
	30.04°			
33	2007-09-11	171 12:18-12:56 195 12:25-12:55 284 12:26-12:46 304 12:16-12:56	A:12:55-14:05 B:12:45-14:35	NPCH, EDGE $\alpha(A) = 26^\circ$ $\beta(A) = 42^\circ$ ?
	30.41°			
34	2007-09-15	171 14:46-14:56 195 14:55 284 14:46 304 14:46-14:56	A:15:05-15:45 B:15:05-16:05	SPCH, EDGE/L $\alpha(A) = 164^\circ$ $\beta(A) = 153^\circ$ <b>Lambda</b>
	31.17°			
35	2007-09-23	171 11:26-11:50 195 11:36-11:55 284 11:26-11:46 304 11:26-11:56	A:12:05-13:15 B:11:45-13:15	NPCH, I/L $\alpha(A) = 346^\circ$ $\beta(A) = 331^\circ$ <b>Lambda</b>
	32.59°			
36	2007-09-28	171 11:06-11:16 195 11:05-11:15 284 11:06-11:26 304 11:06-11:16	A:11:25-12:25 B:11:20-12:50	NPCH, EDGE/L $\alpha(A) = 344^\circ$ $\beta(A) = 332^\circ$ <b>ET-Hel</b>
	33.46°			
37	2007-10-01	171 23:26-23:36 195 23:25 284 23:26 304 23:26-23:36	A:23:30-00:30 B:	NPCH, L $\alpha(A) = 359^\circ$ $\beta(A) = 352^\circ$ ?
	34.06°			
38	2007-10-05	171 08:06-09:06 195 08:05-09:05 284 08:06-08:46 304 08:06-09:06	A:08:40-10:00 B:08:35-09:55	NPCH, I $\alpha(A) = 354^\circ$ $\beta(A) = 349^\circ$ ?
	34.62°			
39	2007-10-06	171 06:06-06:26 195 06:15-06:25 284 06:06-06:26 304 06:06-06:26	A:06:05-07:35 B:06:05-08:05	SPCH, EDGE $\alpha(A) = 207^\circ$ $\beta(A) = 224^\circ$ ?
	34.77°			
40	2007-10-06	171 20:21-20:38 195 20:15-20:35 284 20:26 304 20:26-20:46	A:20:45-21:55 B:20:35-21:15	NPCH, I $\alpha(A) = 354^\circ$ $\beta(A) = 348^\circ$ <b>ET-Hel</b>
	34.86°			
41	2007-10-12	171 23:51-00:16 195 23:55-00:25 284 304 23:56-00:56	A:00:05-01:00 B:	SPCH, I $\alpha(A) = 182^\circ$ $\beta(A) = 184^\circ$ <b>Mini-CME-Hel</b>
	35.84°			
42	2007-10-18	171 15:34-15:59? 195 15:45-15:55 284 15:46 304 15:36-16:06	A: B: (diff.movie(A):16:05) very faint	SPCH, L $\alpha(A) = 178^\circ$ $\beta(A) = 180^\circ$ <b>ET</b>
	36.71°			
43	2007-10-21	171 22:16-22:56 195 22:15-22:25 284 22:06-22:46 304 22:26-22:56	A:22:40-23:20 B:22:45-23:30	SPCH, L $\alpha(A) = 184^\circ$ $\beta(A) = 186^\circ$ <b>ET-Hel</b>
	37.19°			
44	2007-11-01	171 00:38-00:46 195 00:45 284 00:46-01:26 304 00:46-01:26	A:00:55-02:05 B:01:05-02:05 faint	SPCH, L $\alpha(A) = 169^\circ$ $\beta(A) = 172^\circ$ <b>ET</b>
	38.58°			
45	2007-11-01	171 02:21-02:46 195 02:25-02:55 284 02:26 304 02:26-02:46	A:02:55-03:45 B: not seen in B	SPCH, L $\alpha(A) = 168^\circ$ $\beta(A) = 163^\circ$ <b>ET</b>
	38.59°			
46	2007-11-03	171 04:06-04:39 195 04:05-04:45 284 04:06-04:46 304 04:06-04:56	A:04:45-05:35 B:04:45-05:45	SPCH, L $\alpha(A) = 191^\circ$ $\beta(A) = 196^\circ$ <b>Lambda-Hel</b>
	38.86°			
47	2007-11-04	171 01:56-02:56 195 01:55-02:55 284 02:06 304 02:06.03:06	A:02:55- ? B: very faint	NPCH, L $\alpha(A) = 355^\circ$ $\beta(A) = 354^\circ$ <b>ET-Hel</b>
	38.97°			
48	2007-11-06	171 00:28-00:46 195 00:35-00:45 284 304 00:36-00:56	A:00:45-02:15 B:00:45-02:05	SPCH, L $\alpha(A) = 176^\circ$ $\beta(A) = 177^\circ$ <b>ET</b>
	39.22°			
49	2007-11-09	171 02:53-03:36 195 284 02:46 304 02:56-03:46	A:03:25-04:35 B:03:15-04:35	NPCH, L $\alpha(A) = 348^\circ$ $\beta(A) = 332^\circ$ <b>Mini-CME</b>
	39.60°			

Catalogue of polar coronal hole jets

50	2007-11-09	171 21:36-21:53 195 21:36-22:16 284 304 21:46-22:16	A:21:55-23:15 B:22:05-22:35	SPCH, EDGE/L $\alpha(A) = 151^\circ$ $\beta(A) = 147^\circ$ <b>Lambda</b>
51	2007-11-17	171 17:08-17:23 195 17:15-17:45 284 17:26 304 17:16-17:26	A:17:25-19:15 B:17:25-18:55	NPCH, I $\alpha(A) = 6^\circ$ $\beta(A) = 7^\circ$ <b>Lambda-Hel</b>
52	2007-11-19	171 09:53-10:21 195 09:55-10:25 284 10:06 304 09:56-10:26	A:10:45-11:55 B:10:35-12:05	NPCH, EDGE $\alpha(A) = 328^\circ$ $\beta(A) = 327^\circ$ ?
53	2007-11-21	171 21:28-22:26 195 21:35-22:26 284 21:26-21:46 304 21:16-22:26	A:22:15-23:35 B:	NPCH, EDGE/L $\alpha(A) = 18^\circ$ $\beta(A) = 34^\circ$ <b>?-Hel</b>
54	2007-11-26	171 22:53-23:16 195 22:45-23:25 284 304 22:56-23:26	A:23:15-23:55? B:23:25-23:55?	SPCH, L $\alpha(A) = 191^\circ$ $\beta(A) = 196^\circ$ <b>?-Hel</b>
55	2007-12-01	171 195 14:45-15:25 284 15:06 304 14:46-15:06	A:14:55-16:55 B:14:45-17:05	NPCH, I $\alpha(A) = 10^\circ$ $\beta(A) = 18^\circ$ <b>ET</b>
56	2007-12-02	171 195 13:15-13:35 284 304 13:06-13:26	A:13:45-15:15 B:13:35-15:15	NPCH, I $\alpha(A) = 10^\circ$ $\beta(A) = 18^\circ$ <b>ET</b>
57	2007-12-03	171 195 01:25 284 304 01:26-01:46	A:01:55-02:35 B:01:55-03:35	SPCH, L $\alpha(B) = 178^\circ$ $\beta(B) = 167^\circ$ ?
58	2007-12-03	171 03:51-04:26 195 03:55 284 304 03:46-04:16	A:04:05-05:15 B:04:15-05:15	SPCH, L $\alpha(A) = 191^\circ$ $\beta(A) = 197^\circ$ <b>?-Hel</b>
59	2007-12-03	171 04:46-05:16 195 04:45-05:25 284 04:46-05:26 304 04:46-05:26	A:05:05-06:35? B:05:05-06:05?	NPCH, L $\alpha(A) = 10^\circ$ $\beta(A) = 16^\circ$ <b>?-Hel</b>
60	2007-12-04	171 01:06-01:21 195 00:55-01:05 284 304 01:06-01:36	A: not visible B:01:15-02:00 faint (diff.movie(B):01:25)	SPCH, L $\alpha(B) = 180^\circ$ $\beta(B) = 181^\circ$ <b>ET</b>
61	2007-12-05	171 10:53-11:26 195 11:05-11:25 284 304 10:56-11:26	A:11:25-12:45 B:11:15-12:55	NPCH, I $\alpha(A) = 7^\circ$ $\beta(A) = 9^\circ$ <b>?-Hel</b>
62	2007-12-06	171 15:31-16:09 195 15:05-15:35 284 304 15:16-16:16	A: B: (diff.movie(B):16:05)	NPCH, I $\alpha(B) = 352^\circ$ $\beta(B) = 348^\circ$ <b>ET-Hel</b>
63	2007-12-06	171 19:21-19:36 195 19:45 284 19:26 304 19:26-19:46	A: B: (diff.movie(B):19:45-20:05)	NPCH, L $\alpha(B) = 355^\circ$ $\beta(B) = 351^\circ$ ?
64	2007-12-09	171 07:56 195 07:55-08:25 284 304 07:56-08:26	A:08:15-10:15 B:08:25-09:45	SPCH, L $\alpha(A) = 174^\circ$ $\beta(A) = 172^\circ$ <b>ET</b>
65	2007-12-11	171 19:56-20:13 195 19:35-19:45 284 20:06 304 19:46-20:16	A:20:05-21:00? B:20:05-21:05	NPCH, L $\alpha(A) = 0^\circ$ $\beta(A) = 0^\circ$ ?
66	2007-12-12	171 21:56-22:38 195 21:55 284 22:06 304 21:56-22:46	A: B: not visible (diff.movie(A):22:25)	SPCH, L $\alpha(A) = 178^\circ$ $\beta(A) = 177^\circ$ <b>ET-Hel</b>
67	2007-12-12	171 22:21-22:46? 195 22:25-22:46 284 22:26 304 22:26-22:56	A: B: (diff.movie(A):23:05) faint signature	NPCH, EDGE $\alpha(A) = 31^\circ$ $\beta(A) = 56^\circ$ <b>Lambda</b>
68	2007-12-17	171 04:11-04:28 195 04:15-04:45 284 04:26 304 04:16-04:46	A: B: (diff.movie(A):04:25-05:05)	SPCH, EDGE $\alpha(A) = 201^\circ$ $\beta(A) = 216^\circ$ <b>ET</b>
69	2007-12-21	171 04:48-05:03 195 04:55-05:15 284 304 04:46-05:16	A: B:05:15-06:25	NPCH, I $\alpha(B) = 353^\circ$ $\beta(B) = 351^\circ$ <b>ET-Hel</b>
70	2007-12-22	171 03:03-03:38	A:	NPCH, L

---

	43.46°	195 03:05-03:35 284 03:26 304 03:06-03:46	B:03:20-04:50	$\alpha(B) = 351^\circ$ $\beta(B) = 347^\circ$ <b>ET-Hel</b>
71	2008-01-09	171 07:36-07:57 195 07:45-08:00 284 07:36-07:56 304 07:41-08:06	A:08:05-08:55 B:07:55-09:00	NPCH, L $\alpha(A) = 351^\circ$ $\beta(A) = 344^\circ$ <b>ET-Hel</b>
72	2008-01-20	171 00:16-00:31 195 00:15-00:30 284 00:16 304 00:17-00:39	A:00:25-01:35 B:00:20-01:10 very faint in A	NPCH, L/I $\alpha(B) = 1^\circ$ $\beta(B) = 9^\circ$ <b>ET</b>
73	2008-01-20	171 16:26-17:11 195 16:30-17:10 284 16:26-17:11 304 16:28-17:12	A: B: (diff.movie(B):17:10)	NPCH, EDGE $\alpha(B) = 340^\circ$ $\beta(B) = 321^\circ$ <b>Mini-CME-Hel?</b>
74	2008-02-02	171 13:18-13:41 195 13:25-13:35 284 13:26 304 13:16-13:56	A:13:35-14:15 B:13:35-14:05 very faint in A	NPCH, L $\alpha(B) = 352^\circ$ $\beta(B) = 349^\circ$ <b>Lambda-Hel</b>
75	2008-02-08	171 08:33-08:43 195 08:35-08:45 284 304 08:36-08:56	A:08:45-09:35 B:08:40-10:00	NPCH, L $\alpha(A) = 351^\circ$ $\beta(A) = 342^\circ$ <b>?-Hel</b>
76	2008-02-17	171 03:36-03:56 195 03:35-03:55 284 304 03:36-04:06	A:04:05-05:35 B: not recognizable in B	SPCH, I $\alpha(A) = 159^\circ$ $\beta(A) = 164^\circ$ <b>ET</b>
77	2008-03-02	171 07:41-08:26 195 07:45-08:25 284 07:46-08:06 304 07:36-07:46	A:07:55-08:55 B:07:55-08:55	NPCH, L $\alpha(A) = 14^\circ$ $\beta(A) = 31^\circ$ ?
78	2008-03-27	171 06:23-07:06 195 06:25-07:05 284 06:26-06:46 304 06:26-07:06	A:06:45-07:55 B:06:35-07:45	NPCH, I/EDGE $\alpha(A) = 2^\circ$ $\beta(A) = 357^\circ$ <b>ET-Hel</b>
79	2008-04-02	171 08:31-08:46 195 08:35-09:15 284 304 08:36-08:56	A:08:55-10:05 B:08:55-10:15	SPCH, L $\alpha(A) = 185^\circ$ $\beta(A) = 188^\circ$ <b>ET-Hel</b>

---



## Appendix B

# Catalogue of equatorial coronal hole jets

N	Date	$\lambda(\text{\AA})$	COR1 A	EUVI A	COR1 B	EUVI B	Position
							$\Delta\phi$
1	2007-03-31	171	22:30		22:40		
2.9		195 284 304				21:52-22:32	$\alpha(B) = 120^\circ$ $\beta(B) = 118^\circ$
2	2007-04-07	171	16:40	15:59-16:41	16:40	15:59-16:41	
3.4		195 284 304		15:22-16:42 16:00-16:40		15:42-16:32 16:00-16:40	$\alpha(A) = 70^\circ$ $\beta(A) = 76^\circ$
3	2007-04-30	171	22:40	22:29-22:49	22:40	?	
5.9		195 284 304		22:32-22:42			$\alpha(A) = 259^\circ$ $\beta(A) = 241^\circ$
4	2007-05-01	171	21:30	20:54-21:26	21:30	20:54-21:26	
6.1		195 284 304		21:01-21:21		21:01-21:21	$\alpha(B) = 255^\circ$ $\beta(B) = 249^\circ$
5	2007-05-16	171	13:05		13:25		
8.0		195 284 304		12:30-12:45			$\alpha(A) = 104^\circ$ $\beta(A) = 104^\circ$
6	2007-10-03	171	-	-	10:06	09:33-10:03	
34.4		195 284 304				09:35-09:55	$\alpha(B) = 255^\circ$ $\beta(B) = 251^\circ$
7	2007-10-10	171	-	-	22:06	09:36-10:06	
35.5		195 284 304				21:26-21:46 21:35-21:45	$\alpha(B) = 85^\circ$ $\beta(B) = 77^\circ$
8	2007-10-14	171	-	-	11:05	21:26-21:56	
36.1		195 284 304				10:26-11:26	$\alpha(B) = 104^\circ$ $\beta(B) = 94^\circ$
9	2007-10-15	171	-	-	17:46	10:36-11:06	
36.2		195 284 304				17:13-17:43 17:25-17:45	$\alpha(B) = 112^\circ$ $\beta(B) = 97^\circ$
10	2007-11-11	171	-	-	16:05	17:16-17:46	
39.6		195 284 304				15:41-16:08 15:45-15:55 15:46 15:36-16:16	$\alpha(B) = 112^\circ$ $\beta(B) = 81^\circ$
11	2007-11-15	171	01:05	00:31-01:06	-	-	
40.1		195 284 304		00:45-01:05 00:36-01:06			$\alpha(A) = 116^\circ$ $\beta(A) = 115^\circ$
12	2007-11-18	171	-	-	05:25		
40.3		195 284 304				04:56-05:36	$\alpha(B) = 256^\circ$ $\beta(B) = 265^\circ$
13	2007-11-18	171	05:45	05:06-05:43	-	-	



## Catalogue of equatorial coronal hole jets

---

40.3		195		05:16-05:35			$\alpha(A) = 124^\circ$
		284		05:26			$\beta(A) = 126^\circ$
		304		05:06-05:26			
14	2007-11-22	171	-	-	11:25	10:56-11:33	
40.8		195				11:05-11:35	$\alpha(B) = 242^\circ$
		284					$\beta(B) = 239^\circ$
		304				11:06-11:36	
15	2007-12-12	171	11:45	11:18-11:46	11:45	-	
42.9		195		11:15-11:45			$\alpha(A) = 134^\circ$
		284					$\beta(A) = 131^\circ$
		304		11:16-11:46			

# Bibliography

- Alexander, D., Fletcher, L., High resolution observation of plasma jets in the solar corona, *Solar Phys.*, 190: 167–184, 1999. [14](#)
- Altschuler, M. D., Newkirk, G. Jr., Magnetic Fields and the Structure of the Solar Corona. I: Methods for Calculating Coronal Fields, *Solar Phys.*, 9, 131–149, 1969. [54](#)
- Aschwanden, M., Physics of the Solar Corona, Springer, 2006. [5](#), [6](#), [8](#), [38](#), [54](#)
- Aschwanden, M. J., Nitta, N. V., Wuelser, J.-P., Lemen, J. R., First 3D reconstruction of coronal loops with the *STEREO A+B* spacecraft. II. Electron density and temperature measurements, *Astrophys. J.*, 680:1477–1495, 2008. [34](#), [38](#), [41](#), [43](#), [92](#)
- Aurass, H., Mann, G., Radio Observation of Electron Acceleration at Solar Flare Reconnection Outflow Termination Shocks, *Astrophys. J.*, 615, 526–530, 2004. [76](#)
- Bale, S.D., Balikhin, M. A., Horbury, T. S., Krasnoselskikh, V. V., Kucharek, H., Möbius, E., Walker S. N., Balogh, A., Burgess, D., Lembège, B., Lucek, E. A., Scholer, M., Schwartz, S. J., and Thomsen, M.F., Quasi-perpendicular Shock Structure and Processes, *Space Sci. Rev.*, 118: 161–203, doi: 10.1007/s11214-005-3827-0, 2005. [77](#)
- Bemporad, A., Mancuso, S., First complete determination of plasma physical parameters across a Coronal Mass Ejection-driven shock, *Astron. J.*, 720, 130–143, 2010. [9](#), [76](#), [84](#)
- Berdichevsky, D., Geiss, J., Gloeckler, G., Mall, U., Excess heating of  $^4\text{He}^{2+}$  and  $\text{O}^{6+}$  relative to  $\text{H}^+$  downstream of interplanetary shocks, *J. Geophys. Res.*, 102, Issue A2, 2623–2636, 1997. [90](#)
- Bravo, S., and J.-A. Gonzales-Esparza, The north-south asymmetry of the solar and heliospheric magnetic field during activity minima, *Geophys. Res. Lett.*, 27, 847–850, doi:10.1029/1999GL010709, 2000. [53](#), [62](#), [93](#)

- Bothmer, V., Schwenn, R., The structure and origin of magnetic clouds in the solar wind, *Annales Geophysicae*, 16, 1–24, 1998. [65](#)
- Bothmer, V., Nisticò, G., Zimbardo, G., Patsourakos S., Bosman, E., The nature of micro CMEs within coronal holes, Symposium E, session 21, paper number E21-0015-10 (Oral), 38th COSPAR Scientific Assembly, Bremen, Germany, 18–15 July 2010. [9](#)
- Burgess, D., Wilkinson, W. P., Schwartz, S. J., Ion distributions and thermalization at perpendicular and quasi-perpendicular supercritical collisionless shocks, *J. Geophys. Res.*, 94, 8783–8792, 1989. [79](#)
- Chae, J., Park, Y.-D., Moon, Y.-J., Wang, H., Yun, H. S., Temperature of Extreme-Ultraviolet-Emitting plasma structures observed by the *Transition Region And Coronal Explorer*, *Astrophys. J.*, 567, L159-L163, 2002. [36](#), [92](#)
- Cirtain, J. W., Golub, L., Lundquist, L., van Ballegoijen, A., Savcheva, A., Shimojo, M., DeLuca, E., Tsuneta, S., Sakao, T., Reeves, K., Weber, M., Kano, R., Narukage, N., Shibasaki, K., Evidence for Alfvén Waves in Solar X-ray Jets, *Science*, Volume 318, Issue 5856, pp. 1580, 2007 [27](#), [76](#)
- Cremades, H., Bothmer, V., On the three-dimensional configuration of coronal mass ejections, *Astron. Astrophys.*, 422, 307–322, 2004. [24](#), [51](#), [65](#), [66](#), [70](#), [74](#), [94](#)
- Dolgonosov, M. S., Zimbardo, G., Greco, A., Influence of the electric field perpendicular to the current sheet on ion beamlets in the magnetotail, *J. Geophys. Res.*, 115, A2, ID A02209, 2010. [89](#)
- Doschek, G. A., Landi, E., Warren, H. P., & Harra, L. K., Bright points and jets in polar coronal holes observed by the Extreme-Ultraviolet Imaging Spectrometer on Hinode, *Astrophys. J.*, 710, 1806–1824, 2010. [37](#)
- Bosman, E., Bothmer V., Nisticò, G., Vourlidas, A., Howard, R. A., Davies, J. A., 3-Dimensional properties of Coronal Mass Ejections from STEREO/SECCHI observations, *Solar Phys.*, submitted, 2011. [10](#), [67](#), [68](#), [73](#)
- Edmiston, J. P., Kennel, C. F., A parametric survey of the first critical Mach number for a fast MHD shock, *J. Plasma Phys.*, 32, 429–441, 1982. [77](#)
- Erdős, G., and A. Balogh, The symmetry of the heliospheric current sheet as observed by Ulysses during the fast latitude scan, *Geophys. Res. Lett.*, 25, 245–248, doi:10.1029/97GL53699, 1998. [52](#)
- Erdős, L., Balogh, M. L., North-south asymmetry of the location of the heliospheric current sheet revisited, *J. Geophys. Res.*, 115, A01105, 2010. [52](#), [62](#), [93](#), [94](#)

## BIBLIOGRAPHY

---

- Feldman, U., Elemental abundances in the upper solar atmosphere, *Solar Phys.*, Vol. 46, 3, 202–220, 1992. [35](#), [41](#)
- Filippov, B., Golub, L., Koutchmy, S., X-Ray Jet Dynamic in Polar Coronal Hole Region, *Solar Phys.*, 254, 259–269, 2009. [14](#)
- Fisk, L. A., Motion of the footpoints of heliospheric magnetic field lines at the Sun: Implication for recurrent energetic particle events at high heliographic latitudes, *J. Geophys. Res.*, 101, 15,47–15-553, 1996. [50](#)
- Gedalin, M., Ion reflection at the shock front revisited, *J. Geophys. Res.*, 101, A3, 4871–4878, 1996. [78](#), [79](#), [86](#)
- Gontikakis, C., Archontis, V., & Tsinganos, K., Observations and 3D MHD simulations of a solar active region jet, *Astron. Astrophys.*, 506, L45-L48, 2009. [46](#)
- Gosling, J., and Robson, A.E., Ion reflection, gyration, and dissipation at supercritical shocks, in *Collisionless Shocks in the Heliosphere: Reviews of Current Research*, edited by R. G. Stone, B. T. Tsurutani, Geophysical Monograph Series, AGU, 35, Washington D.C., 1985. [77](#), [79](#)
- Heber, B., Droge, W., Kunow, H., Müller-Mellin, R., Wibberenz, G., Ferrando, P., Raviart, A., and Paizis, C., Spatial variation of >106 MeV proton fluxes observed during the Ulysses rapid latitude scan: Ulysses COSPIN/KET results, *Geophys. Res. Lett.*, 23, 15131–1516, doi:10.1029/96GL01042, 1996. [52](#), [62](#), [93](#)
- Heber, B., W. Droge, P. Ferrando, L. J. Haasbroek, H. Kunow, R. Müller-Mellin, C. Paizis, M. S. Potgieter, A. Raviart, and G. Wibberenz, Spatial variation of  $\geq 40$  MeV/n nuclei fluxes observed during the Ulysses rapid latitude scan, *Astron. Astrophys.*, 316, 538–546, 1996. [52](#), [62](#), [93](#)
- Hoekesema, J. T., The large-scale structure of the heliospheric current sheet during the Ulysses epoch, *Space Sci. Rev.*, 72, 137–149, 1995. [52](#), [62](#), [93](#)
- Howard, R. A., Moses, J. D., Vourlidas, A., Newmark, J. S., Socker, D. G., Plunkett, S. P., Korendyke, C. M., Cook, J. W., Hurley, A., Davila, J. M., and 36 coauthors, Sun Earth Connection Coronal and Heliospheric Investigation (SECCHI), *Space Sci. Rev.*, 136, 1–4, 67–115, 2008. [6](#)
- Howard, T.A., Tappin, S.J., Three-Dimensional Reconstruction of Two Solar Coronal Mass Ejections Using the STEREO Spacecraft, *Solar Phys.*, 252, 373–383, 2008. [65](#)
- Hughes, J. V., The magnetopause, magnetotail, and magnetic reconnection, in *Introduction to Space Physics*, edited by M. G. Kivelson and C. T. Russell, Cambridge Univ. Press, Cambridge, UK, 1995. [90](#)

- Kaiser, M. L., Kucera, T. A., Davila, J. M., Cyr, St. O. C., Guhathakurta, M., Christian, E., The STEREO mission: an Introduction, *Space Sci. Rev.*, 136, 5–16, 2008. [6](#), [8](#), [29](#)
- Kamio, S., Hara, H., Watanabe, T., Matsuzaki, K., Shibata, K., Culhane, L., Warren, H.P., Velocity Structure of Jets in a Coronal Hole, *Pub. Astron. Soc. Japan*, 59, S757-S762, 2007 [14](#)
- Kivelson M. G., Russell C. T., Introduction to Space Physics, *Cambridge University Press*, 1995. [54](#)
- Kohl, J. L., Noci, G., Antonucci, E., Tondello, G., Huber, M. C. E., Gardner, L. D., Nicolosi, P., Strachan, L., Fineschi, S., Raymond, J. C., Romoli, M., Spadaro, D., Panasyuk, A., Siegmund, O. H. W., Benna, C., Ciaravella, A., Cranmer, S. R., Giordano, S., Karovska, M., Martin, R., Michels, J., Modigliani, A., Naletto, G., Pernechele, C., Poletto, G., Smith, P. L., First results from the soho ultraviolet coronagraph spectrometer, *Solar Phys.*, 175, 613–644, 1997. [11](#)
- Lang, K. R., The Sun from Space, *Astronomy & Astrophysics Library*, Springer, 2006. [6](#)
- Lee, L. C., Wu, B. H., Heating and Acceleration of Protons and Minor Ions by Fast Shocks in the Solar Corona, *Astrophys. J.*, 535, 1014–1026, 2000. [77](#)
- Lembége, B., Savoini, P., Nonstationarity of a two-dimensional quasiperpendicular supercritical collisionless shock by self-reformation, *Phys. Fluids B*, 4, 3533–3548, 1992. [78](#)
- Leroy, M. M., D. Winske, C. C. Goodrich, C. S. Wu, and K. Papadopoulos, The structure of perpendicular bow shocks, *J. Geophys. Res.*, 87, 5081–5094, 1982. [77](#), [78](#), [79](#), [86](#)
- Lobzin, V. V., Krasnoselskikh, V. V., Bosqued, J. M., Pincon, J. -L., Schwartz, S. J., Dunlop, M., Nonstationarity and reformation of high-Mach-number quasiperpendicular shocks: Cluster observations, *Geophys. Res. Lett.*, 34, L05107, doi:10.1029/2006GL029095, 2007. [78](#)
- Madjarska, M. S., Dynamics and plasma properties of an X-ray jet from SUMER, EIS, XRT, and EUVI A & B simultaneous observations, *Astron. Astrophys.*, 526, id. A19, 2011. [38](#)
- Mancuso, S., Raymond, J. C., Kohl, J., Ko, Y.-K., Uzzo, M., Wu, R. UVCS/SOHO observations of a CME-driven shock: Consequences on ion heating mechanisms behind a coronal shock, *Astrophys. J.*, 383, 267–274, 2002. [9](#), [76](#)

## BIBLIOGRAPHY

---

- Mazzotta, P., Mazzitelli, G., Colafrancesco, S., Vittorio, N., Ionization balance for optically thin plasmas: Rate coefficients for all atoms and ions of the elements H to NI, *Astron. Astrophys. Suppl.*, 133, 403–409, 1998. [35](#), [41](#)
- Moore, R. L., Cirtain, J. W., Sterling, A. C., Falconer, D. A., Dichotomy of solar coronal jets: standard jets and blowout jets, *Astrophys. J.*, 720, 757–770, 2010. [14](#), [18](#)
- Moreno-Insertis, F., Galsgaard, K. and Ugarte-Urra, I.: Jets in coronal hole: HINODE Observations and three-dimensional computer modeling, *Astrophys. J.*, 673, L211–L214, 2008. [14](#), [16](#), [38](#), [45](#), [46](#), [93](#)
- Mursula K., Hiltula T., Systematically asymmetric heliospheric magnetic field: evidence for a quadrupole mode and non-axisymmetry with polar flip-flops, *Solar Phys.*, 224, 133–143, 2005 [53](#), [62](#), [93](#), [94](#)
- Nisticò, G., Bothmer, V., Patsourakos, S., Zimbardo, G., Characteristics of EUV coronal jets observed with STEREO/SECCHI, *Solar Phys.*, 259, 87–108, 2009. [10](#), [27](#), [39](#), [51](#), [76](#)
- Nisticò, G., Bothmer, V., Patsourakos, S., Zimbardo, G., Observational features of equatorial coronal hole jets, *Annales Geophysicae*, 28, 687–696, 2010. [10](#), [76](#)
- Nisticò, G., Patsourakos, S., Bothmer, V., Zimbardo, G., Determination of temperature maps of EUV coronal hole jets, *Adv. Space Res.*, 48, 1490–1498, 2011. [10](#)
- Nisticò, G., Zimbardo, G., Heating heavy ions in the polar corona by collisionless shocks: a one-dimensional simulation, *Adv. Space Res.*, doi:10.1016/j.asr.2011.09.029, 2011. [11](#)
- Phillips, P.E., and Robson, A.E., Influence of reflected ions on the magnetic structure of a collisionless shock front, *Phys. Rev. Lett.*, 29, 154–157, 1972. [77](#), [78](#)
- Paraschiv, A. R., Lacatus, D. A., Badescu, T., Lupu, M. G., Simon, S., Sandu, S. G., Mierla, M., Rusu, M. V., Study of Coronal Jets During the Solar Minimum Based On STEREO/SECCHI Observations, *Solar Phys.*, 264, 365–375, 2010 [14](#)
- Pariat, E., Antiochios, S. K., DeVore, C. R., A model for solar polar jets, *Astrophys. J.*, 691, 61–74, 2009. [14](#), [18](#), [21](#), [31](#), [38](#)
- Pasachoff, J. M., Rusin, V., Druckmüller, M., Aniol, P., Saniga, M., Minarovjech, M., The 2008 August 1 eclipse solar-minimum corona unraveled, *Astrophys. J.*, 702, 1297–1308, 2009. [4](#)

- Patsourakos, S., & Klimchuk, J., The cross-field thermal structure of coronal loops from triple-filter TRACE observations, *Astrophys. J.*, 667, 591–601, 2007. [36](#)
- Patsourakos, S., Pariat, E., Vourlidas, A., Antiochios, S. K. and Wuelser, J. P., STEREO SECCHI stereoscopic observations constraining the initiation of polar coronal jets, *Astrophys. J.*, 680: L73-L76, 2008. [14](#), [18](#), [21](#), [27](#), [31](#), [76](#)
- Patsourakos, S., Vourlidas, A. & Kliem, B., Toward understanding the early stages of an impulsively accelerated coronal mass ejection, *Astron. Astrophys.*, 522, id. A100, 2010. [51](#)
- Paul, J. W. M., Holmes, L. S., Parkinson, M. J., and Sheffield, J., Experimental observations on the structure of collisionless shock waves in a magnetized plasma, *Nature*, 208, 133–135, 1965. [77](#)
- Perri, S., Greco A., Zimbardo, G. Stochastic and direct acceleration mechanisms in the Earth’s magnetotail, *Geophys. Res. Lett.*, 36, L04103, doi:10.1029/2008GL036619, 2009. [76](#)
- Petrosian, V., Liu, S. Stochastic Acceleration of Electrons and Protons. I. Acceleration by Parallel-Propagating Waves, *Astrophys. J.*, 610, 550–571, 2004. [76](#)
- Quest, K.B. Simulations of high Mach number perpendicular shocks with resistive electrons, *J. Geophys. Res.*, 91, 8805–8815, 1986. [78](#)
- Raouafi, N.-E., Petrie, G. J. D., Norton, A. A., Henney, C. J., Solanki, S. K., Evidence for polar jets as precursors of polar plume formation, *Astrophys. J.*, 682, L137-L140, 2008 [32](#)
- Ryutova, M., Habbal, S., Woo, R., Tarbell, T., Photospheric network as the energy source for the quiet-sun corona, *Solar Phys.*, 200, 213–234, 2001 [38](#)
- Ryutova, M., Berger, T., Frank, Z., Title, A., On the penumbral jetlike features and chromospheric bow shocks, *Astrophys. J.*, 686, 1404–1419, 2008 [76](#)
- Savcheva, A., Cirtain, J., DeLuca, E. E., Lundquist, L. L., Golub, L., Weber, M., A study of Polar Jet Parameter Based on Hinode XRT Observations, *Pub. Astron. Soc. Japan*, 59, S771-S778. 2007. [14](#), [27](#)
- Schmelz, J.T., Beene, J. E., Nasraoui, K., Blevins, H. T., Martens P. C. H., Cirtain, J. W., The effect of background subtraction in the temperature of EIT coronal loops, *Astrophys. J.*, 599, 604–614, 2003. [39](#), [41](#), [92](#)

## BIBLIOGRAPHY

---

- Sckopke, N., Paschmann, G., Bame, S. J., Gosling, J. T., Russell, C. T. Evolution of ion distributions across the nearly perpendicular bow shock - Specularly and non-specularly reflected-gyrating ions, *J. Geophys. Res.*, 88, 6121–6136, 1983. [77](#)
- Scudder, J. D., Mangeney, A., Lacombe, C., Harvey, C. C., Wu, C. S., The resolved layer of a collisionless, high beta, supercritical, quasi-perpendicular shock wave. III - Vlasov electrodynamics, *J. Geophys. Res.*, 91, 11075–11097, 1986. [77](#)
- Simpson, J.A., Zhang, M., and Bame, S., A solar polar north-south asymmetry for cosmic ray propagation in the heliosphere: The Ulysses pole-to-pole rapid transit, *Astrophys. J.*, 465, L69-L72, 1996. [52](#), [62](#), [93](#)
- Shibata, K., Ishido, Y., Acton, L. W., Strong, K. T., Hirayama, T., Uchida, Y., McAllister, A. H., Matsumoto, R., Tsuneta, S., Shimizu, T., Hara, H., Sakurai, T., Ichimoto, K., Nishino, Y., Ogawara, Y., Observations of X-ray jets with the YOHKOH Soft X-ray Telescope, *Pub. Astron. Soc. Japan*, 44, L173-L179, 1992. [14](#), [18](#)
- Shimojo, M., Hashimoto, S., Shibata, K., Hirayama, T., Hudson, H. S., Acton, L. W., Statistical study of solar X-Ray jets observed with the Yohkoh Soft X-Ray Telescope, *Pub. Astron. Soc. Japan*, 48, 123–126 and Plate 1-4, 1996. [14](#), [18](#), [24](#)
- Shimojo, M., S., Shibata, K., Physical Parameters of Solar X-Ray Jets, *Astrophys. J.*, 542, 1100–1108, 2000. [14](#), [46](#), [93](#)
- Thernisien, A., Howard, R.A., Vourlidas, A., Modeling of flux rope Coronal Mass Ejections *Astrophys. J.*, 652, 763–773, 2006. [10](#), [66](#), [73](#), [94](#)
- Thernisien, A., Vourlidas A., Howard, R.A., Forward modeling of Coronal Mass Ejections using STEREO/SECCHI data, *Solar Phys.*, 256, 111–130, 2009. [63](#), [65](#), [66](#), [67](#)
- Terzo, S., Reale, F., On the importance of background subtraction in the analysis of coronal loops observed with TRACE, *Astron. Astrophys.*, 515, id.A7, 2010. [41](#)
- Tsuneta, S., and Naito T., Fermi acceleration at the fast shock in a solar flare and the impulsive loop-top hard x-ray source, *Astrophys. J.*, 495: L67, 1998. [76](#), [90](#)
- Trotter, G, MacQueen, R. M., The orientation of pre-transient coronal magnetic fields, *Solar Phys.*, 68, 177–186, 1980. [65](#)
- Veltri, P., Zimbardo, G., Electron-whistler interaction at the Earth's bow shock: 1. Whistler instability, *J. Geophys. Res.*, 98, 13325–13333, 1993. [77](#)



- Veltri, P., Zimbardo, G., Electron-whistler interaction at the Earth's bow shock: 2. Electron pitch angle diffusion, *J. Geophys. Res.*, 98, 13335–13346, 1993. [77](#)
- Virtanen, I. I., and Mursula, K.. Asymmetry of solar polar fields and the southward shift of HCS observed by Ulysses, *J. Geophys. Res.*, 115, A09110, doi: 10.1029/2010JA015275, 2010. [52](#)
- Wang Y.-M., and Shelley, Jr. N. R., On potential field model of the solar corona, *Astrophys. J.*, 392, 310–319, 1992 [58](#)
- Wang Y.-M., Non radial coronal streamer, *Astrophys. J.*, 456, L119-L121, 1996. [51](#)
- Wang, Y.-M., Shelley, N. R., Socker, Jr., D. G., Howard, R. A., Brueckner, G. E., Michels, D. J., Moses, D., & St. Cyr, O. C., Llebaria, A., & Delaboudinière, J.-P., Observations of correlated white-light and Extreme-Ultraviolet Jets from polar coronal holes, *Astrophys. J.*, 508, 899–907, 1998. [14](#), [16](#)
- Yamauchi, Y., Moore, R. L., Suess, S. T., Wang, H., Sakurai, T., The magnetic structure of H $\alpha$  macrospicules in solar coronal holes, *Astrophys. J.*, 605, 511–520, 2004. [16](#), [18](#)
- Yang, Z. W., Lu, Q. M., Lembége, B., Wang, S. Shock front nonstationarity and ion acceleration in supercritical perpendicular shocks, *J. Geophys. Res.*, 114, A03111, 2009. [78](#)
- Yokoyama, T., and Shibata, K., Magnetic reconnection as the origin of X-ray jets and H $\alpha$  surges on the Sun, *Nature*, 375, 42–44, 1995. [14](#), [76](#)
- Yokoyama, T., and Shibata, K., Numerical Simulation of Solar Coronal X-Ray Jets Based on the Magnetic Reconnection Model, *Publ. Astron. Soc. Japan*, 48, 353-376, 1996. [9](#), [14](#), [18](#), [38](#), [76](#), [90](#)
- Zelenyi, L. M., Dolgonosov, M. S., Grigorenko, E. E., Sauvaud, J.-A., Universal properties of the nonadiabatic acceleration of ions in current sheets, *JETP Letters*, 85, 187–193, 2007. [89](#)
- Zimbardo G., More than mass proportional heating of heavy ions by supercritical collisionless shocks in the solar corona, ArXiv: 0906.324V1[astro-ph.SR], 2009. [11](#), [76](#), [77](#), [86](#), [89](#), [94](#)
- Zimbardo G., More than mass proportional heating of heavy ions by collisionless quasi-perpendicular shocks in the solar corona, Twelfth International Solar Wind Conference. AIP Conference Proceedings, 1216, 52–55, 2010. [75](#), [76](#), [77](#), [89](#)

## BIBLIOGRAPHY

---

Zimbardo G., Heavy ion reflection and heating by collisionless shocks in polar solar corona, *Planet. Space. Sci.*, 59, 468–474, 2011. [11](#), [75](#), [77](#), [79](#), [86](#), [89](#)



# Acknowledgements

The work presented in this thesis has been possible thanks the support of people who helped me during my studies and these three years of Ph.D. at the Department of Physics of the University of Calabria.

I would like to thank prof. Gaetano Zimbardo for his constant support, for having introduced me in the world of research, taught to make science, and for unforgettable experiences during the Ph.D. (included a trip by train from Germany to Calabria).

I especially thank dr. Volker Bothmer: I knew him during my Erasmus at the University of Göttingen, and I had the second chance to work with him for six months, during the last year of my Ph.D. Thanks to him for having given me the possibility to make research in solar physics and also for establishing contacts into the scientific community.

Many thanks to Eckhard Bosman, with whom I had a nice collaboration activity in Göttingen, and for his assistance during my stay in Germany. Best wishes for your Ph.D., Eckhard!

I acknowledge dr. Spiros Patsourakos for his kind support in working and analysing solar data, and for useful discussions made by e-mail or during conferences too.

I generally thank the group of Astrophysics and Plasma Physics, at the University of Calabria, for the nice family atmosphere in which I worked. Thanks to Sergio, and the rest of the company for joking me, even if he stopped during the last year. Very strange!

General thanks go to my friends: it is really impossible to remember everyone, a lot of friends, and this is the most wonderful thing that I met during these years at the University. Thanks to Vincenzo, Denise, Loris, Serena and Sandro for sharing the office, trips (by disreputable planes), school or conference meetings (and for the famous song "*Bohemian Nisticò*"). Many thanks to everybody with whom I shared nice moments, inside and outside the University, above all during these last months.

Final thanks to my family, in particular to my parents and my sister, who have seen me to travel a lot, always out, and only few moments at home. In their eyes I have become an important person, but this is not true!

And we are at the end: these years were nice but with many difficulties, too. I had the defect to finish my work always at the last minute, including

12/10/2011

...in ufficio!



the writing of this thesis, too. The picture in this last page gives a sketch a of my hurried activity at last minute: thanks Manuela for having drawn it!